Ab initio Prediction of Thermodynamics in Alkali Metal-Air Batteries

by

ShinYoung Kang

B.S. Materials Science and Engineering, Seoul National University, Korea, 2007

SUBMITTED TO THE DEPARTMENT OF
MATERIALS SCIENCE AND ENGINEERING
IN PARTIAL FULFILLMENT OF THE REQUIREMENTS FOR THE DEGREE OF

DOCTOR OF PHILOSOPHY
AT THE
MASSACHUSETTS INSTITUTE OF TECHNOLOGY

JUNE 2014

Signature redacted
Signature of Author ....
Department of Materials Science and Engineering
May 19th, 2014

Signature redacted
Certified by ....
Gerbrand Ceder
R.P. Simmons Professor of Materials Science and Engineering
Thesis Supervisor

Signature redacted
Accepted by ....
Gerbrand Ceder
Chair, Department Committee on Graduate Students

(This page is intentionally left blank)

Ab initio Prediction of Thermodynamics in Alkali Metal-Air Batteries

by

ShinYoung Kang

Submitted to the Department of Materials Science and Engineering on May 19th, 2014 in
Partial Fulfillment of the Requirements for the Degree of Doctor of Philosophy
at the Massachusetts Institute of Technology

Abstract

Electric vehicles ("EVs") require high-energy-density batteries with reliable cyclability and rate capability. However, the current state-of-the-art Li-ion batteries only exhibit energy densities near ~150 Wh/kg, limiting the long-range driving of EVs with one charge and hindering their wide-scale commercial adoption.[1-3] Recently, non-aqueous metal–O_2 batteries have drawn attention due to their high theoretical specific energy.[2, 4-6] Specifically, the issues surrounding battery studies involve Li–O_2 and Na–O_2 batteries due to their high theoretical specific energies of 3.5 kWh/kg (assuming Li_2O_2 as a discharge product in Li–O_2 batteries) and 1.6 and 1.1 kWh/kg (assuming Na_2O_2 and NaO_2 as discharge products, respectively, in Na–O_2 batteries).

Since the potential of Li–O_2 batteries as an energy storage system was first proposed in 1996,[1] various studies have criticized and verified their shortcomings, such as their low power density, poor cyclability, and poor rate capability.[7, 8] Substantial research attempts have been made to identify the cause of the high overpotentials and electrolyte decomposition and to search for better cathode/electrolyte/anode and/or catalyst material combinations. However, Li–O_2 battery technology remains in its infancy primarily due to the lack of understanding of the underlying mechanisms. Therefore, we investigate the charging mechanism, which contributes to the considerable energy loss using first-principles calculations and propose a new charging mechanism based on experimental observations and knowledge concerning Li-ion and Na-ion batteries.

Most studies on metal–O_2 batteries have mainly focused on Li–O_2 batteries. However, recently, the promising performance of Na–O_2 systems has been reported.[9, 10] Although Na–O_2 batteries exhibit slightly lower theoretical specific energies than those of the Li–O_2 batteries as specified above, the chemical difference between the two alkali metals substantially distinguishes the electrochemistry properties of Na–O_2 and Li–O_2. In the Na–O system, both NaO_2 and Na_2O_2 are stable compounds, while in the Li–O system, LiO_2 is not a stable compound under standard state conditions (300 K and 1 atm).[11, 12] Presumably, due to this chemical difference, the Na–O_2 system has exhibited a much smaller charging overpotential, as low as 0.2 V, when NaO_2 is formed as a discharge product, compared with that in Li–O_2 system, >1 V. Such a low charging overpotential in Na–O_2 batteries demonstrates their potential as a next generation electrochemical system for commercially viable EVs .[9, 10] In this thesis, we study the thermodynamic stability of Na–O compounds to identify the phase selection conditions that affect the performance of Na–O_2 batteries.

Thesis Supervisor: Gerbrand Ceder
Title: R.P. Simons Professor of Materials Science and Engineering

(This page is intentionally left blank)

Acknowledgments

My professors, family, and friends enabled me to survive my graduate life at MIT with their warm encouragement, prayers, and support. I cannot imagine my life and career apart from them, and here, I would like to express many thanks.

First of all, I would like to express my appreciation to my thesis advisor, Professor Gerbrand Ceder, for his insight, patience, and research guidance. Without his enthusiasm and advice over the past academic years, I could not have completed this thesis. I am also grateful to my thesis committee members, Professors Yang Shao-Horn and Jeffrey C. Grossman, for sharing their knowledge and wisdom.

My grateful thoughts are extended to my coworkers, officemates, and research group, with whom I have shared inspiring and helpful discussions. Maria K. Y. Chan, Yifei Mo, and Shyue Ping Ong have offered great scientific contributions and support as my mentors. I cannot emphasize enough how my 13-5025 officemates have helped me build a new life in academia and how much I have enjoyed our conversations, discussions, and internal jokes. In addition, I have been so lucky to benefit from the endless passion, great cooperation, and invaluable collegial minds of the Ceder group members Byoungwoo Kang, Jae Chul Kim, Dong-Hwa Seo, Kathryn Simons, and many others.

Next, I would like to thank all the members in KGMSE and KGSA at MIT; my vivacious suitemate, Yuhan Chen; a generous lawyer, MyungJin Lee; and friends from Harvard. I truly appreciate their warm hearts and support, similar to those of my family back home, a thousand miles away. I have loved celebrating our highs and getting through our lows together. I send my special thanks to my church members from DongKwang Church back in Korea, the Korean Church of the Shepherd in Boston, and Cambridgeport Baptist Church. The members of these churches have spiritually encouraged my studying and living in the U.S. I am grateful to the members of the churches including but not limited to Reverend YongHwal Cho and Pastor Dae-Sung Choi for their support through prayer.

My family members back in Korea have always been my biggest cheerleaders. I deeply appreciate my incredible grandparents, parents, brother, sister-in-law, and my little nephews. Their unwavering love and support sustained me to pursue an academic path and a new life. I would like to give thanks to God for giving me the most amazing family one could ask for.

Last but not least, praise God!

Table of Contents

List of Figures

Figure 1. The theoretical and practical gravimetric energy densities of Li-ion and metal-air batteries. The practical energy densities of metal-air batteries are estimated by applying a reduction factor of 4–7 to the theoretical ones, and the error bars denote the range of the applied reduction factor.

Figure 2. The formation energies calculated in (a) GGA and (b) HSE plotted versus the experimental formation enthalpies at the standard state (300 K and 1 atm)[56] in eV/O_2 for oxides (blue triangles), peroxides (red squares), and superoxides (green circles). The data points corresponding to Li_2O_2 and SrO_2 overlap on this scale. The insets show zoomed-in formation energies for superoxides. The trend lines with slope = 1 are plotted for each group, and the oxidation energy correction is the y-intercept of each line. Reprinted with permission from Kang, S.; Mo, Y.; Ong, S. P.; Ceder, G. *Chemistry of Materials* **2013,** 25 (16), 3328-3336 and Kang, S.; Mo, Y.; Ong, S. P.; Ceder, G. *Nano Letters* **2014,** 14 (2), 1016-1020. Copyright 2014 American Chemical Society.

Figure 3. The structure for Li_2O_2 (a) and candidate structures for LiO_2 (b-h). The green spheres represent Li ions, and the red spheres represent O ions. The oxygen bonds are marked as red bars. (a) Two distinct Li sites exist in the Li_2O_2 structure with the $P6_3$/mmc space group: a site that forms a Li-only layer (henceforth known as the "L" site) and a site in the plane that contains the O_2^{2-} bond centers (henceforth labeled as the "P" site). From (b) to (h), nine candidate LiO_2 structures are displayed accordingly. (b) The structures derived from Li_2O_2 by extracting two Li ions from a Li_2O_2 unit cell, which are labeled by their symmetry; (c) layered P3 structure by removing Na and replacing Co with Li from P3 $NaCoO_2$; (d) marcasite structure; (e) C2/m structure, where Li and O_2^- layers are alternately stacked; (f) I4/mmm structure, where LiO_2 dimers are arranged in a bipyramid structure; (g) pyrite structure; and (h) a structure in the Pbca space group, which has a similar arrangement of atoms as in the pyrite structure but in an orthorhombic lattice. Reprinted with permission from Kang, S.; Mo, Y.; Ong, S. P.; Ceder, G. *Chemistry of Materials* **2013,** 25 (16), 3328-3336. Copyright 2014 American Chemical Society.

Figure 4. The calculated formation free energy (in eV/O_2) of the different structures considered for LiO_2. Multiple data-points indicate the energies computed from different initial structures, such as NaO_2, CsO_2, and MgO_2, or from different magnetic states. The lowest energy structure is Pnnm (−2.68 eV/O_2). Reprinted with permission from Kang, S.; Mo, Y.; Ong, S. P.; Ceder, G. *Chemistry of Materials* **2013,** 25 (16), 3328-3336. Copyright 2014 American Chemical Society.

Figure 5. Phonon dispersion and density of states for LiO_2 in the (a) Pnnm and (b) *$P6_3$/mmc-layered* structures. The partial phonon density of states contributed from Li and O are represnted in red and blue, respectively. Reprinted with permission from Kang, S.; Mo, Y.; Ong, S. P.; Ceder, G. *Chemistry of Materials* **2013,** 25 (16), 3328-3336. Copyright 2014 American Chemical Society.

Figure 6. (a) A *layered* structure of $Li_{2-x}O_2$ ($0 < x < 1$), where the Li_2O_2 and LiO_2 phases are separated by the *a-b* plane, and (b) a *channel* structure of $Li_{2-x}O_2$ ($0 < x < 1$), where the Li_2O_2 and LiO_2 phases are separated by the *a-c* or *b-c* planes. Yellow shading is used to highlight LiO_2 regions distinguished from Li_2O_2. Reprinted with permission from Kang, S.; Mo, Y.; Ong, S. P.; Ceder, G. *Chemistry of Materials* **2013,** 25 (16), 3328-3336. Copyright 2014 American Chemical Society.

Figure 7. The formation free energy (eV/O_2) of the off-stoichiometry $Li_{2-x}O_2$ structures referenced to the equilibrium in Eq. (3-1). The red solid line connects the lowest energy off-stoichiometry $Li_{2-x}O_2$ structures starting from Li_2O_2 with the ground state structure of LiO_2 (Pnnm), whereas the red dashed line ends with the topotactically delithiated *$P6_3$/mmc-layered* LiO_2 structure. Reprinted with permission from Kang, S.; Mo, Y.; Ong, S. P.; Ceder, G. *Chemistry of Materials* **2013,** 25 (16), 3328-3336. Copyright 2014 American Chemical Society.

Figure 8. The non-equilibrium voltage profile from Li_2O_2 ($x = 0$) to O_2 ($x = 2$). The red solid and dotted line indicates the predicted topotactic oxidation path. The dashed blue line denotes

the direct decomposition of Li_2O_2 into 2 Li^+ + 2 e^- + O_2. The lowest energy structures are shown along the path. Reprinted with permission from Kang, S.; Mo, Y.; Ong, S. P.; Ceder, G. *Chemistry of Materials* **2013,** 25 (16), 3328-3336. Copyright 2014 American Chemical Society.

Figure 9. The formation energy (eV/O_2) of (a) $Li_{1.75}O_2$ (b) $Li_{1.50}O_2$ and (c) $Li_{1.25}O_2$ referenced to the equilibrium phases in Eq. (3-1). The "layered" structures have the lowest energy, followed by the "channel" and other "phase-separated" structures. The "solid solution" structures are highest in energy. Representative structures for each group are inserted with superoxide regions highlighted by yellow boxes. The lowest-energy layered structures are displayed in Fig. 8, and their energies are listed in Table 2. Reprinted with permission from Kang, S.; Mo, Y.; Ong, S. P.; Ceder, G. *Chemistry of Materials* **2013,** 25 (16), 3328-3336. Copyright 2014 American Chemical Society.

Figure 10. A facile off-stoichiometric mechanism of charging in Li-O_2 batteries. Due to the non-monotonic voltage profile upon charging (Fig. 8), only a few Li_2O_2 particles are involved in the topotactic delithiation at any given time. Reprinted with permission from Kang, S.; Mo, Y.; Ong, S. P.; Ceder, G. *Chemistry of Materials* **2013,** 25 (16), 3328-3336. Copyright 2014 American Chemical Society.

Figure 11. The structures of (a) $Im\bar{3}m$ Na metal; (b) $Fm\bar{3}m$ Na_2O; (c) $P\bar{6}2m$ Na_2O_2; NaO_2 polymorphs, (d) Pnnm, (e) $Pa\bar{3}$ (ordered form of $Fm\bar{3}m$), and (f) $Rm\bar{3}$; and (g) Imm2 NaO_3. The yellow spheres represent Na ions, and the red spheres represent O ions with their bonds marked as red bars. Reprinted with permission from Kang, S.; Mo, Y.; Ong, S. P.; Ceder, G. *Nano Letters* **2014,** 14 (2), 1016-1020. Copyright 2014 American Chemical Society.

Figure 12. Phonon dispersion and density of states for (a) $Im\bar{3}m$ Na metal, (b) $Fm\bar{3}m$ Na_2O, (c) $P\bar{6}2$ Na_2O_2, (d) Pnnm NaO_2, (e) $R\bar{3}m$ NaO_2, and (f) Imm2 NaO_3. The partial phonon density of states contributed from Na and O are shown in blue and red, respectively. The phonon dispersion of $Pa\bar{3}$ NaO_2 calculated using the small displacement method (SDM) with the energy cutoff set to 700 eV and the density functional perturbation theory (DFPT) is

displayed in (g) and (h), respectively. Reprinted with permission from Kang, S.; Mo, Y.; Ong, S. P.; Ceder, G. *Nano Letters* **2014,** 14 (2), 1016-1020. Copyright 2014 American Chemical Society.

Figure 13. The formation free energies of $Fm\bar{3}m$ Na_2O (blue), $P\bar{6}2m$ Na_2O_2 (red), Pnnm NaO_2 (dashed gray line), $Fm\bar{3}m$ NaO_2 (dash-dot gray line), and the lowest energy envelope for NaO_2 (green) as a function of temperature. The calculated data are plotted in lines, and the experimental data are marked as circles. Reprinted with permission from Kang, S.; Mo, Y.; Ong, S. P.; Ceder, G. *Nano Letters* **2014,** 14 (2), 1016-1020. Copyright 2014 American Chemical Society.

Figure 14. The phase diagram of bulk Na–O compounds as a function of temperature and O_2 partial pressure. The red, yellow, and green domains represent the regions where Na_2O_2, Pnnm NaO_2, and $Fm\bar{3}m$ NaO_2 are stable, respectively. The Pnnm NaO_2 structure transforms to $Fm\bar{3}m$ NaO_2 at 230–240 K when $P_{O_2} = 1$ atm, and Na_2O_2 is in equilibrium with $Fm\bar{3}m$ NaO_2 at 8.5 atm when $T = 300$ K. The horizontal dashed line denotes $P_{O_2} = 1$ atm, and the vertical dashed line denotes $T = 300$ K. Reprinted with permission from Kang, S.; Mo, Y.; Ong, S. P.; Ceder, G. *Nano Letters* **2014,** 14 (2), 1016-1020. Copyright 2014 American Chemical Society.

Figure 15. The stability map of Na–O compounds and their chemical potential boundaries at (a) 0 K and (b) 300 K. (a-1) and (b-1) are before applying the E_{oxd}; (a-2) and (b-2) are after applying the E_{oxd}; and (a-3) and (b-3) are based on experimental formation enthalpies.[58] The stability of compounds is mapped on a linear μ_{o} scale, and the corresponding μ_{Na} values at the phase boundaries are labeled above the top axes. Note that the μ_{Na} scale is not linear according to the stoichiometry of the mapped compounds.

Figure 16. The surface unit cell of a Na_2O_2 {0001} facet terminated at the (a) A layer and (b) B layer. The yellow spheres represent Na ions, and the red spheres represent O ions. The surface ions that are used to define the surface terminations are labeled in the figure.

Figure 17. The surface unit cell of Na_2O_2 $\{1\bar{1}00\}$ terminated at the (a) A layer, (b) B layer, and (c) B′ layer. The yellow spheres represent Na ions, and the red spheres represent O ions. The surface ions that are used to define the surface terminations are labeled in the figure.

Figure 18. The surface unit cell of Na_2O_2 $\{11\bar{2}0\}$ terminated at the (a) A layer, (b) B layer, and (c) C layer. The yellow spheres represent Na ions, and the red spheres represent O ions. The surface ions that are used to define the surface terminations are labeled in the figure.

Figure 19. (a) Surface energies of Na_2O_2 as a function of μ_o for the most stable terminations of $\{0001\}$, $\{1\bar{1}00\}$, and $\{11\bar{2}0\}$ facets at 300 K and 1 atm. The range of μ_o where Na_2O_2 is stable, from the O_2 gas limit to the Na_2O limit, is marked using a yellow box, and the Wulff shapes at these two limits are displayed in (b) and (c), respectively. The color scheme of surface energies used for the Wulff shapes is displayed in the scale bar in meV/Å^2.

Figure 20. The surface unit cell of $Pa\bar{3}$ NaO_2 in the (a) $\{100\}$ orientation, (b) $\{110\}$ orientation, $\{111\}$ orientation terminated at the (c-1) A layer and (c-2) B layer, and $\{211\}$ orientation terminated at the (d-1) A layer and (d-2) B layer. The yellow spheres represent Na ions, and the red spheres represent O ions, and the surface ions that are used to define the surface terminations are labeled in the figure.

Figure 21. (a) Surface energies of $Pa\bar{3}$ NaO_2 as a function of μ_o for the most stable terminations of the $\{100\}$, $\{110\}$, $\{111\}$, and $\{211\}$ facets at 300 K and 1 atm. NaO_2 exists as metastable at the standard state; therefore, its equilibrium boundary with Na_2O_2 and O_2 gas, the most oxidizing and reducing conditions, respectively, is considered and marked using a yellow box. The Wulff shapes at these two limits are identical and are represented by the cube displayed in (b). The color scheme of the surface energies used for the Wulff shape is displayed in the scale bar in meV/Å^2.

Figure 22. The correction energy applied to the surface energies by Eq. (8-11) as a function of the surface O–O bond lengths of all the surface terminations we considered for Na_2O_2 (blue circles) and NaO_2 (red triangles). The dashed vertical lines indicate the O_2 bond lengths in O_2 gas (1.23 Å), bulk $Pa\bar{3}$ NaO_2 (1.35 Å), and bulk Na_2O_2 (1.55 Å averaged over three O_2 bonds) and the distance between nearest O–O ions in bulk Na_2O (3.96 Å) from left to right. The blue and red lines are obtained from the linear regression for each non-stoichiometric surface group (Na-rich or O-rich) centering on the O_2^{2-} and O_2^{-} bond lengths in their bulk states, respectively.

Figure 23. Phase diagram of Na_2O_2 (red) and NaO_2 (green) at 300 K as a function of particle size and P_{O_2} at the O_2 gas limit. The particle size is defined as $(V^0)^{1/3}$, where V^0 is the total volume of the particle. Reprinted with permission from Kang, S.; Mo, Y.; Ong, S. P.; Ceder, G. *Nano Letters* **2014,** 14 (2), 1016-1020. Copyright 2014 American Chemical Society.

Figure 24. (a, c) The critical nucleus size and (b, d) critical nucleation energy barrier of Na_2O_2 and NaO_2 particles as a function of P_{O_2} at $\phi = 2.1$ V vs. Na/Na^+ ((a) and (b)) and as a function of voltage at $P_{O_2} = 1$ atm ((c) and (d)). The applied potential 2.1 V for (a) and (b) is 0.21 and 0.18 V lower than the calculated equilibrium potentials of Na_2O_2 and NaO_2, respectively. These equilibrium potentials of Na_2O_2 and NaO_2 are marked by vertical lines in (c) and (d). Reprinted with permission from Kang, S.; Mo, Y.; Ong, S. P.; Ceder, G. *Nano Letters* **2014,** 14 (2), 1016-1020. Copyright 2014 American Chemical Society.

List of Tables

Table 1. Theoretical gravimetric and volumetric energy densities of Li-ion and metal-air batteries. The discharge products for metal-air batteries are noted in parentheses. The energy density values are calculated based on the active components only.

Table 2. The calculated formation enthalpy in eV per formula unit, experimental entropy in meV/K per formula unit, and oxidation energy correction in eV per formula unit obtained in Chapter 2.2 for Li metal, O_2 gas, and Li–O compounds. The formation enthalpies of the intermediate compounds, $Li_{1.75}O_2$, $Li_{1.50}O_2$, and $Li_{1.25}O_2$, are obtained from the lowest energy structures in Fig. 8, and their Ehentropies and oxidation energy correction are linearly interpolated from Li_2O_2 and LiO_2. Reprinted with permission from Kang, S.; Mo, Y.; Ong, S. P.; Ceder, G. *Chemistry of Materials* **2013,** 25 (16), 3328-3336. Copyright 2014 American Chemical Society.

Table 3. Structure and phase transition information about the Na and Na–O compounds considered in this study.[58] Reprinted with permission from Kang, S.; Mo, Y.; Ong, S. P.; Ceder, G. *Nano Letters* **2014,** 14 (2), 1016-1020. Copyright 2014 American Chemical Society.

Table 4. The calculated formation free energies of Na–O compounds (experimental values[58] in parentheses) at 0 K and 300 K at 1 atm. The stable phases at each temperature are marked in bold. Reprinted with permission from Kang, S.; Mo, Y.; Ong, S. P.; Ceder, G. *Nano Letters* **2014,** 14 (2), 1016-1020. Copyright 2014 American Chemical Society.

Table 5. The average surface energy changes ($\langle \Delta\gamma \rangle$ in meV/Å^2) between {0 K, without E_{oxd}} and {300 K, with E_{oxd}} for Na-rich or O-rich surface slabs of Na_2O_2. The contribution to the $\Delta\gamma$ is divided into three terms: i) $\Delta\mu_{\mathrm{Na}}$ due to ΔT from 0 K to 300 K, ii) $\Delta\mu_{\mathrm{Na}}$ due to the energy correction applied to bulk phases $E_{\mathrm{oxd,\,bulk}}$, and iii) the oxidation correction energy difference between the surface slab and the bulk, ΔE_{oxd}.

Table 6. The average surface energy changes ($\langle\Delta\gamma\rangle$ in meV/Å^2) between {0 K, without E_{oxd}} and {300 K, with E_{oxd}} for Na-rich or O-rich surface slabs of NaO_2. The contribution to the Δγ is divided into three terms, i) $\Delta\mu_{\text{Na}}(\Delta T)$, ii) $\Delta\mu_{\text{Na}}(E_{\text{oxd, bulk}})$, and iii) ΔE_{oxd}.

Table A 1. Surface energies (in meV/Å^2) of different orientations and terminations of Na_2O_2 at 0 K without E_{oxd}, the correction energy difference between the surface slab and bulk Na_2O_2 (ΔE_{oxd}), which is the net correction energy applied to the surface energies, and the corrected surface energies at 300 K. The NaO_2 limit (O_2 gas limit) represents the most oxidizing condition, and the Na_2O limit (Na_2O limit) represents the most reducing condition for Na_2O_2 at 0 K (300 K). The lowest energy terminations are marked in bold for each condition.

Table A 2. Surface energies (in meV/Å^2) of different orientations and terminations of $Pa\bar{3}$ NaO_2 at 0 K without E_{oxd}, the correction energy difference between the surface slab and bulk NaO_2 (ΔE_{oxd}), which is the net correction energy applied to the surface energies, and the corrected surface energies at 300 K. The O_2 gas limit (Na_2O_2 limit) represents the most oxidizing condition, and the Na_2O_2 limit (O_2 gas limit) represents the most reducing condition for Na_2O_2 at 0 K (300 K). The lowest energy terminations are marked in bold for each condition.

PART ONE

Chapter 1. Non-Aqueous Metal-Air Batteries as an Energy Storage System for Vehicles

Li-ion batteries are widely used in applications including small and portable electronics such as cellphones and laptop computers and even for bigger systems such as electric vehicles ("EVs"). In Li-ion batteries, Li^+ ions navigate from an anode to a cathode through an electrolyte and intercalate during discharging, and the vice-versa reaction occurs during charging. The most common Li intercalation cathodes for Li-ion batteries are based on oxides such as layered $LiCoO_2$ (in the $R\bar{3}m$ space group) and spinel $LiMn_2O_4$ (in the $Fd\bar{3}m$ space group) and phosphates such as $LiFePO_4$ (in the Pnma space group) due to their useful features in terms of affordable energy density, safety, and longer cyclability. Their theoretical specific energy (in kWh/kg) and volumetric energy density (in kWh/L) are listed in Table 1. In addition, the practical specific energies are substantially lower than the theoretical ones by including but not being limited to the use of binders and electrolytes, packaging, and wiring harnesses. The practical specific energy of these Li-ion batteries is presented in Fig. 1. The current state-of-the-art Li-ion batteries are only able to provide less than 200 km of driving range between charging, which is significantly far behind the needs of 500 km for full EVs.[13] Therefore, to develop commercially feasible EVs, an electrochemical energy storage system with a higher energy density than Li-ion batteries is needed.

A significant amount of research has been focused on studying metal-air batteries as a replacement for Li-ion batteries because metal-air batteries provide much higher theoretical specific energies than Li-ion batteries (Table 1), which is attributed to the low-weight O_2 gas cathode and high-capacity metal anode.[2, 4-6] The practical specific energies of metal-air batteries are generally estimated by applying a reduction factor of 4–7 to the theoretical specific energies, as displayed in Fig. 1. The estimated practical specific energies of metal-air

Table 1. Theoretical gravimetric and volumetric energy densities of Li-ion and metal-air batteries. The discharge products for metal-air batteries are noted in parentheses. The energy density values are calculated based on the active components only.

System	Theoretical energy density (kWh/kg)	Theoretical energy density (kWh/L)	System	Theoretical energy density (kWh/kg)	Theoretical energy density (kWh/L)
$LiCoO_2$	1.07	5.45	Na-air (Na_2O_2)	1.60	4.48
$LiFePO_4$	0.60	2.14	Ca-air (CaO)	2.64	8.82
$LiMn_2O_4$	0.60	2.58	Li-air (Li_2O_2)	3.46	7.99
Zn-air (ZnO)	0.55	3.07	Mg-air (MgO)	3.92	14.04
Na-air (NaO_2)	1.10	2.43	Al-air (Al_2O_3)	4.31	16.81

batteries are comparable to or higher than those of Li-ion batteries, indicating that metal-air batteries can possibly serve as an energy storage system for full EVs.

Various studies have been conducted mainly on Li-air batteries among the other types of metal-air batteries because of their several advantages. First, Li-air batteries theoretically have a high specific energy of 3.4 kWh/kg. Second, the use of Li ions, which is the common feature of Li-ion and Li-air batteries, is likely to help in understanding the scientific and engineering transition from the commercialized Li-ion batteries to Li-air batteries. Early studies deployed carbonate-based electrolytes, which were typically used in Li-ion batteries. More recent studies in 2010 and 2011, however, reported that the organic carbonate electrolytes react with O_2 or discharge intermediates, resulting in the formation of Li_2CO_3 and CO_2 evolution.[14-16] Therefore, it has been challenging to find electrolytes that are stable against O_2 and discharge intermediates, facilitate the diffusion of O_2 and Li^+, and provide a proper range of voltage windows. Intensive computational and experimental studies have examined many organic solvent molecules, and ether- or sulfoxide-based electrolytes, such as dimethoxyethane (DME), tetraethylene glycol dimethyl ether (TEGDME), and dimethylsulfoxide (DMSO), have replaced carbonate electrolytes.[16-21]

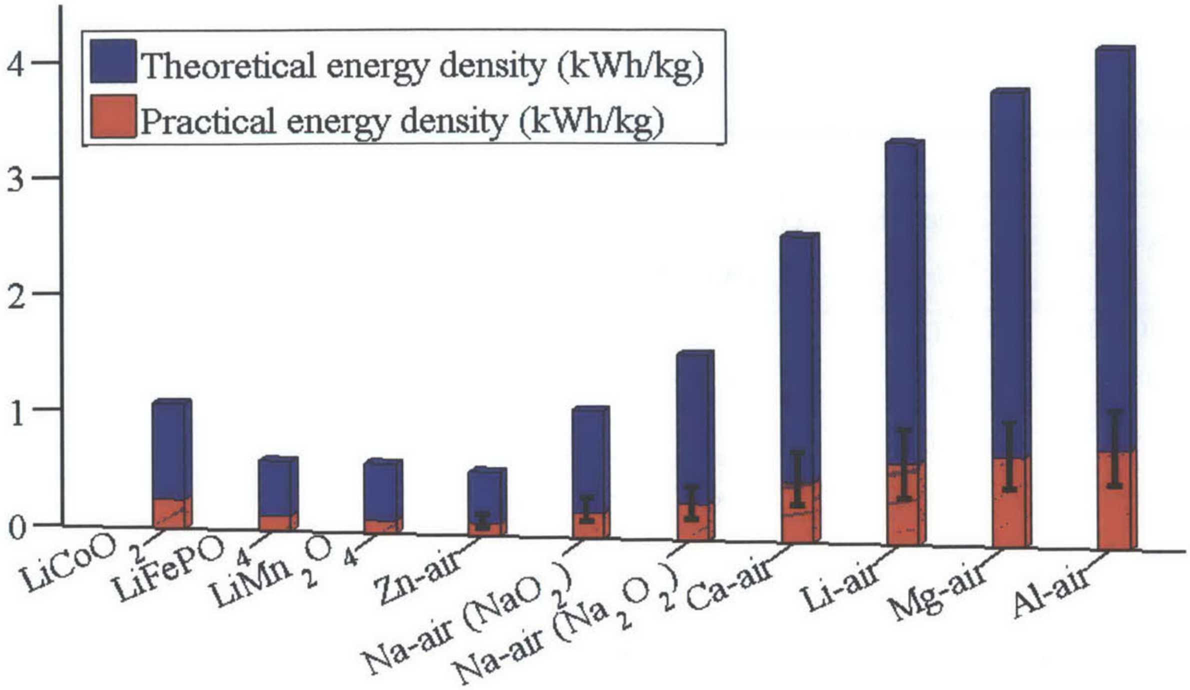

Figure 1. The theoretical and practical gravimetric energy densities of Li-ion and metal-air batteries. The practical energy densities of metal-air batteries are estimated by applying a reduction factor of 4–7 to the theoretical ones, and the error bars denote the range of the applied reduction factor.

Although the non-carbonate electrolytes slightly improved the performance of Li-air batteries by increasing their capacity, the high charging and discharging overpotentials and poor cyclability still remain, and these propensities suppress the power density of Li-air batteries. Lu *et al.*[22] proposed a O_2^- (superoxide)-involved discharge mechanism based on rotating disk electrode (RDE) measurements, and later, Peng *et al.*[23] validated this mechanism using surface enhanced Raman spectroscopy (SERS). This LiO_2 or O_2^- radical contributes to the poor rechargeability by reacting with the electrolytes and/or carbon electrode.[18, 24, 25] More details about the discharge and charge mechanisms can be found in Chapter 3.

Based on these findings, many researchers focused on replacing Li-air battery components such as catalysts, cathode materials, and electrolytes with ones that are more stable against a nucleophilic attack by the superoxide radical and enhance the kinetics. For instance, Peng *et al.*[26] deployed gold, which is relatively resistive to the parasitic side reactions, as a cathode support, and Riaz *et al.*[27] applied a Co_3O_4-doped Ni foam as a promising cathode support material for the $Li{-}O_2$ batteries. In addition, recently, Ottakam Thotiyl *et al.*[28] reported TiC, and Li *et al.*[29] suggested Ru nanoparticles deposited on a conductive indium tin oxide (ITO) as alternative cathode support materials, and both substitutes benefit from the absence of carbon and resulted in greatly improved performance of the $Li{-}O_2$ batteries.

In addition to the efforts to replace carbon cathode materials, recent studies have also focused on a redox shuttle that promotes electron transfer to enhance the reaction kinetics and thus lower the overpotentials. Chen *et al.*[30] achieved > 100 cycles with relatively low overpotentials by adding tetrathiafulvalene (TTF) as a redox mediator, and Lim *et at.*[31] reported up to 900 cycles under ~0.25 V overpotentials by employing a hierarchical nanoporous carbon nanotube as an air electrode and LiI as a redox mediator. To the best of our knowledge, this battery is the current state-of-the-art Li-air battery, exhibiting much improved cyclability (~900 cycles) and power density and a discharge capacity of 1000 mAh/g under a current rate of 2000 mAh/g.

Meanwhile, unlike Li-air batteries, other metal-air batteries are relatively less explored and remain in the early stage of development. While some metal-air batteries exhibit higher energy density than Li-air batteries, e.g., Mg- and Al-air batteries, these batteries are not electrochemically rechargeable and thus are not used as secondary batteries.[2, 4] On the other hand, Zn- and Na-air batteries not only exhibit lower theoretical specific energies than Li-air batteries but also suffer from dendrite formation of the metal anode in addition to the problems in Li-air batteries including but not limited to the stability of electrolytes, high overpotentials, and poor rate capability.[2, 32-35]

Most recently, promising battery performance has been reported in Na-air batteries, with charging and discharging overpotentials as low as < 0.2 V.[9, 10] This result triggered a new research direction in the field of metal-air batteries, especially for Na-air batteries. As can be seen from Table 1, Na-air batteries can hold more than one discharge product, NaO_2 and Na_2O_2, and the low charging and discharging overpotentials were observed only when NaO_2 is formed as a discharge product. As the performance of Na-air batteries highly depends on the type of the discharge product, understanding and controlling the formation mechanism of the discharge products are crucial. Therefore, we address this question in Part

Three. We would like to note that in addition to the discharge product issue, the typical problems in Li-air batteries also exist in Na-air batteries, such as the selection of electrolytes and electrode materials, understanding the discharging and charging mechanisms, and these need further follow-up studies and experiments.

Chapter 2. DFT Functionals and Fitting Energy Correction Method

Density functional theory ("DFT") is a computational modeling approach in quantum mechanics that is used to predict the charge density, and in turn, material properties in many-body systems. DFT is based on the idea that many-body interactions can be described by a unique charge density n and that the functionals of the charge density can determine the energy of the entire system. The functionals in DFT consist of the kinetic energy (T), potential energy (V), and electronic interaction energy (U). The kinetic energy functional of interacting electrons is decomposed into two sub-parts: the part representing the kinetic energy of non-interacting particles of density n (T_s, where s represents "single-particle") and the remainder. Similarly, the electronic interaction energy is divided into an electrostatic Hartree term (U_H) and the remainder. The remainders ($T-T_s$ and $U-U_H$) are combined and approximated in an exchange-correlation functional, E_{xc}. Therefore, the accuracy of DFT calculations depends on the design of E_{xc}. Here, we used the generalized gradient approximation ("GGA")[36] and the Heyd-Scuseria-Ernzerhof ("HSE") screened hybrid functional[37, 38] to model various oxidation states of Li–O and Na–O compounds, respectively.

2.1. GGA and HSE functionals

There are numerous exchange-correlation functional approximations. One can select a specific E_{xc} based on the purposes and systems to model, for instance, band structures in solids, binding energies of molecules, and compromises between the computational cost and accuracy. Among these bases of variations, the GGA functional approximates the charge density n as a combination of a uniform electron density and its local gradient. Together with the local density approximation ("LDA"), which assumes a uniform electron density, GGA is also so-called "(semi-) local." Despite their simplicity, the LDA and GGA functionals can achieve good agreement with experimental data in a wide range of materials. However, these (semi-)local functionals still have shortcomings, such as the under- and over-estimation of bonding energies in LDA and GGA, respectively, lack of van-der-Waals interactions, and self-interaction errors.

To overcome the weaknesses of LDA and GGA, theorists have attempted to add higher derivatives of the electron density to the exchange-correlation functionals to improve the accuracy of calculations, for example, meta-GGA where the Laplacian of the electron density is added.[39] Because it is not guaranteed that the order of derivatives of the electron density is necessarily related to the accuracy of the exchange-correlation functionals, another approach has been conceived: adding a fraction of exact exchange, Hartree-Fock ("HF"), into the GGA exchange-correlation. This theory is called a hybrid functional and has been intensively tested on many aspects of systems from energetics to electronic properties.[37, 40-43] The hybrid functionals require much more computational resources, such as memory and time, than the (semi-)local LDA and GGA functionals. However, the hybrid functionals are regarded as having superior performance compared with the conventional DFT functionals due to the cancellation of self-interaction errors by adding the non-local exact HF exchange.[37, 41-43]

The most popular hybrid functional for solids is HSE, for which the exchange terms are divided into short-range and long-range parts and described by HF and GGA exchanges:

$$E_{xc}^{\mathrm{HSE}} = \frac{1}{4}E_x^{\mathrm{HF,SR}}(\omega) + \frac{3}{4}E_x^{\mathrm{GGA,SR}}(\omega) + E_x^{\mathrm{GGA,LR}}(\omega) + E_c^{\mathrm{GGA}} , \qquad \text{Eq. (2-1)}$$

where ω is the screening parameter set to 0.207 Å^{-1} (0.11 bohr^{-1}) for HSE06,[44] to reduce the computational cost. The HSE functional is reported to perform better at predicting lattice constants, bulk moduli, formation energies, and band gaps.[40, 41]

Throughout this thesis, the Vienna ab-initio simulation package ("VASP")[45] and the projector augmented-wave ("PAW") approach[46] were used to calculate the total energy of Li–O and Na–O compounds with the GGA and HSE functionals, respectively.

2.2. Correction energy for oxides, peroxides, and superoxides[*]

It is well known that DFT predicts the formation energies of oxides (O^{2-}) less accurately than other properties. The overbinding of O_2 molecules in DFT calculations (6.04 eV in GGA and 5.17 eV in HSE) compared with the experimental value (5.12 eV) as

---

[*] This section has been accepted to *Chemistry of Materials* and *Nano Letters* for publication.

well as the electron transfer to form O^{2-} from O_2 are the main factors in the inaccuracy. Wang *et al.*[47] observed a constant energy shift of the formation energies from calculated values in GGA+U to experimental values for transition metal oxides, where the oxygen ions are in the O^{2-} state. In this method, the energy shift was observed to be −1.36 eV/O_2, and this correction energy was broadly applied to, for instance, the prediction of materials stability, oxidation/reduction energies, and particle morphology.[48-50]

Triggered by Wang *et al.*'s study,[47] several methods have been proposed to correct the formation energies of metal-oxygen systems, particularly those simultaneously involving oxides, peroxides and superoxides. Mo *et al.*[51] used the O_2 chemical potential that reproduces the experimental reaction energy between Li_2O_2 and Li_2O, and, Lee *et al.*[52] applied this approach to a Na–O system. On the other hand, Radin *et al.*[53] adopted the O_2 chemical potential from the experimental binding energy of the O_2 gas molecule. In addition, Hummelshøj *et al.* linked the O_2 chemical potential to the experimental formation energy of water,[54] and these authors later proposed a correction energy for oxides, peroxides, and superoxides, which is obtained by the linear regression of the calculated formation energies of compounds to their experimental formation enthalpies, as Wang *et al.*[47] performed. However, these researchers lumped oxides, peroxides, and superoxides together and ignored the different charge transfer natures depending on the oxygen valence states.[55]

Unfortunately, none of the above-proposed methods systematically corrects the energies in the different chemical environments, O^{2-}, O_2^{2-}, and O_2^{-}, originating from the O–O binding and electron transfer. Hence, we developed a correction method treating oxides, peroxides, and superoxides separately.[56, 57] We fitted the calculated formation energies of each oxygen valence state to its standard state experimental values, extended from the suggested method mentioned in Wang *et al.*[47]

The oxidation energy correction is obtained by calculating the formation energies of various non-transition metal oxides as

$$\Delta E_{\mathrm{form}} = E_{\mathrm{M}_x\mathrm{O}_y} - xE_{\mathrm{M}} - \tfrac{y}{2}E_{\mathrm{O}_2}, \qquad \text{Eq. (2-2)}$$

where E_i is the total energy calculated in DFT for a compound i at its reference state under the standard state (300 K and 1 atm). For example, E_{Li} and E_{Na} represent the total energy of Li and Na metal in the body-centered cubic structures, respectively, and E_{O_2} is the total energy of O_2 gas. These calculated formation energies are plotted versus the experimental formation enthalpies at the standard state obtained from NIST-JANAF[58] in Fig. 2. We used Li_2O, Na_2O, MgO, CaO, Al_2O_3, and K_2O for oxides; Li_2O_2, Na_2O_2, K_2O_2, and SrO_2 for peroxides; and NaO_2, KO_2, and RbO_2 for superoxides. From this plot in Fig. 2, the oxidation correction energies, E_{oxd}, were obtained as 1.33, 0.85, and 0.23 eV/O_2 in GGA and 1.05, 0.76, and 0.33 eV/O_2 in HSE for oxides, peroxides, and superoxides, respectively.

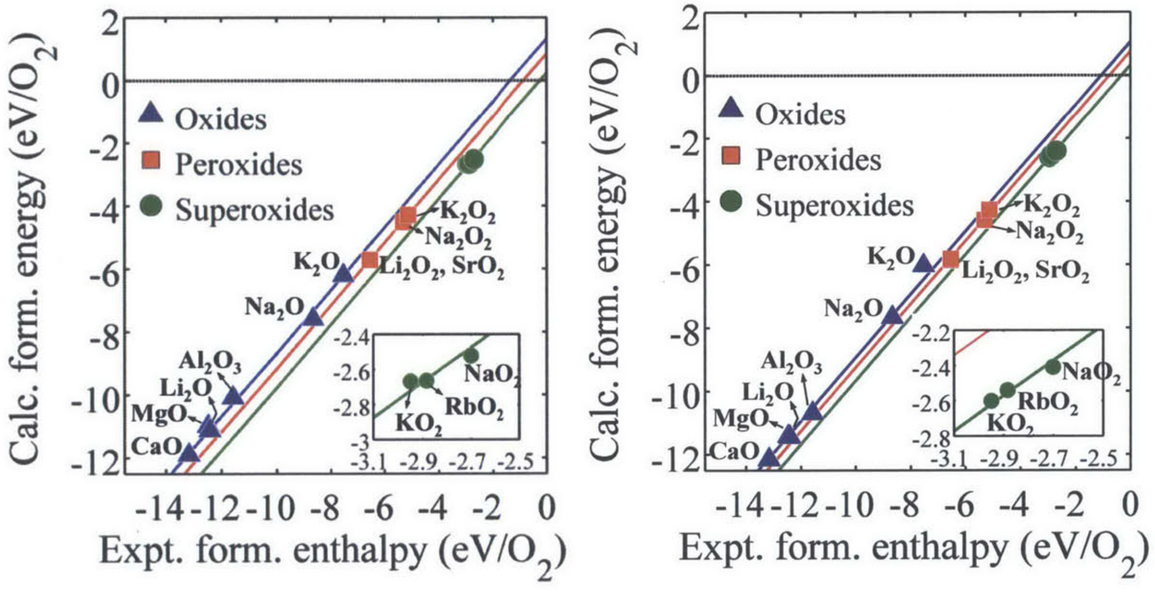

(a) (b)

Figure 2. The formation energies calculated in (a) GGA and (b) HSE plotted versus the experimental formation enthalpies at the standard state (300 K and 1 atm)[58] in eV/O_2 for oxides (blue triangles), peroxides (red squares), and superoxides (green circles). The data points corresponding to Li_2O_2 and SrO_2 overlap on this scale. The insets show zoomed-in formation energies for superoxides. The trend lines with slope = 1 are plotted for each group, and the oxidation energy correction is the y-intercept of each line. Reprinted with permission from Kang, S.; Mo, Y.; Ong, S. P.; Ceder, G. *Chemistry of Materials* **2013,** 25 (16), 3328-3336 and Kang, S.; Mo, Y.; Ong, S. P.; Ceder, G. *Nano Letters* **2014,** 14 (2), 1016-1020. Copyright 2014 American Chemical Society.

The correction energy differences between oxides and superoxides are 1.10 and 0.72 eV/O_2 in GGA and HSE, respectively, which indicates that the HSE functional performs slightly better than GGA in terms of the relative stability of oxides, peroxides, and superoxides. However, both the HSE and GGA functionals are unable to successfully predict accurate energies of metal-oxygen compounds. The origin of such errors is beyond the scope of this thesis. Thus, both functionals were used to evaluate the electrochemistry in Li–O and Na–O systems in this thesis, and the corresponding oxidation correction energy for each functional was applied.

PART TWO[‡]

Chapter 3. Literature Review: Charging and Discharging Mechanisms in Li-Air Batteries

Li-air batteries, in which Li^+ ions react with oxygen, represent an enticing novel rechargeable battery technology,[26, 59-61] offering the potential for a high theoretical specific energy due to their low weight and the high reaction energy of Li metal. However, the technology is still in its infancy, and the scientific and technical challenges remain to be overcome. These challenges are described in several good review papers.[7, 13, 62-65] It has been well established that the overall reaction in a $Li-O_2$ cell is the oxidation of Li to Li_2O_2 upon discharge and its subsequent reduction upon charge:[7, 13, 61-64, 66-68]

$$2Li^+ + O_2 + 2e^- \underset{\text{charge}}{\overset{\text{discharge}}{\rightleftarrows}} Li_2O_2. \qquad \text{Eq. (3-1)}$$

However, the details of the microscopic mechanisms in these reactions still remain mostly unknown, although such understanding is needed to optimize the rate and cycle life and decrease the large voltage polarization that is currently needed to operate the cell. In particular, the large voltage hysteresis leads to large energy losses and would exclude Li-air as a viable technology for EVs.[7, 13, 24, 26, 59-65]

While early work was often plagued by the reactivity of the discharge products with the electrolyte solvent,[14-16, 20, 69] recent experiments have slightly shifted their focus to appropriately stable electrolytes, which have demonstrated the overall reaction as the formation of Li_2O_2 with few byproducts in discharge.[15, 16, 26, 60, 66, 69] The reduction of dissolved O_2 to O_2^- reacting with Li^+ to make LiO_2 ("lithium superoxide") was demonstrated by in-situ surface enhanced Raman spectroscopy (SERS), and the LiO_2 species are not stable in the cell and disproportionate to Li_2O_2 and O_2 in the discharging process.[21, 23, 70] The

---

[‡] This part has been accepted to *Chemistry of Materials* for publication.

discharge curve is usually characterized by a relatively flat potential, which suggests a multiphase reaction process.[26, 59-61, 66, 71, 72]

On the other hand, less is understood about the process by which the cell recharges, only that it requires a substantial overpotential. Direct evidence has been provided by differential electrochemical mass spectrometry (DEMS) and various characterization techniques and has explained that the charging reaction involves the decomposition of Li_2O_2 to Li and O_2.[16, 26, 60, 67, 69, 73, 74] However, in contrast to the relatively flat potential in discharge, oxidization phenomena between 3.2 V and higher than 4 V have been observed in the charging process. [13, 26, 59, 60, 63, 64, 66-68, 71, 72, 75, 76]

More recent experiments have demonstrated that O_2 evolution begins at a relatively low charging voltage (as low as 3.1 V),[16, 26, 73, 74] and a clear plateau is observed at a voltage of 3.2–3.3 V in the charging curve.[26, 60, 74, 75, 77, 78] In addition, a significant fraction of capacity (~30–50% of total discharged capacity) has been observed to be charged at this low-voltage plateau,[26, 60, 74, 75, 77, 78] which is significantly lower than the previously reported charging voltage of 3.6 V to higher than 4 V. In addition, an improved rate capability is reported in these studies with low charging overpotential. For example, Refs. 26, 60, and 77 showed a ~10 fold improvement in the charging rate, and Ref. 16 demonstrated that the current associated with the peak at 3.2 V is 50–100% higher compared with current peaks at higher voltages.

This recent progress has shed light on one of the significant challenges of Li-air batteries, its high charging overpotential. A few charging mechanisms have been proposed to explain the low charging overpotential and improved kinetics. Representatively, Hummelshøj *et al.*[55] suggested the decomposition of Li_2O_2 particles at kink and step sites on surfaces to account for the low overpotential at the initial stage of charging. However, Hummelshøj *et al.* disregard the density of kink and step sites, which is expected to be small on Li_2O_2 particles, which are approximately hundreds of nanometers in diameter.[67, 79] More importantly, even if Li_2O_2 is preferentially removed at kink and step sites, this process will end as soon as the terrace that forms the kinks and steps is consumed in the charge.[7, 16, 60, 66, 74, 80] A charging mechanism that involves the formation of LiO_2 as an intermediate has been proposed by Lu and Shao-Horn,[81] and recent studies by Yang *et al.*[78] have reported the existence of LiO_2-like species in the discharged product. These LiO_2-like species were attributed to the superoxide-like O_2-rich surfaces of Li_2O_2 and/or the small clusters of Li_2O_2. The superoxides were observed to be the origin of the initial ~40% of charging capacity at a voltage plateau ~3.2–3.5 V and disappeared as soon as the sample was charged back to higher than 3.7 V. However, neither the decomposition path from Li_2O_2 through LiO_2 nor how this path can serve as a fast rate pathway at low overpotential has been clarified. Thus, numerous issues remain unsolved regarding what controls the overpotential and kinetics in oxidation.

To clarify this issue, we propose that a more facile path for Li_2O_2 charging exists that requires only approximately 370 mV of overpotential, which is in good agreement with experiments. At this relatively small overpotential, the discharge product Li_2O_2 is delithiated topotactically to form off-stoichiometric $Li_{2-x}O_2$ compounds. We find that the formation of these off-stoichiometric states is energetically favorable and is likely to be kinetically easy. The previously predicted good electronic and ionic conductivity[51, 53, 54, 82-85] in these off-stoichiometric states would further enhance delithiation until these products eventually break up into Li^+ and O_2 or O_2^- species, with possible dissolution in the electrolyte.[7, 24, 70, 86]

To prove this mechanism, we predict the crystal structures of LiO_2 and the intermediate compounds in the topotactic delithiation path for Li_2O_2 in Chapter 4.1 and calculate the energetics to pass through the off-stoichiometric $Li_{2-x}O_2$ compounds in Chapter 5.1.

Chapter 4. Structure Prediction for Metastable LiO_2 Phase

4.1. Methods

4.1.1. Computational setting and formation energy formula

The total energies of compounds were calculated using the HSE functional[37, 38] with the PAW method[46] in VASP.[45] In this method, the plane wave energy cutoff was set at 500 eV, and a *k*-point mesh was sampled with < 0.05 Å^{-1} *k*-points spacing. All the structures were relaxed until the total energies were converged to within 10^{-5} eV/atom.

The formation free energy of LiO_2 was calculated as

$$\Delta G_{f,\mathrm{LiO_2}} = E_{\mathrm{LiO_2}} - TS_{\mathrm{LiO_2}} - \left(E_{\mathrm{Li}} - TS_{\mathrm{Li}}\right) - \left(E_{\mathrm{O_2}} - TS_{\mathrm{O_2}}\right), \qquad \text{Eq. (4-1)}$$

where $E_{\mathrm{LiO_2}}$, E_{Li}, and $E_{\mathrm{O_2}}$ are the total energies of the LiO_2 compound, bulk metallic Li, and an O_2 molecule as computed in HSE, respectively, T is the temperature (298.15 K in this work), and $S_{\mathrm{LiO_2}}$, S_{Li}, and $S_{\mathrm{O_2}}$ are the entropies of the LiO_2 compound, bulk metallic Li, and O_2 gas, respectively. The entropies of Li metal and O_2 gas were obtained from the experimental values under standard conditions (298.15 K, 1 atm)[58], which are 0.30 meV/K and 2.13 meV/K per formula unit of Li and O_2, respectively. Because there is no measured entropy for bulk LiO_2, we approximated the entropy of solid state LiO_2 based on the entropy of other alkali metal superoxides (NaO_2 and KO_2) obtained from the CRC thermodynamics database,[87] which are 1.20 meV/K and 1.21 meV/K per formula unit of NaO_2 and KO_2, respectively, at the standard state. Even though the structures of NaO_2 and KO_2 are different (disordered $Pa\bar{3}$ cubic for NaO_2 and I4/mmm for KO_2) at the standard state, their formation enthalpies and entropies are very similar. In addition, our calculation indicates that the formation enthalpy of LiO_2 is also very close to that of NaO_2 and KO_2. Therefore, as an approximation, we adopted a value 1.21 meV/K per formula unit for the entropy of LiO_2.

4.1.2. Structure motifs for crystalline LiO_2

The structure of Li_2O_2 (Fig. 3(a)) consists of close-packed layers of Li ions stacked in an ABAC arrangement along the *c*-axis[88, 89] and O_2^{2-} dimers aligned along the *c*-axis straddling one of the Li layers. There are two symmetrically distinct Li sites in Li_2O_2, where we have labeled P (Li site in the O_2^{2-} layer) and L (Li site in the Li-only layer) in Fig. 3(a), and this notation will be used throughout this thesis. It has been previously established that the P sites are higher in energy in the Li_2O_2 structure, and therefore, the P sites tend to be the favorable sites to form Li vacancies.[54, 82, 90]

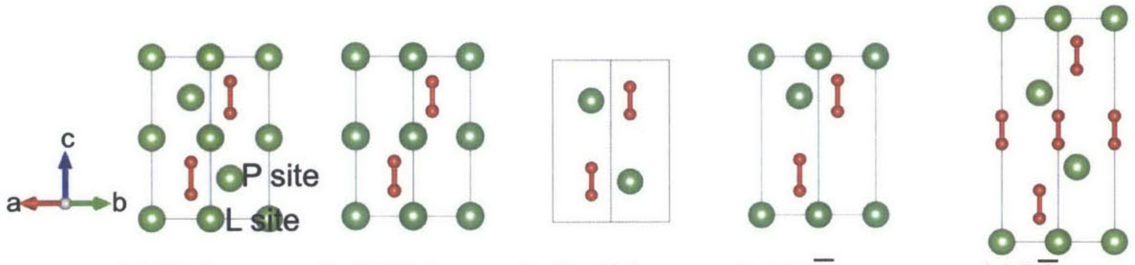

(a) P6_3/mmc Li_2O_2 (b-1) P6_3/mmc layered (b-2) P6_3/mmc monomers (b-3) P$\bar{3}$m disproportionated (c) R$\bar{3}$m (P3 layered)

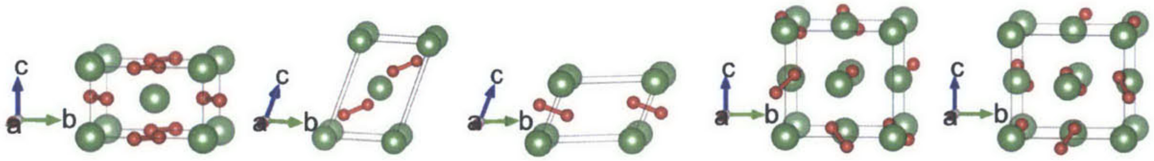

(d) Pnnm (e) C2/m (f) I4/mmm (g) Pa$\bar{3}$ (h) Pbca

Figure 3. The structure for Li_2O_2 (a) and candidate structures for LiO_2 (b-h). The green spheres represent Li ions, and the red spheres represent O ions. The oxygen bonds are marked as red bars. (a) Two distinct Li sites exist in the Li_2O_2 structure with the P6_3/mmc space group: a site that forms a Li-only layer (henceforth known as the "L" site) and a site in the plane that contains the O_2^{2-} bond centers (henceforth labeled as the "P" site). From (b) to (h), nine candidate LiO_2 structures are displayed accordingly. (b) The structures derived from Li_2O_2 by extracting two Li ions from a Li_2O_2 unit cell, which are labeled by their symmetry; (c) layered P3 structure by removing Na and replacing Co with Li from P3 $NaCoO_2$; (d) marcasite structure; (e) C2/m structure, where Li and O_2^- layers are alternately stacked; (f) I4/mmm structure, where LiO_2 dimers are arranged in a bipyramid structure; (g) pyrite structure; and (h) a structure in the Pbca space group, which has a similar arrangement of atoms as in the pyrite structure but in an orthorhombic lattice. Reprinted with permission from Kang, S.; Mo, Y.; Ong, S. P.; Ceder, G. *Chemistry of Materials* **2013,** 25 (16), 3328-3336. Copyright 2014 American Chemical Society.

While it is usually assumed that Li_2O_2 is stoichiometric, topotactic removal of Li with oxidation of O_2^{2-} to O_2^{-} is conceivable as both oxidation states of O_2 exist. As this oxidation removes an anti-bonding electron, it results in a decrease in the bond length of O_2, similar to the size change of a transition metal ion in a Li-ion intercalation cathode when it is oxidized. We also observe that the structure of Li_2O_2 is similar to that of P2 $NaCoO_2$.[91] The Li_2O_2 structure can be obtained by substituting Na and Co cations in P2 $NaCoO_2$ for Li ions and decreasing the O–O bond distance to form peroxide bonds. P2 $NaCoO_2$ is a well-known intercalation electrode material in Na-ion batteries, indicating that Li_2O_2 could undergo topotactic delithiation as well. More specifically, the oxidation of 2 O^{2-} to O_2^{2-} has recently been demonstrated computationally in Li_2MnO_3, lending further credence to the idea that topotactic Li removal with peroxide ion formation is possible in host structures.[92]

First, we investigated the relative stability of various LiO_2 structures, and then, we proceeded to determine the overpotential needed to form intermediates between LiO_2 and Li_2O_2. Nine possible structure types were evaluated as the possible ground state for LiO_2:

1) Three symmetrically distinct structures are obtained by extracting two Li atoms from a single Li_2O_2 unit cell (from Figs. 3(b-1) to 3(b-3)). The Li_2O_2 derivatives in Fig. 3(b) are labeled by the symmetry of the relaxed structure and a descriptor of the main structure feature. For example, the structure labeled *$P6_3/mmc$-layered* in Fig. 3(b-1) has alternating Li and O_2 layers stacked along the *c*-axis. The *$P6_3/mmc$-monomer* structure in Fig. 3(b-2) is comprised of LiO_2 monomers. The *$P\bar{3}m$-disproportionated* structure in Fig. 3(b-3) is named after the fact that its relaxed final structure is a "disproportionated state" that resembles ½ Li_2O_2 + ½ O_2 (see Chapter 5.1 for details).

2) A $R\bar{3}m$ (P3 layered) structure is obtained by removing Na and replacing Co with Li from the layered P3 $NaCoO_2$ structure (Fig. 3(c)).[91] Given the structural similarity between Li_2O_2 and P2 $NaCoO_2$, we investigated this analogue of the P3 structure as a candidate structure for the ground state LiO_2.

3) The additional structures in Figs. 3(d) to 3(h) are obtained by substituting metal ions with Li in known superoxides and peroxides with AO_2 stoichiometry, such as NaO_2, KO_2, RbO_2, and CsO_2 as known superoxides and BaO_2, CaO_2, CdO_2, HgO_2, MgO_2, SrO_2, and ZnO_2 as known AO_2 stoichiometry peroxides.

4.2. Results

4.2.1. Calculated energies of LiO_2 bulk structures

The computed HSE formation free energies for the candidate structures of LiO_2 are plotted in Fig. 4 based on Eq. (4-1). We find that the marcasite structure in the Pnnm space group (Fig. 3(d)) is the ground state structure for LiO_2 with a formation free energy of −2.68 eV/O_2. The ground state structure is consistent with an experimental diffraction study of LiO_2 at 4.2 K[93] and with previous computational studies on a small number of possible structures.[94, 95]

Furthermore, we find that LiO_2 is not thermodynamically stable when the oxygen energy is set to represent O_2 gas at 1 atm and 298.15 K, as the lowest free energy at that composition is a combination of ½ Li_2O_2 + ½ O_2. This result indicates that Eq. (3-1) is truly the thermodynamically favored reaction at this condition,[94, 95] which is consistent with LiO_2 being observed to disproportionate into Li_2O_2 and O_2 during discharge.[23, 26] Nevertheless,

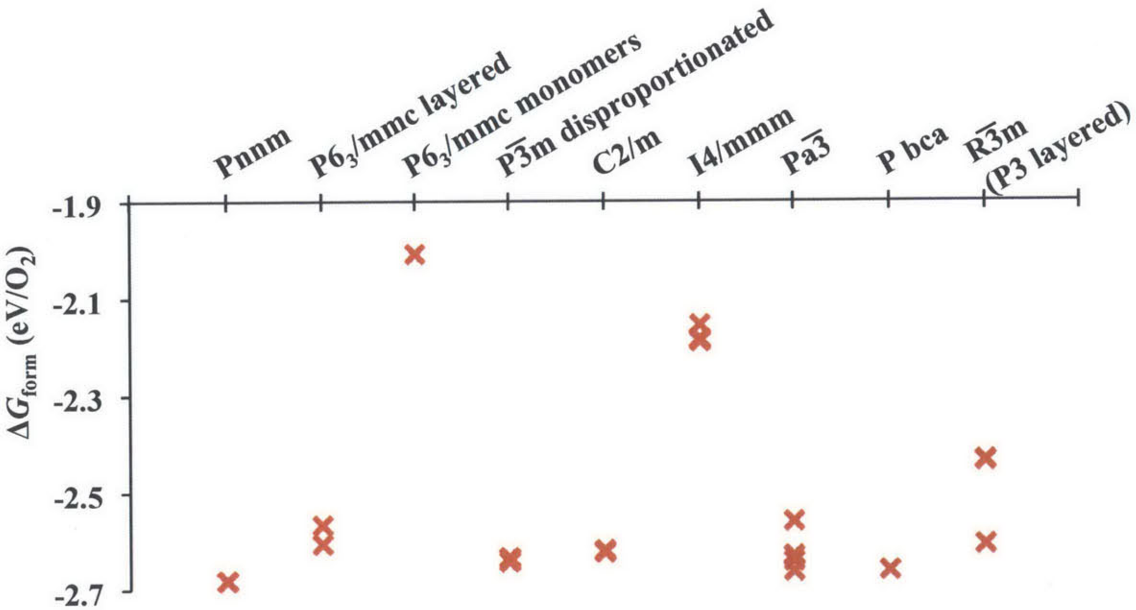

Figure 4. The calculated formation free energy (in eV/O_2) of the different structures considered for LiO_2. Multiple data-points indicate the energies computed from different initial structures, such as NaO_2, CsO_2, and MgO_2, or from different magnetic states. The lowest energy structure is Pnnm (−2.68 eV/O_2). Reprinted with permission from Kang, S.; Mo, Y.; Ong, S. P.; Ceder, G. *Chemistry of Materials* **2013,** 25 (16), 3328-3336. Copyright 2014 American Chemical Society.

note that this result will depend on the applied O_2 chemical potential. At high enough O_2 chemical potentials, which can be a high O_2 partial pressure and/or low temperature, it is possible for LiO_2 to be thermodynamically stable.

The three LiO_2 structures derived from $P6_3/mmc$ Li_2O_2 are of special interest in this study as these structures could be easily created by topotactic delithiation of Li_2O_2 during charging. Among these structures, we select to neglect the $P\overline{3}m$*-disproportionated* structure because it is a "disproportionated state," which resembles ½ Li_2O_2 + ½ O_2. The disproportionation is confirmed by the fact that the lengths of two O_2 bonds in the unit cell are split into 1.21 Å and 1.51 Å, which are the typical bond lengths of O_2 and O_2^{2-}, respectively. When neglecting this structure, the *$P6_3/mmc$-layered* structure has the lowest energy among the structures derived from topotactically delithiating Li_2O_2. The formation free energy of the *$P6_3/mmc$-layered* structure, −2.61 eV/O_2, indicates that topotactic removal of Li from Li_2O_2 is not much higher in energy than the formation of the LiO_2 ground state.

4.2.2. Phonon spectra for LiO_2 bulk structures

To investigate the dynamic stability of LiO_2 structures, we computed the phonon spectra of LiO_2 in its ground state Pnnm structure and topotactically delithiated *$P6_3/mmc$-layered* structure. The phonon calculations for LiO_2 were performed based on the small displacement method within the harmonic approximation using the PHON code.[96] Symmetrically distinct displacements of atoms by 0.04 Å were introduced in a 3 × 3 × 3 supercell for Pnnm LiO_2 and a 3 × 3 × 2 supercell for *$P6_3/mmc$-layered* LiO_2. The lattice parameters and atomic positions of these supercells were optimized in GGA. The unit cells of both structures were relaxed until the total energies and forces were converged to within 10^{-7} eV and 10^{-3} eV/Å per formula unit, respectively, and the phonon density of states ("DOS") was computed using a 25 × 20 × 30 and 30 × 30 × 18 q-points grid for Pnnm and *$P6_3/mmc$-layered* LiO_2, respectively. To maintain reasonable computational costs, the phonon calculations were performed using the GGA functional instead of the HSE functional.

No imaginary vibrational frequency appears in the computed phonon dispersion in either Pnnm or *$P6_3/mmc$-layered* LiO_2 (Fig. 5), which suggests that both LiO_2 structures are dynamically stable. The phonon spectra of Pnnm and *$P6_3/mmc$-layered* LiO_2 exhibit some common features, such as *i)* a broad phonon band at low frequencies, which is relatively flat in the wave vector space and has contributions from both cations and anions; *ii)* a wide phonon band gap in the range of 380 to 970 cm^{-1} for Pnnm and of 410 to 1085 cm^{-1} for *P6₃/mmc-layered*; and *iii)* a localized phonon band at high frequencies arising from the O_2^- anions. The O_2^- vibration modes have higher frequencies for *P6₃/mmc-layered* LiO_2 (ranging from 1085 to 1290 cm^{-1}) than for Pnnm (ranging from 970 to 1173 cm^{-1}), indicating that the O_2^- bonds in *P6₃/mmc-layered* LiO_2 are stronger than those in Pnnm LiO_2.

The peak frequency of the O_2^- vibrational mode in the phonon DOS (Fig. 5) is located at 1089 cm^{-1} for *P6₃/mmc-layered* LiO_2, which is comparable to the experimentally detected O−O stretching frequencies of LiO_2 monomer gas (1094 cm^{-1})[97, 98] and an isolated O_2^- radical (1090 cm^{-1}).[99] More importantly, the O_2^- vibrational mode in *P6₃/mmc-layered* LiO_2 agrees with the Raman peak for LiO_2-like species at 1125 cm^{-1} observed at the end of discharge of Li-air batteries.[78] On the other hand, the peak frequency of the O_2^- vibrational mode in Pnnm is located at 996 cm^{-1}. This frequency is significantly lower than the value of 1103 cm^{-1} reported in previous computational works, which analyzed the Γ-X-S-Y-Γ segment for Pnnm LiO_2.[78, 95] Our lower frequencies, however, occurred along the Z-U-R-T-Z high symmetry *q*-lines for the O_2^- phonon branch, which was not reported in the previous work.[95] Therefore, the LiO_2 in the *P6₃/mmc-layered* structure rather than Pnnm structure could be a possible structure that accounts for the peak at 1125 cm^{-1} observed in the Raman spectrum during the operation of the Li−O_2 battery.[78]

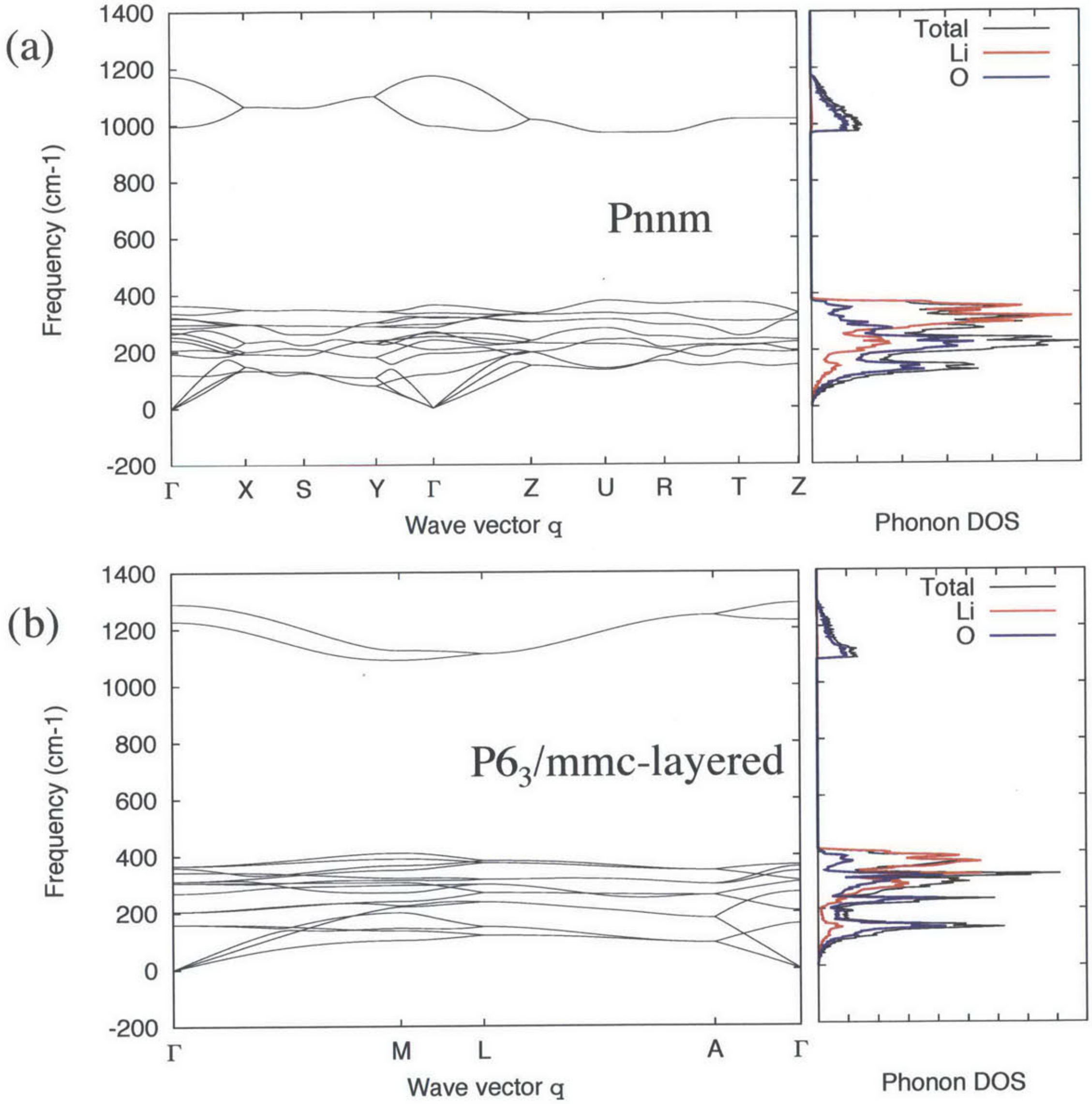

Figure 5. Phonon dispersion and density of states for LiO_2 in the (a) Pnnm and (b) *P6$_3$/mmc-layered* structures. The partial phonon density of states contributed from Li and O are represented in red and blue, respectively. Reprinted with permission from Kang, S.; Mo, Y.; Ong, S. P.; Ceder, G. *Chemistry of Materials* **2013,** 25 (16), 3328-3336. Copyright 2014 American Chemical Society.

Chapter 5. Understanding the Charging Mechanism in Li-Air Batteries

To understand the energetics of our proposed charging mechanism, "topotactic delithiation of Li_2O_2," we predicted the lowest energy compounds between Li_2O_2 and LiO_2 and calculated the voltage steps starting from Li_2O_2.

5.1. Methods

5.1.1. Formation free energy and voltage formalism

The formation free energies of $Li_{2-x}O_2$ intermediate compounds ($0 < x < 1$) during charging as well as Li_2O, Li_2O_2, and LiO_2 stoichiometric compounds were computed with respect to elemental chemical potentials as follows:

$$\Delta G_{f,\,\mathrm{Li}_a\mathrm{O}_b} = E_{\mathrm{Li}_a\mathrm{O}_b} - TS_{\mathrm{Li}_a\mathrm{O}_b} - a\left(E_{\mathrm{Li}} - TS_{\mathrm{Li}}\right) - \tfrac{b}{2}\left(E_{\mathrm{O}_2} - TS_{\mathrm{O}_2}\right), \qquad \text{Eq. (5-1)}$$

where $E_{\mathrm{Li}_a\mathrm{O}_b}$ is the total energy of the Li_aO_b compound computed in HSE, T is 298.15 K, and $S_{\mathrm{Li}_a\mathrm{O}_b}$ is the entropy of the Li_aO_b compound. The entropies of Li_2O, Li_2O_2, Li metal, and O_2 gas were obtained from the experimental values under the standard conditions (298.15 K, 1 atm),[58] which are 0.39 meV/K, 0.59 meV/K, 0.30 meV/K, and 2.13 meV/K per formula unit of Li_2O, Li_2O_2, Li, and O_2, respectively. The entropies of the intermediate states $Li_{2-x}O_2$ ($0 < x < 1$) were obtained by linearly interpolating the entropies of Li_2O_2 and LiO_2. The linear interpolation of entropy values is a crude approximation; however, given that the low energy structures we are primarily interested in are "phase-separated" forms (see Chapter 5.1.2), the approximation should be relatively valid. The equilibrium voltage between intermediate compounds during charging, $Li_{2-x_1}O_2$ and $Li_{2-x_2}O_2$, is given by the following expression:[100]

$$\phi = -\frac{\Delta G_{f,\mathrm{Li}_{2-x_1}\mathrm{O}_y} - \Delta G_{f,\mathrm{Li}_{2-x_2}\mathrm{O}_y}}{(x_2 - x_1)F}, \qquad \text{Eq. (5-2)}$$

where F is the Faraday constant.

5.1.2. Prediction of off-stoichiometric compounds $Li_{2-x}O_2$

To determine whether topotactic removal of Li ions from Li_2O_2 is possible at the early stage of charging, we evaluated the energies of the off-stoichiometry compositions, $Li_{1.75}O_2$, $Li_{1.50}O_2$, and $Li_{1.25}O_2$. For each of the intermediate compositions, a reasonable number of candidate structures was considered by taking into account different arrangements of Li atoms and vacancies, which were generated as follows:

1) Two symmetrically distinct structures for $Li_{1.50}O_2$ are generated by removing one Li atom from P or L site in a single unit cell of Li_2O_2 (see Fig. 3(a)).

2) All symmetrically distinct arrangements of Li ions and vacancies in the 1 × 1 × 2 and 2 × 1 × 1 supercells of Li_2O_2 were considered. These arrangements yield six, twelve, and thirty structures for the $Li_{1.75}O_2$, $Li_{1.50}O_2$, and $Li_{1.25}O_2$ compositions, respectively.

3) The "phase-separated structures" are further investigated in the 1 × 1 × 4 and 4 × 1 × 1 supercells. The phase-separated structures are comprised of distinct domains of pure Li_2O_2 and LiO_2 compositions. Among the phase-separated structures, some specific

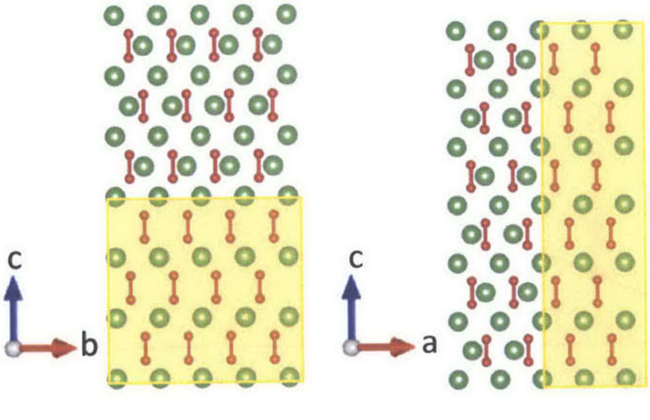

(a) (b)

Figure 6. (a) A *layered* structure of $Li_{2-x}O_2$ ($0 < x < 1$), where the Li_2O_2 and LiO_2 phases are separated by the *a-b* plane, and (b) a *channel* structure of $Li_{2-x}O_2$ ($0 < x < 1$), where the Li_2O_2 and LiO_2 phases are separated by the *a-c* or *b-c* planes. Yellow shading is used to highlight LiO_2 regions distinguished from Li_2O_2. Reprinted with permission from Kang, S.; Mo, Y.; Ong, S. P.; Ceder, G. *Chemistry of Materials* **2013,** 25 (16), 3328-3336. Copyright 2014 American Chemical Society.

structures are labeled as *layered* (Fig. 6(a)) and *channel* (Fig. 6(b)) structures. In the *layered* structure, the domain boundaries are parallel to the *a-b* plane, whereas the domain boundaries are in the *a-c* or *b-c* planes in the *channel* structure. We calculated eight $Li_{1.75}O_2$, nine $Li_{1.50}O_2$, and eight $Li_{1.25}O_2$ phase-separated structures.

In total, we considered 14, 23, and 38 symmetrically distinct structures for $Li_{1.75}O_2$, $Li_{1.50}O_2$, and $Li_{1.25}O_2$ compositions, respectively.

5.2. Results

Fig. 7 shows the energy of a large number of structures between compositions Li_2O_2 and LiO_2 relative to the equilibrium Li_2O_2–O_2 tie line. Surprisingly, there are multiple off-stoichiometric $Li_{2-x}O_2$ configurations that have relatively low energy above the equilibrium state. We find that all the lowest energy off-stoichiometric structures are *layered* structures of the type depicted in Fig. 6(a), where LiO_2 and Li_2O_2 domains are separated by a boundary in

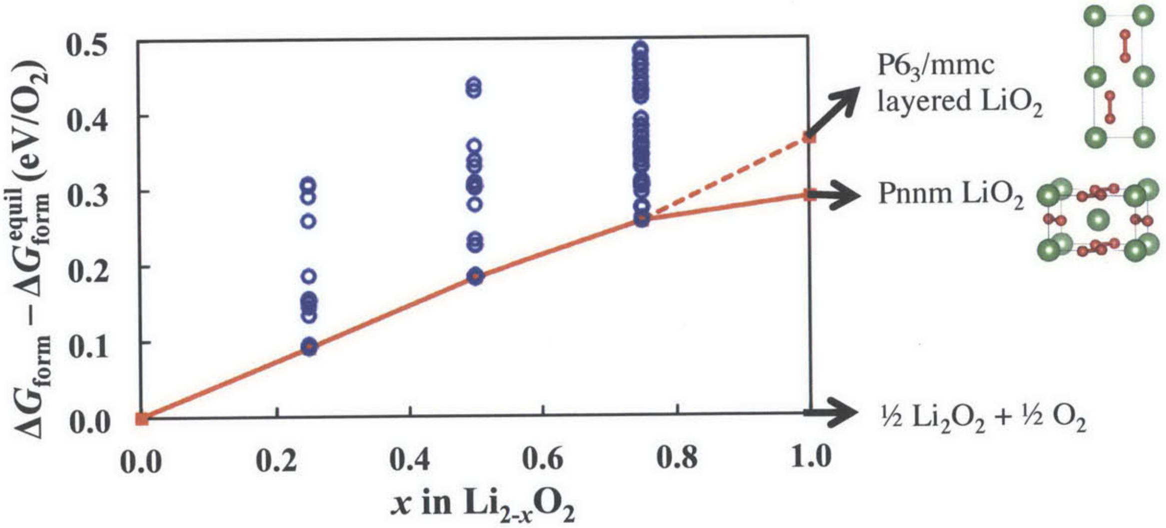

Figure 7. The formation free energy (eV/O_2) of the off-stoichiometry $Li_{2-x}O_2$ structures referenced to the equilibrium in Eq. (3-1). The red solid line connects the lowest energy off-stoichiometry $Li_{2-x}O_2$ structures starting from Li_2O_2 with the ground state structure of LiO_2 (Pnnm), whereas the red dashed line ends with the topotactically delithiated *P6₃/mmc-layered* LiO_2 structure. Reprinted with permission from Kang, S.; Mo, Y.; Ong, S. P.; Ceder, G. *Chemistry of Materials* **2013,** 25 (16), 3328-3336. Copyright 2014 American Chemical Society.

the *a-b* plane. The lowest energy structures are shown in Fig. 8, and their calculated formation enthalpies and lattice parameters are summarized in Table 2. In all these structures, Li atoms are extracted from the layers that contain the peroxide centers, i.e., P sites. Such layer-by-layer Li extraction allows the nearby O_2^- groups to relax without interfering with the O_2^{2-} groups in other layers. As more Li atoms are extracted, more so-called "superoxide" layers are formed. Our results indicate that the lowest energy structures tend to group peroxides and superoxides in layers, most likely to minimize strain. However, the energy of

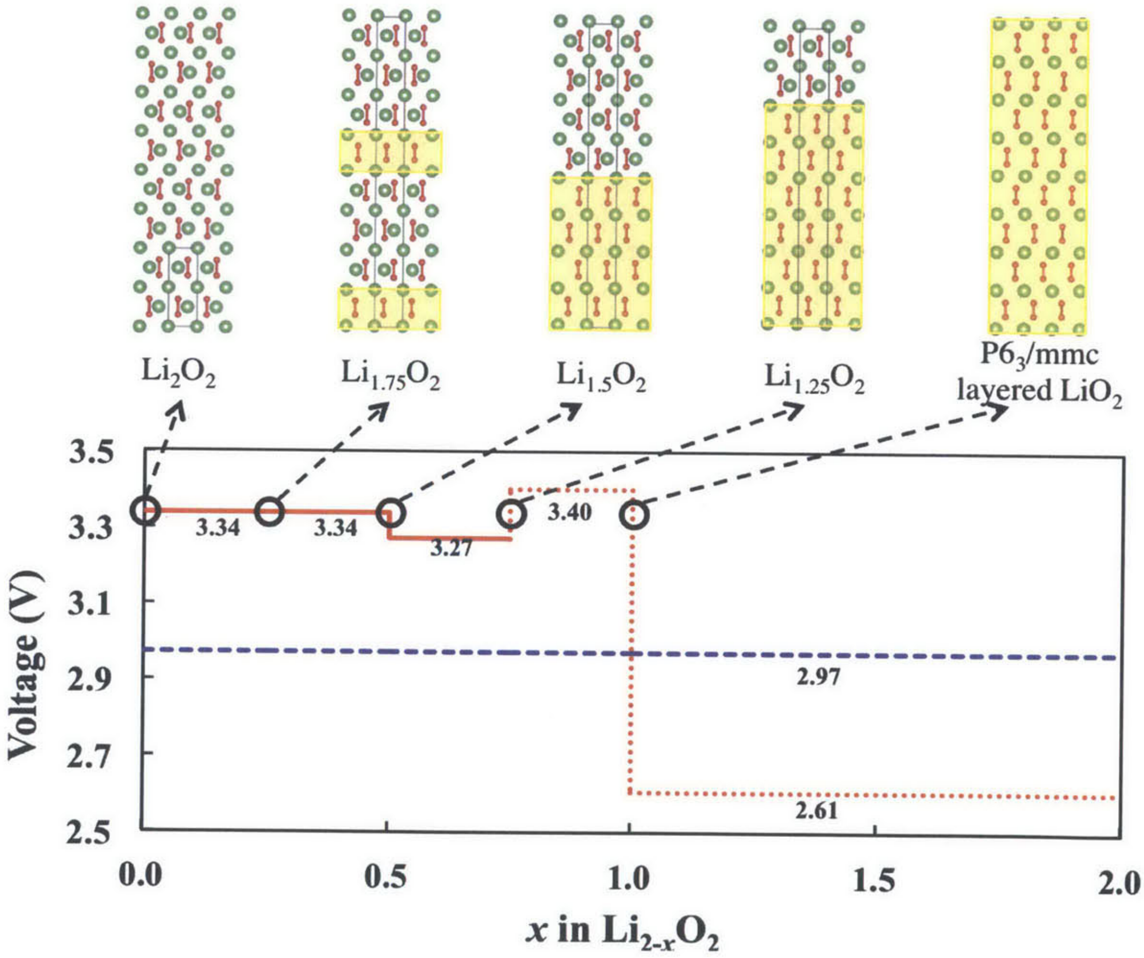

Figure 8. The non-equilibrium voltage profile from Li_2O_2 ($x = 0$) to O_2 ($x = 2$). The red solid and dotted line indicates the predicted topotactic oxidation path. The dashed blue line denotes the direct decomposition of Li_2O_2 into 2 Li^+ + 2 e^- + O_2. The lowest energy structures are shown along the path. Reprinted with permission from Kang, S.; Mo, Y.; Ong, S. P.; Ceder, G. *Chemistry of Materials* **2013,** 25 (16), 3328-3336. Copyright 2014 American Chemical Society.

structures when they are grouped but not layered, such as *channel* structures, is only marginally higher than that of the layered ones (see Fig. 9).

Fig. 8 compares the calculated voltage profile for the thermodynamically stable path (blue) and for the metastable path formed from delithiating Li_2O_2 (red). The calculated equilibrium voltage of 2.97 V for the decomposition of Li_2O_2 to $2\ Li^+ + 2\ e^- + O_2$ agrees with the experimental value of 2.96 V.[58] As to the metastable topotactic delithiation path, the predicted voltage plateau at 3.34 V is consistent with the experimentally observed charging voltage plateau at 3.1−3.3 V,[16, 26, 60, 73-75] designating that these off-stoichiometric structures are certainly accessible in the charge process. Because the topotactic delithiation is a non-equilibrium path, its initial charging voltage is above the equilibrium voltage and behaves

Table 2. The calculated formation enthalpy in eV per formula unit, experimental entropy in meV/K per formula unit, and oxidation energy correction in eV per formula unit obtained in Chapter 2.2 for Li metal, O_2 gas, and Li−O compounds. The formation enthalpies of the intermediate compounds, $Li_{1.75}O_2$, $Li_{1.50}O_2$, and $Li_{1.25}O_2$, are obtained from the lowest energy structures in Fig. 8, and their entropies and oxidation energy correction are linearly interpolated from Li_2O_2 and LiO_2. Reprinted with permission from Kang, S.; Mo, Y.; Ong, S. P.; Ceder, G. *Chemistry of Materials* **2013,** 25 (16), 3328-3336. Copyright 2014 American Chemical Society.

Compounds	Calculated $\Delta \boldsymbol{H}_{\text{form}}$ without correction (eV)	Experimental S (meV/K)	Oxidation energy correction (eV)
Li	0.00	0.30	-
Li_2O	−5.72	0.39	0.53
Li_2O_2	−5.82	0.59	0.76
$Li_{1.75}O_2$	−5.03	0.74	0.65
$Li_{1.50}O_2$	−4.23	0.90	0.55
$Li_{1.25}O_2$	−3.45	1.05	0.44
Pnnm LiO_2	−2.72	1.21	0.33
$P6_3$/mmc-layered LiO_2	−2.64	1.21	0.33
O_2	0.00	2.13	-

non-monotonically as the charging proceeds. This result is unlike an equilibrium oxidation profile, which must have a non-decreasing voltage to satisfy thermodynamic stability conditions. The initially higher voltage of the topotactic path must be compensated by a lower voltage at the end of charge because the average voltage for two paths between the same compounds is a conserved quantity. However, any decrease in voltage along a charging path will lead to instabilities and current localization in the electrode and, hence, will not be directly observed, as described in Chapter 5.3.

Figure 9 (next page). The formation energy (eV/O_2) of (a) $Li_{1.75}O_2$ (b) $Li_{1.50}O_2$ and (c) $Li_{1.25}O_2$ referenced to the equilibrium phases in Eq. (3-1). The "layered" structures have the lowest energy, followed by the "channel" and other "phase-separated" structures. The "solid solution" structures are highest in energy. Representative structures for each group are inserted with superoxide regions highlighted by yellow boxes. The lowest-energy layered structures are displayed in Fig. 8, and their energies are listed in Table 2. Reprinted with permission from Kang, S.; Mo, Y.; Ong, S. P.; Ceder, G. *Chemistry of Materials* **2013,** 25 (16), 3328-3336. Copyright 2014 American Chemical Society.

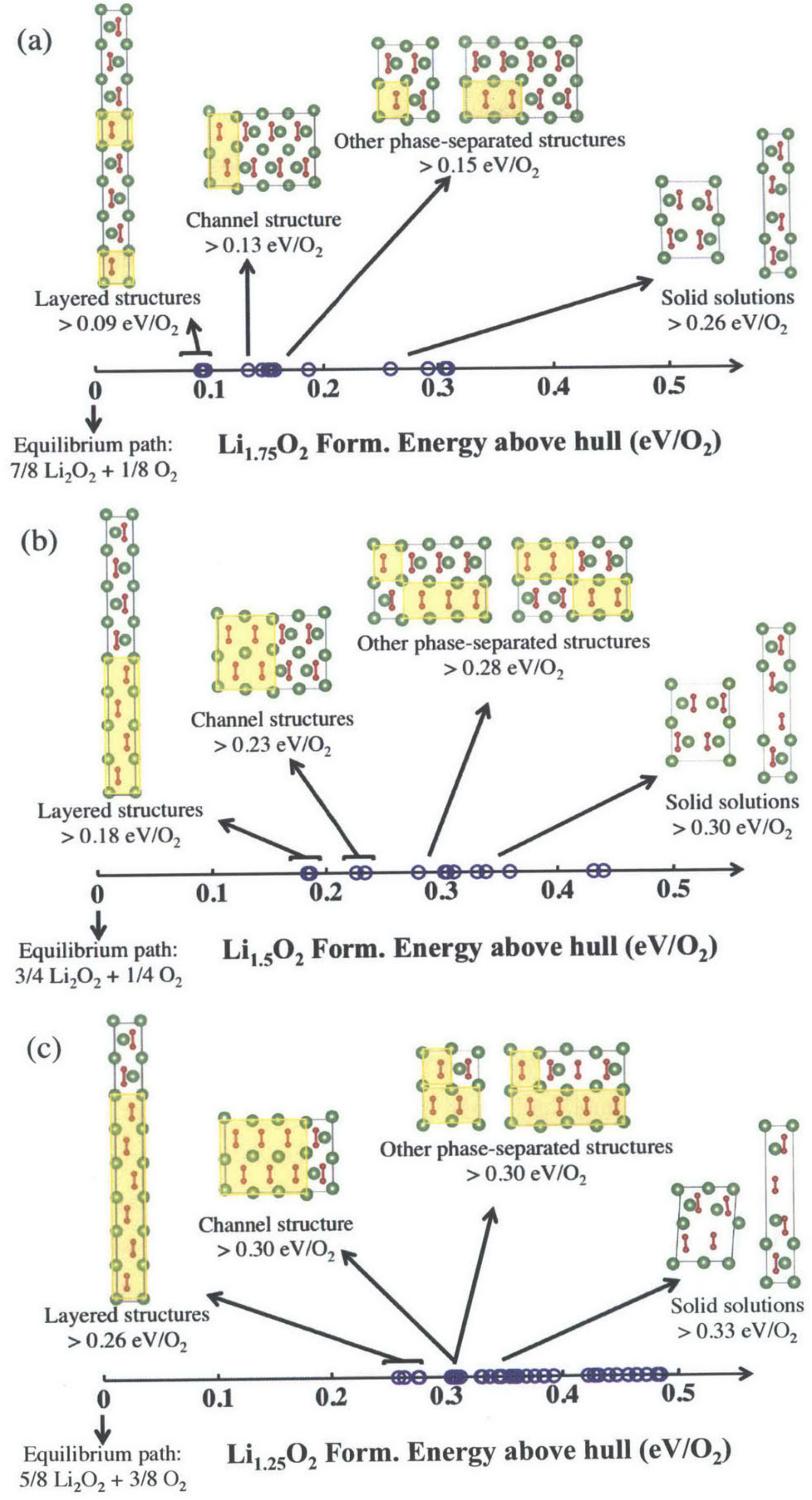
(a)
Layered structures
> 0.09 eV/O_2
Channel structure
> 0.13 eV/O_2
Other phase-separated structures
> 0.15 eV/O_2
Solid solutions
> 0.26 eV/O_2
0
0.1
0.2
0.3
0.4
0.5
Equilibrium path:
7/8 Li_2O_2 + 1/8 O_2
$Li_{1.75}O_2$ Form. Energy above hull (eV/O_2)
(b)
Layered structures
> 0.18 eV/O_2
Channel structures
> 0.23 eV/O_2
Other phase-separated structures
> 0.28 eV/O_2
Solid solutions
> 0.30 eV/O_2
0
0.1
0.2
0.3
0.4
0.5
Equilibrium path:
3/4 Li_2O_2 + 1/4 O_2
$Li_{1.5}O_2$ Form. Energy above hull (eV/O_2)
(c)
Layered structures
> 0.26 eV/O_2
Channel structure
> 0.30 eV/O_2
Other phase-separated structures
> 0.30 eV/O_2
Solid solutions
> 0.33 eV/O_2
0
0.1
0.2
0.3
0.4
0.5
Equilibrium path:
5/8 Li_2O_2 + 3/8 O_2
$Li_{1.25}O_2$ Form. Energy above hull (eV/O_2)

5.3. Implication to the charging mechanism in Li-air batteries

People tend to think of polarization in electrochemical experiments as the extra force required to drive the equilibrium reaction forward (e.g., to overcome nucleation barriers, Li^+ or electron transport problems, or catalytic barriers). Unlikely, our results demand a different viewpoint: when the equilibrium voltage is applied, the chemical potential of Li in the system allows only the equilibrium reaction to proceed. However, once an overpotential is applied, the number of accessible paths becomes much larger: any path along which the required voltage remains below the applied voltage can be used by the system. Out of all these possible reaction paths, the one that proceeds the fastest is the one the system will pick. One should, therefore, think of the overpotential as "enabling more reactions paths," rather than making the thermodynamic path faster. Similar arguments have been made to understand conversion reactions[101] and the rapid kinetics of the first-order phase transition in $LiFePO_4$ upon charging and discharging.[102]

An off-stoichiometric path is likely to be a facile path for transformation. Multiple theoretical studies indicate that once vacancies are created, the mobility of a Li vacancy in Li_2O_2 is high with a migration energy barrier of ~0.3–0.4 eV.[53, 54, 83] In addition, the energy to create Li vacancies has been predicted to be as low as ~0.1 to 0.3 eV on the top layer of Li_2O_2 surfaces.[51, 55] Removal of Li^+ also creates electronic holes that have a reasonably low activation barrier for motion.[82] Therefore, reliable electronic conductivity can be expected in off-stoichiometric peroxide particles.

We first discuss the mechanism by which a single particle of Li_2O_2 can decompose, and then, the consequences for the multi-particle electrode behavior are evaluated. To charge Li_2O_2, both Li and O must be removed. Because it has typically been assumed that Li_2O_2 is stoichiometric, both Li and O must be removed at the same rate from the particle, apart from stoichiometry variations in the surface layer.[51] Our results indicate that simultaneous O and Li removal is not the only option. We find that off-stoichiometric delithiation with local superoxide ion formation in the material can proceed at a low overpotential without leading to mechanical instability in the structure. The off-stoichiometric phase is easy to form during charging, given the low formation energy of bulk $Li_{2-x}O_2$ phases, which is thermodynamically accessible under a small overpotential. More importantly, the attraction among Li vacancies and the energetic preference of Li vacancies to P sites facilitates the clustering of Li vacancies and the nucleation of LiO_2 layers in the Li_2O_2 framework (Figs. 6 and 8). Because the mobility of Li^+ is expected to be good in the off-stoichiometric material as well as in the electrolyte, while the O_2 evolution from the surface appears to be hindered by a substantial energy barrier,[51] it is likely that O_2 removal lags behind Li removal, creating off-stoichiometric $Li_{2-x}O_2$ states in a particle. The nature of degree of off-stoichiometry "x" depends on the relative O_2 versus Li removal rates and hence on the particle size, electronic wiring, and electrolyte. In the limit where O_2 removal is very slow, a particle will be homogenously delithiated until it reaches a critical value of x, where it starts to release O_2 gas or dissolve in the electrolyte. However, we argue below that even under this scenario, such metastable off-stoichiometric states may be difficult to observe as they lead to particle-by-particle inhomogeneous reactions. Nonetheless, these states are critical to understand the kinetics and atomistic-level mechanism of Li_2O_2 charging.

Our findings apply to the reaction path that a single Li_2O_2 particle takes. How such single particle behavior manifests itself at the macroscopic electrode scale, which consists of a large number of interacting particles, depends on the shape of the voltage profile and on the electrode construction. An important consequence is that the non-monotonic topotactic voltage profile in Fig. 8 will lead to an inhomogeneous reaction of the electrode (see Fig. 10). Apart from the small voltage increase as x reaches 0.75 in Fig. 8, the voltage is either constant or decreasing as the charge proceeds, indicating that once delithiation of the peroxide starts, it will continue rapidly and locally (under constant applied voltage) because the driving force for Li removal *increases* with increasing state of charge (a condition opposite to a thermodynamic equilibrium path). Once this reaction starts in a particle, it will continue at the maximum rate consistent with the Li^+ and hole mobility in the solid. At some level of delithiation, this particle will become unstable and either dissolve in the electrolyte or release O_2 gas. Fig. 7 shows that the excess energy (above the equilibrium) of the delithiated peroxide increases with x, indicating that the structures become increasingly unstable as x increases in $Li_{2-x}O_2$. The lower plateau at 2.61 V at $x > 1$ in Fig. 8 corresponds to the decomposition potential of LiO_2 in the *$P6_3/mmc$-layered* structure (Fig. 4). This potential is well below the typical charging voltage, and hence, no long-lived LiO_2 is expected in the charge process, which is confirmed by in-situ SERS characterization.[23]

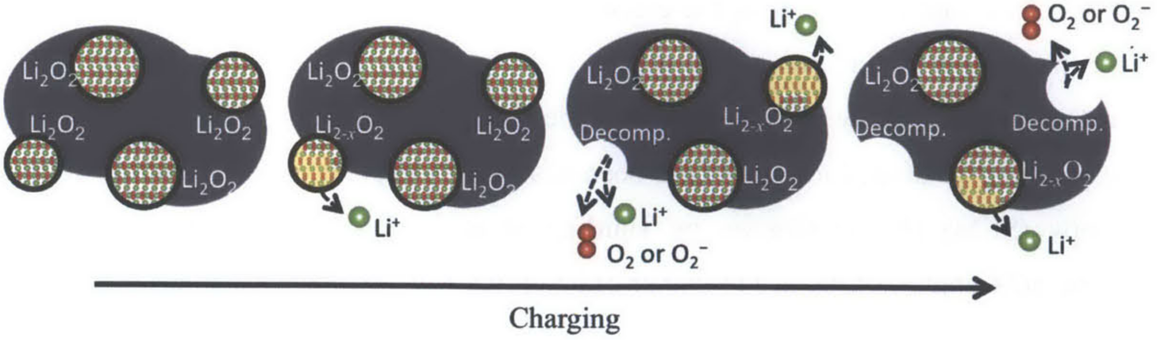

Figure 10. A facile off-stoichiometric mechanism of charging in Li-O$_2$ batteries. Due to the non-monotonic voltage profile upon charging (Fig. 8), only a few Li$_2$O$_2$ particles are involved in the topotactic delithiation at any given time. Reprinted with permission from Kang, S.; Mo, Y.; Ong, S. P.; Ceder, G. *Chemistry of Materials* **2013,** 25 (16), 3328-3336. Copyright 2014 American Chemical Society.

Notably, our predicted potential for LiO$_2$ is very close to the typical *discharge* potentials observed in Li-air cells,[26, 60] which is consistent with the first step in *discharge* being the formation of the metastable superoxide. However, in charge, either decomposition before $x = 1$ or topotactic delithiation of Li$_2$O$_2$ to LiO$_2$ occurs, with the LiO$_2$ immediately decomposing. In either case, the superoxide will not be observed.

When the charging mechanism occurs along the topotactic delithiation pathway to Li$_{2-x}$O$_2$, near $x = 1$, LiO$_2$ may simply dissolve into the electrolyte,[86] and the last oxidation step of O_2^- to O$_2$ may occur on the surfaces of the electrode pores or at catalytic additives present.[65, 67, 71, 72, 103] If the material disintegrates at before reaching LiO$_2$ ($x < 1$), then, some amount of disproportionation will occur from Li$_{2-x}$O$_2$ into $(1-x)$ Li$_2$O$_2$ + x LiO$_2$, which, with dissolution of the superoxide, would lead to $(1-x)$ Li$_2$O$_2$ + x [Li$^+$] + x [O_2^-].

It is important to stress that our results provide a mechanism by which Li$_2$O$_2$ particles can lose Li$^+$ upon charging; however, our results do not argue that the electrode as a whole passes homogenously through these off-stoichiometric states. Two factors will promote inhomogeneous charging. The shape of the predicted voltage profile along the non-equilibrium path drives localization of current in the electrode as it leads to accelerated charging of the particles that – due to their size or connectivity and position in the electrode – proceed first in delithiation. A secondary effect is that the particles that charge first will locally inject Li^+ and O_2 species in the electrolyte at a high rate when they decompose and decrease the local potential, preventing nearby Li_2O_2 particles from reacting until the excess Li^+ and O_2 are removed by diffusion through the electrode porosity. This local particle-by-particle charging illustrated in Fig. 10 has been observed in experiments.[67] Scanning electron microscopy (SEM) characterization by Harding *et al.*[67] demonstrated that the electrode charged by 50% contains a reduced number of Li_2O_2 particles, while the size of the left Li_2O_2 particles remains the same as before charging. Neither the direct surface decomposition[51, 54] nor the stepped surface-facilitated mechanism[54, 55, 74] can explain this inhomogeneous decomposition mechanism at the beginning of charge in Li-O_2 batteries. Our proposed mechanism also agrees with the experimental and computational observation of the existence of LiO_2-like species.[78, 104]. Yang *et al.*[78] attributed the observed Raman spectrum peak at ~1125 cm^{-1} to the LiO_2-like species on the surface of small $(Li_2O_2)_n$ clusters ($n = 3$–4, 16). However, it is unlikely for surfaces or small clusters to account for ~30–50% of the charging capacity, given that Li_2O_2 particle sizes are only tens to hundreds of nanometers. However, the topotactic delithiation may contribute to a significant amount of charging capacity, and the topotactically delithiated *$P6_3$/mmc-layered* LiO_2 phase yields an O_2^- vibrational frequency that is consistent with the experimental Raman spectra. This vibrational peak of superoxides in the Raman spectra has been attributed to the initial 40% of charging capacity at the low charging voltage plateau ~3.2–3.5 V.

The localization of the instantaneous reaction may make it difficult to observe the off-stoichiometric states during charge as these states immediately proceed to charge completely under constant applied voltage according to Fig. 8. Nonetheless, as these states constitute the path by which particles charge, they are important in understanding the overpotential and kinetics of Li-air batteries. This inhomogeneous reaction is also important in understanding why O_2 evolution starts at the same time as the onset of the charging current, as documented in Refs. 16 and 26. We predict that at any given time, only a small fraction of the particles are participating in the charging process. Some of these particles may be in the initial delithiation process, while others, which reached the delithiation step earlier due to their size or position in the electrode, are in the process of fully decomposing and releasing O_2. Hence, while for a single particle, the Li^+ extraction and O_2 evolution do not coincide according to

Eq. (3-1), on average, at the electrode level, they will evolve in a ratio of two to one, as is observed in experiments.[16, 26]

Our proposed reaction path successfully reveals the origin of the low charging voltage plateau at 3.2−3.3 V at the initial stage of charging. This reaction path is also consistent with the relatively higher rate and other observed phenomena in the corresponding experiments. Our proposed reaction path only accounts for a part of the charging process at the low overpotential. Further studies are required to understand whether the increase in charging voltage after the initial 30−50% charge is due to intrinsic features of Li_2O_2 decomposition or due to electrode design issues. In that context, it is important to understand that according to our proposed mechanism, the smaller and better connected particles (electronically and ionically) will fully charge first, leaving the larger and poorly connected particles uncharged until the later part of the charge is reached, as depicted in Fig. 10. Hence, a strong degradation of the kinetics toward the later part of charge is expected from our mechanistic model.

The consequences of our findings are significant. At the single particle level, we predict a facile path to recharge a Li-air battery once some overpotential is applied. If this is the only path with reasonable reaction kinetics, then, this overpotential sets a minimum bound on the charge potential of a Li-air system. However, given the low formation energy of $Li_{2-x}O_2$ phases and good electronic and ionic conductivity in $Li_{2-x}O_2$, one can reasonably infer that at this overpotential, the local rate of Li removal from a Li_2O_2 particle is fast, suggesting the exciting possibility to create fast charging Li-air systems once the transport issues at the electrode and electrolyte level, rather than at the particle level, are resolved. We believe that resolving the current density limitations in Li-air systems is one of the significant obstacles toward technological application and that our findings indicate that there are no obstacles to this achievement at the Li_2O_2 particle level.

5.4. Remaining questions

We have investigated the first half of the charging that involves attackable superoxide ions. In the study of the second phase of charging mechanism, the energetics of solvation of LiO_2 and/or solid-state delithiation of $Li_{2-x}O_2$, where $x > 1$, should be investigated. As we discussed in Chapter 5.3, the solvation mechanism is more likely because LiO_2 is soluble in aprotic solvents. The complexity arises from the concurrent reactions of dissolution and nucleophilic attack of LiO_2 (or O_2^-). Furthermore, the lack of experimental data that are not contaminated by electrolyte or air electrode decomposition makes the problem more complicated.

In addition, in terms of engineering aspects, previous studies on catalysts, air electrodes, and redox mediators did not consider the reactions involving LiO_2 or O_2^-, such as the formation of LiO_2-like surface units and their dissolution. Similar to studies on new electrolytes to replace carbonates while accounting for attackable O_2^- ions, a new research direction to design catalysts, air electrodes, and redox mediators must be considered to improve the reversibility and power density of Li-air batteries.

PART THREE[**]

Chapter 6. Literature Review: Puzzles in Discharge Products of Na-Air Batteries

Notwithstanding the promising performance of Na–O_2 batteries as described in Chapter 1, there are remaining questions in Na–O_2 electrochemistry – some studies[9, 10] reported NaO_2 as the main discharge product, while others[32-35, 105-107] reported Na_2O_2. When Na_2O_2 is formed as a discharge product, the cells exhibit poor reversibility (< 10 cycles) and high overpotentials (from 0.3 V to higher than 1.0 V).[33-35, 105-107] However, the charge and discharge overpotentials are reduced to less than 200 mV when NaO_2 forms,[9, 10] offering prospects for highly reversible Na–O_2 batteries. Currently, there is no understanding of how reaction conditions control the formation of either peroxide or superoxide.

In addition, it appears that the thermodynamic stability and formation of the superoxide are significant in controlling the performance of different metal-air battery systems. In Li–O_2 batteries, the dominant discharge product is Li_2O_2, which is difficult to recharge. The overpotential needed to decompose this phase is as high as 1 V, which causes electrolyte decomposition and the formation of byproducts.[5, 7] In addition, it is possible that unstable LiO_2 is an intermediate state,[56] which creates free superoxide species that attack the electrolyte and carbon support. NaO_2 and KO_2 are significantly more stable as superoxides. As like in a Na–O_2 battery, which forms NaO_2 as a discharge product with less than 200 mV of overpotentials, in the K–O_2 system, KO_2 is even more stable relative to K_2O_2 and K_2O, and the overpotentials needed to charge it are correspondingly lower at 50 mV.[6] The fact that the formation of the superoxide is a one-electron reduction/oxidation process, as opposed to the two-electron process associated with peroxide, may lead to more facile kinetics, less susceptible to side reactions, and may account for the better kinetics of superoxide charging.

[**] This part has been accepted to *Nano Letters* for publication.

These observations indicate that the stability of the superoxide is possibly a key parameter to design viable metal-air batteries. Hence, unraveling the puzzle in Na–O_2 batteries, i.e., determining the conditions that govern the nature of the Na–O discharge compound, is essential to understand and improve the performance of Na–O_2 batteries.

In Part Three, we investigate the thermodynamic stability of Na–O compounds as a function of temperature, O_2 partial pressure, and particle size using first-principles calculations. The energy of bulk Na–O compounds is calculated and combined with environmentally equilibrated surface energies, and phase diagrams as a function of particle size and O_2 partial pressure are constructed. Using this thermodynamic information in a nucleation model, we find that the superoxide NaO_2 is the preferred nanoparticle product at high P_{O_2} or at small discharge overpotential, indicating that it is the most likely phase to nucleate first, even when Na_2O_2 is the thermodynamically preferred bulk state. Hence, our results demonstrate that understanding the particle-size dependence of phase stability is crucial for understanding nucleation.

Chapter 7. Phase Diagram of Bulk Sodium Oxides from First-Principles Calculations

7.1. Methods

We considered all Na–O compounds and polymorphs reported by Wriedt:[11] Na_2O, Na_2O_2, NaO_2, and NaO_3.[108, 109] The structures of these compounds are displayed in Fig. 11. The stable structure of NaO_2 below 196 K has the Pnnm space group, which is shown in Fig. 11(d). Between 196 K and 223 K, the Pa$\bar{3}$ structure is the stable form of NaO_2. This structure is derived from the NaCl rocksalt structure with O_2 dimers centered on the "Cl" lattice positions and aligned along the <111> directions, as illustrated in Fig. 11(e). Above 223 K, O_2 bonds freely rotate, leading to the Fm$\bar{3}$m space group, a disordered form of the Pa$\bar{3}$ structure.[108, 109] More information reported in experiments on these compounds can be found in Table 3. Because the $P6_3/mmc$ structure of Na metal is only stable below 36 K and the Im$\bar{3}$m structure is stable between 36 K and 370.98 K, we only considered the Im$\bar{3}$m structure for Na metal.

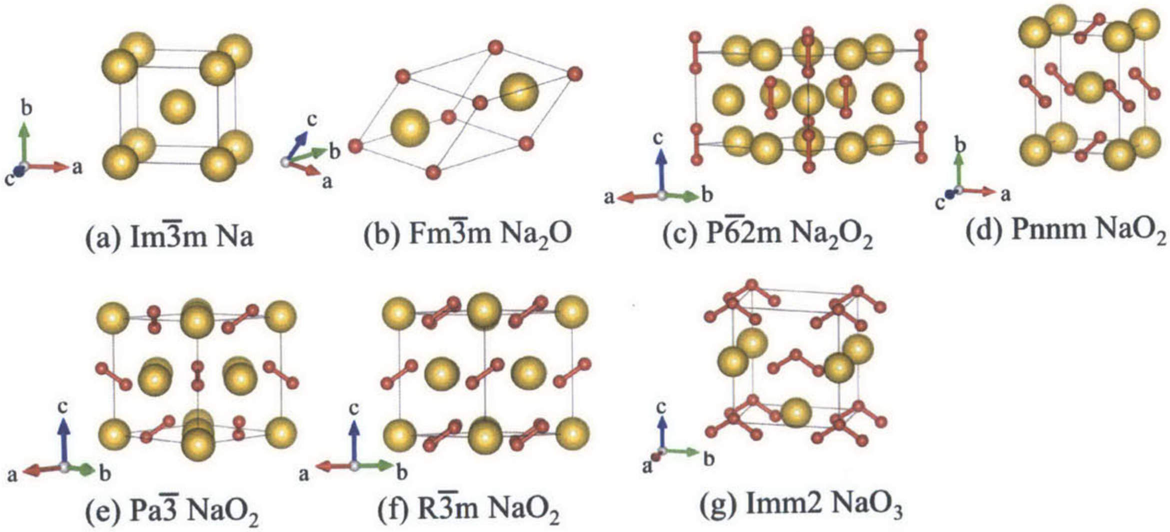

(a) Im$\bar{3}$m Na (b) Fm$\bar{3}$m Na_2O (c) P$\bar{6}$2m Na_2O_2 (d) Pnnm NaO_2

(e) Pa$\bar{3}$ NaO_2 (f) R$\bar{3}$m NaO_2 (g) Imm2 NaO_3

Figure 11. The structures of (a) Im$\bar{3}$m Na metal; (b) Fm$\bar{3}$m Na_2O; (c) P$\bar{6}$2m Na_2O_2; NaO_2 polymorphs, (d) Pnnm, (e) Pa$\bar{3}$ (ordered form of Fm$\bar{3}$m), and (f) Rm$\bar{3}$; and (g) Imm2 NaO_3. The yellow spheres represent Na ions, and the red spheres represent O ions with their bonds marked as red bars. Reprinted with permission from Kang, S.; Mo, Y.; Ong, S. P.; Ceder, G. *Nano Letters* **2014,** 14 (2), 1016-1020. Copyright 2014 American Chemical Society.

Table 3. Structure and phase transition information about the Na and Na–O compounds considered in this study.[58] Reprinted with permission from Kang, S.; Mo, Y.; Ong, S. P.; Ceder, G. *Nano Letters* **2014,** 14 (2), 1016-1020. Copyright 2014 American Chemical Society.

Compound	Structure	Note
Na	$P6_3/mmc$	Phase transition from $P6_3/mmc$ to $Im\bar{3}m$ at ~ 36 K
	$Im\bar{3}m$	Melting at 370.98 K
Na_2O	$Fm\bar{3}m$	Stable up to 1407 K
Na_2O_2	$P\bar{6}2m$	Phase transition to a different structure at ~785 K
NaO_2	Pnnm	Magnetic transition at ~ 43 K, phase transition from Pnnm to ordered $Pa\bar{3}$ at 196 K
	$Pa\bar{3}$	O_2 bonds aligned to <111> directions, order-disorder transition at 223 K
	$Fm\bar{3}m$	Disordered arrangements of O_2 bonds
NaO_3	Imm2 (I4/mmm)	Wriedt[11] reported on I4/mmm structure, but all compounds reported in ICSD (ICSD # 85587, 180566, 411168) are in the Im2m structure.

We performed total energy calculations using the VASP code package[45] within GGA. We calculated the ground state energies of O_2 gas and the Na–O compounds in Fig. 11. For Na, the $2p$ and $3s$ states were treated as valence states using a Na_pv ($2p^6$ $3s^1$) pseudopotential. The O ($2s^2$ $2p^4$) pseudopotential was used for O. The energy cutoff for plane-waves was set to 520 eV, and the energies and forces were converged within 10^{-6} eV and 10^{-3} eV/Å per formula unit, respectively. The spacing of the Γ-centered *k*-point meshes was set to less than 0.05 $Å^{-1}$. To correct the DFT errors for different oxygen environments, the oxidation energy correction reported in Chapter 2.2 was applied.

7.1.1. Computational details for phonon calculations

To assess the vibrational entropy in the solid states, phonon calculations were performed using the small displacement method within the harmonic approximation. The force constant matrix was constructed using the PHON software[96] based on the Hellman-Feynman forces calculated in GGA when symmetrically distinct atomic displacements were imposed in the structures. The supercell dimensions used for phonon computation were as follows: 5 × 5 × 5 for $\mathrm{Im}\bar{3}\mathrm{m}$ Na, 4 × 4 × 4 for $\mathrm{Fm}\bar{3}\mathrm{m}$ Na_2O, 2 × 2 × 3 for $\mathrm{P}\bar{6}2\mathrm{m}$ Na_2O_2, 3 × 3 × 3 for Pnnm NaO_2, 3 × 3 × 3 for $\mathrm{R}\bar{3}\mathrm{m}$ NaO_2 (to represent $\mathrm{Fm}\bar{3}\mathrm{m}$ NaO_2), and 3 × 3 × 3 for Imm2 NaO_3. For each compound, 0.04 Å of symmetrically distinct atomic displacements were introduced, and the Hellman-Feynman forces were obtained in GGA-DFT.

The Gibbs free energy of solids is approximated by the Helmholtz free energy as pressure effects on solids can be neglected:

$$\begin{aligned} G(T,P) &\cong F(T,V^0) \\ &= E^{\mathrm{total}}(V^0) + \Delta F^{\mathrm{harm}}(T,V^0) \\ &= E^{\mathrm{total}}(V^0) + \Delta E^{\mathrm{harm}}(T,V^0) - TS^{\mathrm{harm}}(T,V^0), \end{aligned} \qquad \text{Eq. (7-1)}$$

where V^0 is the optimized volume of the solid within DFT, E^{total} is the total energy calculated in DFT, and ΔF^{harm} is the Helmholtz free energy change due to vibrations in the harmonic approximation, which is decomposed into contributions from the internal energy change ΔE^{harm} and entropy S^{harm}.

The calculated phonon spectrum of $\mathrm{Pa}\bar{3}$ NaO_2 exhibited imaginary phonon frequencies, indicating that the structure is dynamically unstable (Figs. 12(g) and 12(h)). Instead we calculated the phonons for the $\mathrm{R}\bar{3}\mathrm{m}$ NaO_2 structure, where all the O_2 bonds are aligned in one [111] direction (Fig. 11(f)). To represent the rotation of O_2 molecules in $\mathrm{Fm}\bar{3}\mathrm{m}$ NaO_2 (disordered form of the $\mathrm{Pa}\bar{3}$ structure), we started from the phonon energy and entropy of $\mathrm{R}\bar{3}\mathrm{m}$ NaO_2 and added a fraction of the energy and entropy contributions of a rigid rotor:[110]

$$E^{\mathrm{rotor}} \approx k_B T \left\{ 1 - \frac{T_{\mathrm{rot}}}{3T} - \frac{1}{45}\left(\frac{T_{\mathrm{rot}}}{T}\right)^2 \right\}$$

and $$S^{\text{rotor}} \approx k_B \left\{ 1 - \ln\left(\frac{2T_{\text{rot}}}{T}\right) - \frac{1}{90}\left(\frac{T_{\text{rot}}}{T}\right)^2 \right\} \qquad \text{Eq. (7-2)}$$

per O_2, when $T > 5\,T_{\text{rot}}$. Here, $\boldsymbol{k_B}$ is the Boltzmann constant, and $T_{\text{rot}} = 2.08$ K, the characteristic rotational temperature of O_2 gas. The fraction was set to 80% to reproduce the phase transition temperature between the NaO_2 polymorphs, and the equilibrium temperature between Na_2O_2 and NaO_2 at $P_{O_2} = 1$ atm (see Chapter 7.2.2). We also observed imaginary frequencies in the phonon spectrum of NaO_3 and will not consider this phase further in this thesis.

7.1.2. Formation free energy formalism as a function of T and P_{O_2}

The formation free energies ΔG_{form} of sodium oxides were calculated as a function of T and P_{O_2} by combining the phonon energy of solids, the (T, P_{O_2})-dependent chemical potential of oxygen, and the oxidation energy correction. The formation enthalpy of Na–O compounds at 300 K can be expressed by combining Eq. (2-1) and the oxidation energy correction term as

$$\Delta H_{\text{form}}(300\text{ K}) = \Delta E_{\text{form}}(0\text{ K}) - \tfrac{y}{2} E_{\text{oxd}}, \qquad \text{Eq. (7-3)}$$

where E_{oxd} is the oxidation correction energy obtained in Chapter 2.2. Referencing the formation enthalpy at 300 K, ΔH_{form} at a given temperature T can be calculated as

$$\begin{aligned}\Delta H_{\text{form}}(T) &= \Delta H_{\text{form}}(300\text{ K}) + \left\{E^{\text{harm}}_{\text{Na}_x\text{O}_y}(T) - xE^{\text{harm}}_{\text{Na}}(T) - \tfrac{y}{2}\Delta H_{\text{O}_2}(T)\right\} \\ &\quad - \left\{E^{\text{harm}}_{\text{Na}_x\text{O}_y}(300\text{ K}) - xE^{\text{harm}}_{\text{Na}}(300\text{ K}) - \tfrac{y}{2}\Delta H_{\text{O}_2}(300\text{ K})\right\} \\ &= \Delta H_{\text{form}}(300\text{ K}) + \Delta\Delta H_{\text{form}}(T) - \Delta\Delta H_{\text{form}}(300\text{ K}) \end{aligned}, \qquad \text{Eq. (7-4)}$$

where E_i^{harm} is the internal energy of solid i contributed from the phonon vibration as in Eq. (7-1), $\Delta H_{\text{O}_2}(T) = \tfrac{7}{2}k_B T$ using the diatomic ideal gas approximation for the enthalpy of O_2 gas, and $\Delta\Delta H_{\text{form}}$ is defined as

$$\Delta\Delta H_{\text{form}}(T) \equiv E^{\text{harm}}_{\text{Na}_x\text{O}_y}(T) - xE^{\text{harm}}_{\text{Na}}(T) - \tfrac{y}{2}\Delta H_{\text{O}_2}(T) \quad . \qquad \text{Eq. (7-5)}$$

In the same manner, the formation free energy of Na–O compounds at 300 K and 1 atm can be expressed as

$$\begin{aligned}
&\Delta G_{\text{form}}(300\text{ K, 1 atm}) \\
&\quad = \Delta H_{\text{form}}(300\text{ K}) - 300\cdot\Delta S_{\text{form}}(300\text{ K, 1 atm}) \\
&\quad = \left\{\Delta E_{\text{form}}(0\text{ K}) + \tfrac{y}{2}E_{\text{oxd}}\right\} \\
&\qquad - 300\cdot\left\{S^{\text{harm}}_{\text{Na}_x\text{O}_y}\left(300\text{ K}, V^0_{\text{Na}_x\text{O}_y}\right) - xS^{\text{harm}}_{\text{Na}}\left(300\text{ K}, V^0_{\text{Na}}\right) - \tfrac{y}{2}S_{\text{O}_2}\left(300\text{ K, 1 atm}\right)\right\}
\end{aligned} \quad ,\text{Eq. (7-6)}$$

and can be generalized to any given temperature and O2 partial pressure as

$$\begin{aligned}
\Delta G_{\text{form}}(T, P_{\text{O}_2}) &= \Delta H_{\text{form}}(T) - T\Delta S_{\text{form}}\left(T, P_{\text{O}_2}\right) \\
&\cong \Delta H_{\text{form}}(300\text{ K}) + \Delta\Delta H_{\text{form}}(T) - \Delta\Delta H_{\text{form}}(300\text{ K}) \\
&\quad - T\left\{S^{\text{harm}}_{\text{Na}_x\text{O}_y}(T, V^0_{\text{Na}_x\text{O}_y}) - xS^{\text{harm}}_{\text{Na}}(T, V^0_{\text{Na}}) - \tfrac{y}{2}S_{\text{O}_2}\left(T, P_{\text{O}_2}\right)\right\}
\end{aligned} \quad . \text{ Eq. (7-7)}$$

Note that the entropy of O2 gas in Eqs. (7-6) and (7-7) is approximated as the combination of experimental entropy[58] and pressure-dependent ideal gas behavior for O2 gas:

$$S_{\text{O}_2}(T, P_{\text{O}_2}) = S^{\text{expt}}_{\text{O}_2}(T) - k_B\log\left(P_{\text{O}_2} / P^{\text{o}}_{\text{O}_2}\right) , \qquad \text{Eq. (7-8)}$$

where $S^{\text{expt}}_{\text{O}_2}$ is the temperature-dependent entropy of O2 gas at 1 atm as obtained from experiments,[58] and the last term is the partial pressure dependence of the entropy of the ideal gas, where $P^{\text{o}}_{\text{O}_2}$ is set to 1 atm. In total, the chemical potential of O2 gas as a function of temperature and O2 partial pressure is obtained as follows:

$$\begin{aligned}
\mu_{\text{O}_2}\left(T, P_{\text{O}_2}\right) &= E^{\text{total}}_{\text{O}_2} + \Delta H_{\text{O}_2}(T) - TS_{\text{O}_2}\left(T, P_{\text{O}_2}\right) \\
&= E^{\text{total}}_{\text{O}_2} + \tfrac{7}{2}k_BT - TS^{\text{expt}}_{\text{O}_2}(T) + k_BT\left(P_{\text{O}_2} / P^{\text{o}}_{\text{O}_2}\right) \cdot
\end{aligned} \qquad \text{Eq. (7-9)}$$

7.2. Results

7.2.1. Calculated phonon spectra of Na–O compounds

The phonon spectra calculated for Na metal and Na–O compounds are displayed in Fig. 12. Due to the presence of imaginary frequencies in Pa$\bar{3}$ NaO$_2$ (ordered form of Fm$\bar{3}$m NaO$_2$) in Figs. 12(g) and 12(h), we have tested different sets of energy and force convergence criteria, kinetic energy cutoff, charge density mixing parameters, and algorithms that can affect the final structure and Hellman-Feynman forces within the small displacement method used. In addition, we have calculated the phonon spectra using the density functional perturbation theory.[111-113] However, none of these attempts were successful in removing the imaginary frequencies. In Figs. 12(g) and 12(h), we display the phonon dispersion and density of states (DOS) of Pa$\bar{3}$ NaO$_2$ calculated using the small displacement method with an energy cutoff of 700 eV and the density functional perturbation theory using VASP, respectively. In both methods, the phonon spectra of Pa$\bar{3}$ NaO$_2$ show imaginary frequencies, indicating that the Pa$\bar{3}$ NaO$_2$ structure is not dynamically stable.

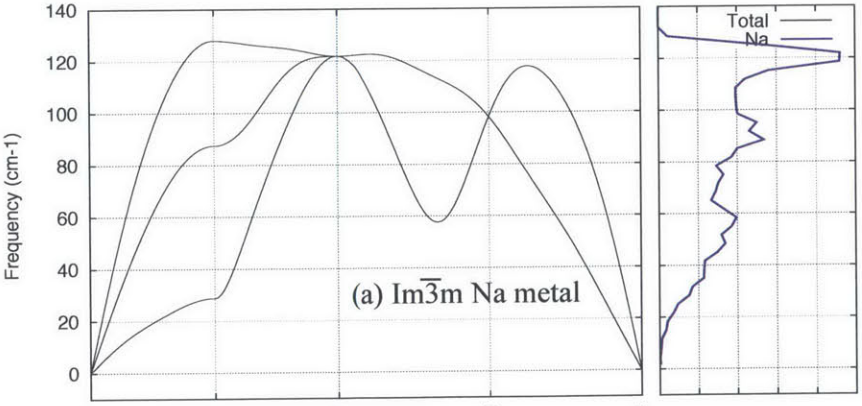

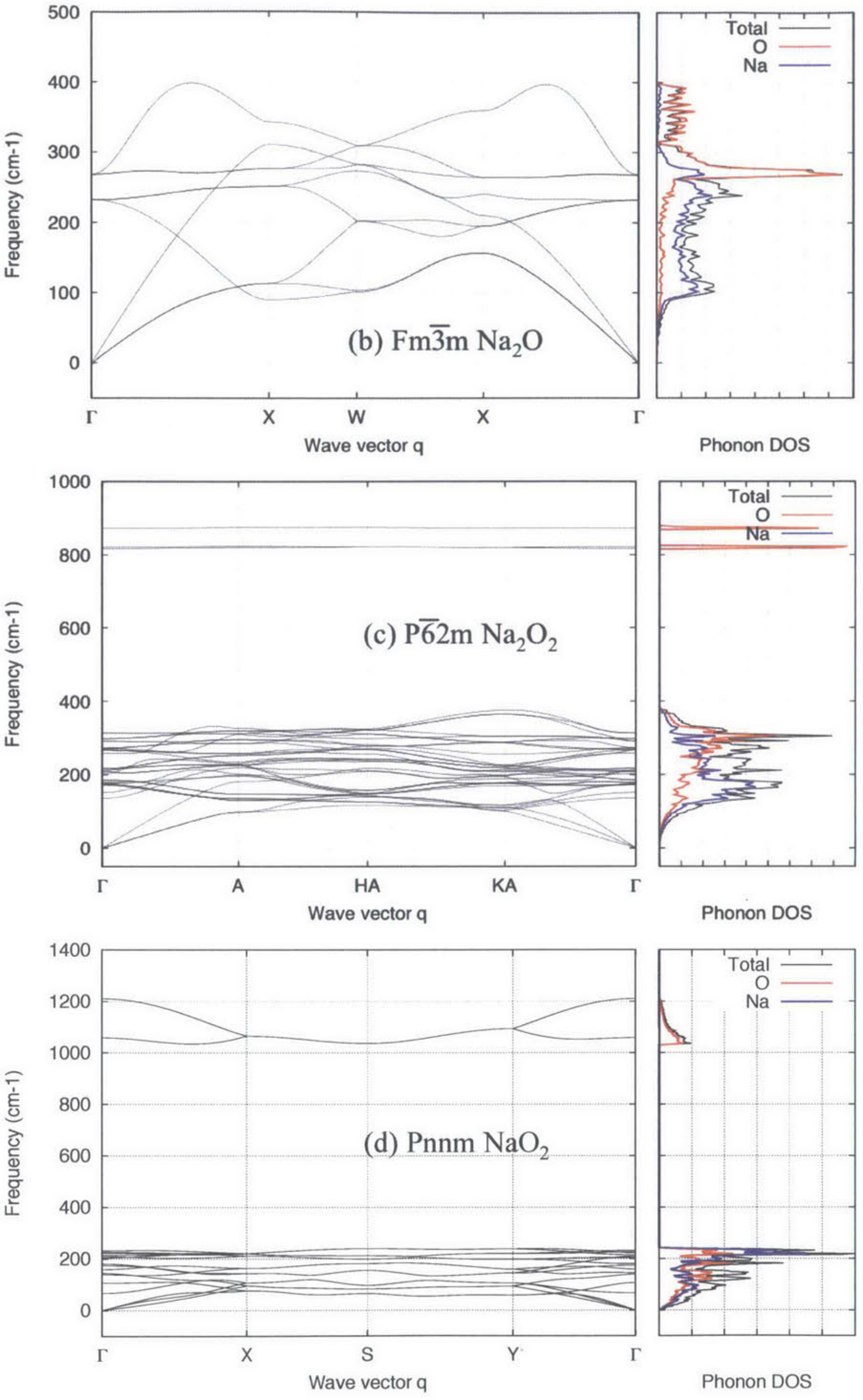
500
400
300
200
100
0
Frequency (cm-1)
(b) Fm$\overline{3}$m Na$_2$O
Γ
X
W
X
Γ
Wave vector q
Total
O
Na
Phonon DOS
1000
800
600
400
200
0
Frequency (cm-1)
(c) P$\overline{6}$2m Na$_2$O$_2$
Γ
A
HA
KA
Γ
Wave vector q
Total
O
Na
Phonon DOS
1400
1200
1000
800
600
400
200
0
Frequency (cm-1)
(d) Pnnm NaO$_2$
Γ
X
S
Y
Γ
Wave vector q
Total
O
Na
Phonon DOS

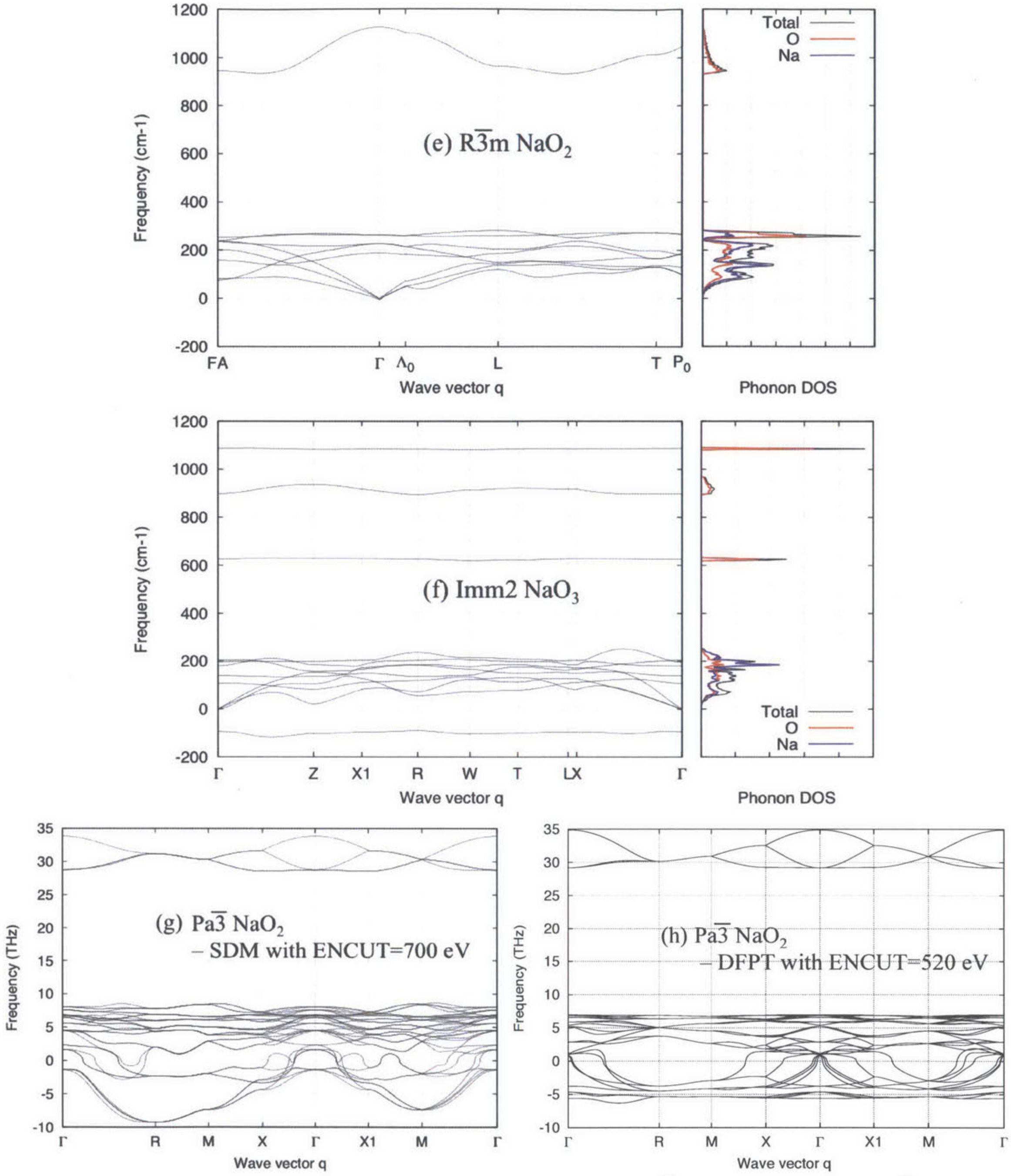

Figure 12. Phonon dispersion and density of states for (a) Im$\overline{3}$m Na metal, (b) Fm$\overline{3}$m Na$_2$O, (c) P$\overline{6}$2 Na$_2$O$_2$, (d) Pnnm NaO$_2$, (e) R$\overline{3}$m NaO$_2$, and (f) Imm2 NaO$_3$. The partial phonon density of states contributed from Na and O are shown in blue and red, respectively. The phonon dispersion of Pa$\overline{3}$ NaO$_2$ calculated using the small displacement method (SDM) with the energy cutoff set to 700 eV and the density functional perturbation theory (DFPT) is displayed in (g) and (h), respectively. Reprinted with permission from Kang, S.; Mo, Y.; Ong, S. P.; Ceder, G. *Nano Letters* **2014,** 14 (2), 1016-1020. Copyright 2014 American Chemical Society.

7.2.2. Temperature dependent stability of bulk Na–O compounds

The formation free energies of Na_2O, Na_2O_2, and NaO_2 in eV/Na versus temperature are plotted in Fig. 12. In Fig. 12, the solid blue, red, and green lines (circles) represent the calculated (experimental) ΔG_{form} of Na_2O, Na_2O_2, and NaO_2, respectively. The green line is obtained as the lowest energy envelope of the two NaO_2 polymorphs, represented as the dashed gray line for Pnnm NaO_2 and the dash-dot gray line for $Fm\bar{3}m$ NaO_2. The energy is given per Na in the formula unit to represent the system open to oxygen. Given that the experimental ΔG_{form} values at 1 atm are available,[58] the temperature dependency of ΔG_{form} can be used to validate our computations. The formation free energies of Na–O compounds at 0 and 300 K are compared with experimental values in Table 4.

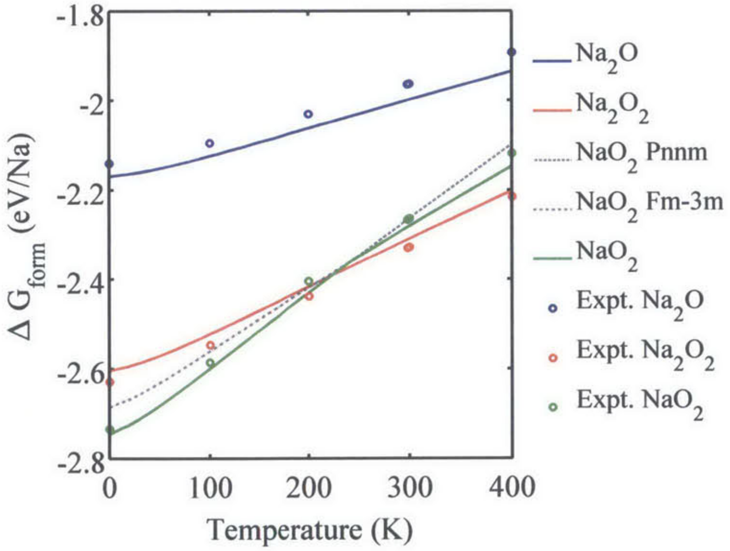

Figure 13. The formation free energies of $Fm\bar{3}m$ Na_2O (blue), $P\bar{6}2m$ Na_2O_2 (red), Pnnm NaO_2 (dashed gray line), $Fm\bar{3}m$ NaO_2 (dash-dot gray line), and the lowest energy envelope for NaO_2 (green) as a function of temperature. The calculated data are plotted in lines, and the experimental data are marked as circles. Reprinted with permission from Kang, S.; Mo, Y.; Ong, S. P.; Ceder, G. *Nano Letters* **2014,** 14 (2), 1016-1020. Copyright 2014 American Chemical Society.

Table 4. The calculated formation free energies of Na–O compounds (experimental values[58] in parentheses) at 0 K and 300 K at 1 atm. The stable phases at each temperature are marked in bold. Reprinted with permission from Kang, S.; Mo, Y.; Ong, S. P.; Ceder, G. *Nano Letters* **2014,** 14 (2), 1016-1020. Copyright 2014 American Chemical Society.

Compounds	ΔG_{form} (eV/Na)	
	0 K	300 K
Na_2O	**−2.17 (−2.14)**	**−2.00 (−1.96)**
Na_2O_2	**−2.60 (−2.63)**	**−2.31 (−2.33)**
Pnnm NaO_2	**−2.75 (−2.74)**	−2.26 (-)
$Fm\bar{3}m$ NaO_2	−2.69 (-)	**−2.28 (−2.26)**

As observed in Fig. 13, the temperature-dependent ΔG_{form} values of the Na–O compounds are in good agreement with the experimental values. The absolute errors at any given temperature are less than 40 meV/Na. Furthermore, the absolute errors for Na_2O_2 and NaO_2, which are of interest as discharge products in Na–O_2 batteries, are less than 30 meV/Na. As these errors are almost constant with respect to temperature (Fig. 13), the primary source of errors is possibly ΔH_{form}, and we can presumably conclude that the source of errors is the oxidation energy correction that is obtained from the fitting of various metal oxides, peroxides, and superoxides as described in Chapter 2.2. Although Na_2O_2 is slightly under-stabilized compared with NaO_2, our computational results successfully predict the trends in ΔG_{form} with respect to temperature and the relative stability of Na–O compounds. Thus, we continue our study to investigate the phase stability of Na–O compounds as a function of O_2 partial pressure, as the O_2 partial pressure is a more important parameter that varies during the charge and discharge of Na–O_2 batteries.

Adding the full rotor energy and entropy contribution to the energy of $Fm\bar{3}m$ overestimates the stability of this phase, as some of this excitation is also counted in the phonon spectrum of the structure. We find that reducing the rotor contribution to 80% best reproduces the transition temperatures between Na_2O_2 and NaO_2 and between Pnnm NaO_2 and $Fm\bar{3}m$ NaO_2 polymorphs. With this approximation, the transition temperature from Pnnm NaO_2 to $Fm\bar{3}m$ NaO_2 is between 230 and 240 K in our calculations, which is in fair agreement with the experimental transition temperatures of 196 K from Pnnm to ordered $Pa\bar{3}$ and 223 K from ordered $Pa\bar{3}$ to $Fm\bar{3}m$.[108, 109] In addition, the equilibrium temperature between NaO_2 and Na_2O_2 is calculated to be 210–220 K, while being between 100 K and 200 K in experiments.[11] To the best of our knowledge, the exact temperature has not been reported.

7.2.3. Phase diagram of bulk Na–O compounds as a function of T and P_{O_2}

Fig. 14 presents the equilibrium T–P_{O_2} phase diagram of Na–O compounds based on Eq. (7-7). The phase diagram reveals that Na_2O_2 is the thermodynamically favored phase under standard conditions ($P_{O_2} = 1$ atm and $T = 300$ K) and under high temperature or low oxygen pressure. At 300 K, the superoxide NaO_2 in the $Fm\bar{3}m$ structure becomes stabilized at a P_{O_2} higher than 8.5 atm, which is much higher than the typical operating conditions of Na–O_2 batteries. Therefore, Na_2O_2 has been observed to be the dominant discharge product in most experiments.[33, 35, 105-107] Note that Na_2O is not stable in the T and P_{O_2} range considered, which is consistent with its high experimentally measured formation energy when expressed per Na atom, representing "open O_2" conditions.

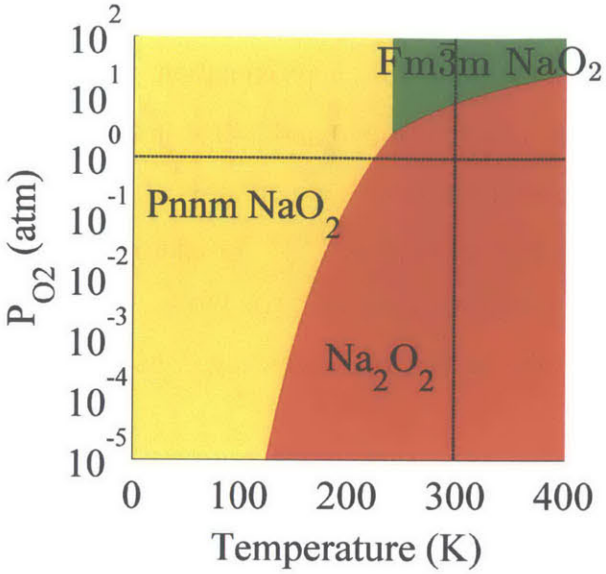

Figure 14. The phase diagram of bulk Na–O compounds as a function of temperature and O_2 partial pressure. The red, yellow, and green domains represent the regions where Na_2O_2, Pnnm NaO_2, and Fm $\bar{3}$ m NaO_2 are stable, respectively. The Pnnm NaO_2 structure transforms to Fm $\bar{3}$ m NaO_2 at 230–240 K when P_{O_2} = 1 atm, and Na_2O_2 is in equilibrium with Fm $\bar{3}$ m NaO_2 at 8.5 atm when T = 300 K. The horizontal dashed line denotes P_{O_2} = 1 atm, and the vertical dashed line denotes T = 300 K. Reprinted with permission from Kang, S.; Mo, Y.; Ong, S. P.; Ceder, G. *Nano Letters* **2014,** 14 (2), 1016-1020. Copyright 2014 American Chemical Society.

Chapter 8. Calculations of Surface Structure and Energies of Na_2O_2 and NaO_2

To understand the relative stability of Na_2O_2 and NaO_2 at the nanoscale, where these oxides nucleate, we expanded our study to include their surface energies. We considered the low-index surfaces of Na_2O_2 and $Fm\overline{3}m$ (disordered $Pa\overline{3}$) NaO_2 as they are the competing compounds near room temperature. As $Fm\overline{3}m$ NaO_2 has the O_2 dimer orientations disordered, we approximated its surface energies using those of ordered $Pa\overline{3}$ NaO_2.

8.1. Methods

We used the surface slab method[114, 115] to calculate the surface energies with vacuum layers thicker than 10 Å and the Na_xO_2 compound layers being ~20 Å thick. The structure optimization and total energy computation were simulated within GGA to DFT using the VASP code package.[45] The computational parameters, such as the pseudopotential, energy and force cutoff, and *k*-points sampling, were identical to those used in Chapter 7.1.

8.1.1. Surface energy formalism

The surface energy at a given temperature and O_2 partial pressure can be calculated as

$$\gamma\left(T,P_{O_2}\right)=\frac{1}{2A}\left\{G_{\text{slab}}\left(T,P_{O_2},N_{\text{Na}},N_{\text{O}}\right)-N_{\text{Na}}\mu_{\text{Na}}\left(T,P_{O_2}\right)-N_{\text{O}}\mu_{\text{O}}\left(T,P_{O_2}\right)\right\}, \quad \text{Eq. (8-1)}$$

where G_{slab} is the Gibbs free energy of the surface slab, N_i is the number of elements i (Na or O) in the surface slab, μ_i is the chemical potential of i, and A is the surface area. Note that the chemical potentials of Na and O are dependent parameters by the formation free energy of bulk Na_xO_2:

$$x\mu_{\text{Na}}^{\text{Na}_x\text{O}_2}\left(T,P_{O_2}\right)+2\mu_{\text{O}}^{\text{Na}_x\text{O}_2}\left(T,P_{O_2}\right)=G_{\text{Na}_x\text{O}_2}\left(T,P_{O_2}\right), \quad \text{Eq. (8-2)}$$

where $\mu_i^{\text{Na}_x\text{O}_2}$ is the chemical potential of element i in Na_xO_2 ($x = 1$ for NaO_2 or $x = 2$ for Na_2O_2), and $G_{\text{Na}_x\text{O}_2}$ is the Gibbs free energy of Na_xO_2 per formula unit. The Gibbs free energy of solid phases can be approximated by their Helmholtz free energy, and combination with Eq. (8-2) transforms Eq. (8-1) into

$$\gamma\left(T,P_{\mathrm{O}_2}\right)=\frac{1}{2A}\Big\{F_{\mathrm{slab}}\left(T,N_{\mathrm{Na}},N_{\mathrm{O}}\right)-\frac{N_{\mathrm{O}}}{2}F_{\mathrm{Na}_x\mathrm{O}_2}(T) \\ -\left(N_{\mathrm{Na}}-\frac{x}{2}N_{\mathrm{O}}\right)\mu_{\mathrm{Na}}^{\mathrm{Na}_x\mathrm{O}_2}\left(T,P_{\mathrm{O}_2}\right)\Big\} \quad , \qquad \text{Eq. (8-3)}$$

where F_{slab} and $F_{\mathrm{Na}_x\mathrm{O}_2}$ are the Helmholtz free energies of the surface slab and bulk $\mathrm{Na}_x\mathrm{O}_2$, respectively.

F_{slab} and $F_{\mathrm{Na}_x\mathrm{O}_2}$ can be calculated by combining the 0 K DFT total energy E^{total}, the temperature-dependent phonon vibrational energy F^{harm} that is approximated in harmonic oscillation, and the oxidation energy correction E_{oxd} as

$$\gamma\left(T,P_{\mathrm{O}_2}\right)\approx\frac{1}{2A}\Big[E_{\mathrm{slab}}^{\mathrm{total}}\left(N_{\mathrm{Na}},N_{\mathrm{O}}\right)+F_{\mathrm{slab}}^{\mathrm{harm}}\left(T,N_{\mathrm{Na}},N_{\mathrm{O}}\right)-E_{\mathrm{oxd,\,slab}} \\ -\frac{N_{\mathrm{O}}}{2}\left\{E_{\mathrm{Na}_x\mathrm{O}_2}^{\mathrm{total}}+F_{\mathrm{Na}_x\mathrm{O}_2}^{\mathrm{harm}}(T)-E_{\mathrm{oxd,\,Na}_x\mathrm{O}_2}\right\}-\left(N_{\mathrm{Na}}-\frac{x}{2}N_{\mathrm{O}}\right)\mu_{\mathrm{Na}}^{\mathrm{Na}_x\mathrm{O}_2}\left(T,P_{\mathrm{O}_2}\right)\Big] . \qquad \text{Eq. (8-4)}$$

We assume that the entropy arising from surface cleavage is negligible and approximate the entropy of non-stoichiometric surface slabs to that of the stoichiometric bulk. This approximation is reasonable given that Reuter and Scheffler[115] observed the contribution of surface entropy to the surface energy being less than 10 meV/Å^2. This approximation cancels out $F_{\mathrm{slab}}^{\mathrm{harm}}$ and $F_{\mathrm{Na}_x\mathrm{O}_2}^{\mathrm{harm}}$, resulting in

$$\gamma\left(T,P_{\mathrm{O}_2}\right)\cong\frac{1}{2A}\Big[E_{\mathrm{slab}}^{\mathrm{total}}\left(N_{\mathrm{Na}},N_{\mathrm{O}}\right)-E_{\mathrm{oxd,\,slab}}-\frac{N_{\mathrm{O}}}{2}\left(E_{\mathrm{Na}_x\mathrm{O}_2}^{\mathrm{total}}-E_{\mathrm{oxd,\,Na}_x\mathrm{O}_2}\right) \\ -\left(N_{\mathrm{Na}}-\frac{x}{2}N_{\mathrm{O}}\right)\mu_{\mathrm{Na}}^{\mathrm{Na}_x\mathrm{O}_2}\left(T,P_{\mathrm{O}_2}\right)\Big] \quad . \qquad \text{Eq. (8-5)}$$

We further assume that the charge density in surface O_2 bonds is localized such that the oxidation correction energy of the surface slab can be approximated by the number of oxides, peroxides, and superoxides multiplied by their corresponding oxidation correction energy:

$$E_{\mathrm{oxd,\,slab}}\cong\sum_{\nu\ \mathrm{in}\ \{\mathrm{O}^{2-},\mathrm{O}_2^{2-},\mathrm{O}_2^{-}\}}N_{\nu}E_{\mathrm{oxd},\,\nu} \quad , \qquad \text{Eq. (8-6)}$$

where N_v is the number of O_2 bonds in the oxidation state v (2 O^{2-}, O_2^{2-}, or O_2^-), and $E_{\mathrm{oxd},v}$ is the oxidation correction energies of the state v that are 1.33, 0.85, and 0.23 eV/O_2 for 2 O^{2-}, O_2^{2-}, and O_2^-, respectively. For instance, a non-stoichiometric {0001} Na_2O_2 surface slab that is composed of 23 Na ions and 26 O ions can be thought of as 10 Na_2O_2 + 3 NaO_2. Therefore, $E_{\mathrm{oxd,\,slab}}$ for this surface slab is calculated as 10 × 0.85 + 3 × 0.23 = 9.19 eV.

This presumption that non-stoichiometric surface slabs are viewed as a combination of aliovalent Na–O compounds based on the charge localization is a crude approximation; however, we verified this approximation by investigating the O_2 bond lengths in the surface slabs. We observed that indeed the surface O_2 bonds change their bond lengths to the appropriate bond length of one of the peroxides (1.55 Å), superoxides (1.35 Å), or O_2 gas (1.23 Å) as the slab stoichiometry changes. In addition, for Na-rich Na_2O_2 surface slabs, the surface O_2 bonds break, and the distance between nearest oxygen ions becomes > 2 Å. Therefore, we believe that our approximation of the oxidation energy correction for the slab (Eq. (8-6)) is relatively valid. Details can be found in Chapter 8.4.

8.1.2. Calculated materials stability as a function of μ_{Na} and μ_{O}

The Na and O chemical potentials where bulk Na_xO_y is stable are limited by adjacent competing Na–O phases and/or Na metal and O_2 gas. For example, the chemical potential of Na in Na_2O has a higher bound at the Na metal limit and a lower bound in equilibrium with Na_2O_2:

$$\mu_{\mathrm{Na}}^{\mathrm{Na_2O}} \le \mu_{\mathrm{Na}}^{\mathrm{Na\ metal}} \qquad \text{Eq. (8-7)}$$

and

$$G_{\mathrm{Na_2O}} - \frac{G_{\mathrm{Na_2O_2}}}{2} \le \mu_{\mathrm{Na}}^{\mathrm{Na_2O}} . \qquad \text{Eq. (8-8)}$$

Using the calculated formation free energies of Na–O compounds, we evaluated their stability as a function of μ_{Na} and μ_{O}. The results with and without the oxidation correction energy E_{oxd} are displayed in Figs. 15(a-1) and 15(a-2) and in Figs. 15(b-1) and 15(b-2) for 0 K and 300 K, respectively. To assess our calculations, we performed the same construction of chemical potential ranges using experimental formation free energies from NIST-

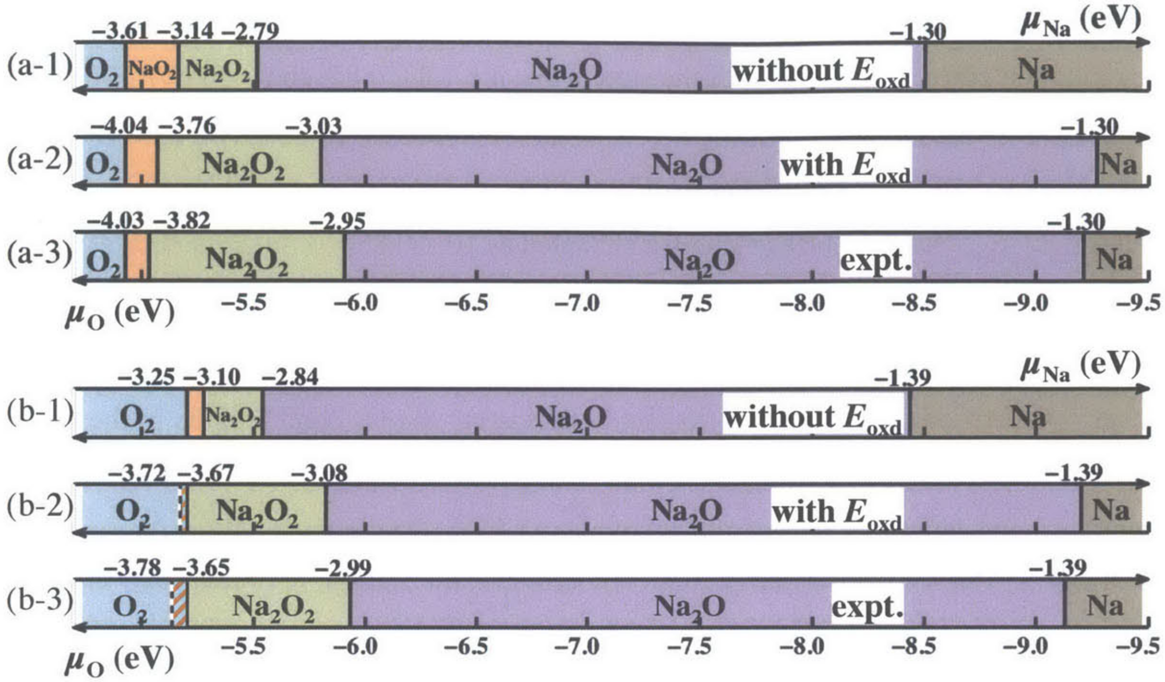

Figure 15. The stability map of Na−O compounds and their chemical potential boundaries at (a) 0 K and (b) 300 K. (a-1) and (b-1) are before applying the E_{oxd}; (a-2) and (b-2) are after applying the E_{oxd}; and (a-3) and (b-3) are based on experimental formation enthalpies.[58] The stability of compounds is mapped on a linear μ_{O} scale, and the corresponding μ_{Na} values at the phase boundaries are labeled above the top axes. Note that the μ_{Na} scale is not linear according to the stoichiometry of the mapped compounds.

JANAF,[58] which are displayed in Figs. 15(a-3) and 15(b-3) for 0 K and 300 K, respectively. Due to the over-stabilization of superoxides and under-stabilization of oxides before correcting with E_{oxd}, the NaO_2 and Na_2O domains were over- and under-estimated, respectively. At both 0 K and 300 K, our E_{oxd} fitting method successfully predicts the stability domains of Na_2O, Na_2O_2, and NaO_2 simultaneously.

The most evident effect of the E_{oxd} correction occurs in the stability prediction for NaO_2 at 300 K, which stays stable before applying E_{oxd} (Fig. 15(b-1)) while becoming metastable after E_{oxd} (Fig. 15(b-2)), which is consistent with experiments (Fig. 15(b-3)). The metastable nature of NaO_2 is denoted by the dashed boxes in Figs. 15(b-2) and 15(b-3), in contact with Na_2O_2 at higher μ_O and with O_2 gas at lower μ_O. The equilibrium between Na_2O_2 and metastable NaO_2 (dashed vertical lines in Figs. 15(b-2) and 15(b-3)) indicates that when oxygen is over-saturated, Na_2O_2 transforms to NaO_2 before passing through the equilibrium decomposition path to 2 Na + O_2. Note that the stable NaO_2 polymorph at 0 K is in the Pnnm space group, while the metastable NaO_2 at 300 K is in the $Fm\bar{3}m$ space group. In Lee *et al.*'s recent computational work,[52] which used μ_O referring to the reaction energy between Li_2O and Li_2O_2, although they predicted stable domains for NaO_2, Na_2O_2, and Na_2O, which are consistent with the experimental data at 0 K, their chemical potential boundary cannot be directly carried to the surface structure computation because particles exist at room temperature in reality, where the stability of NaO_2 shifts from stable to metastable.

Therefore, using the properly designed chemical potential boundaries displayed in Fig. 15(b-2), we evaluated the surface structures of two competing Na–O compounds at room temperature, Na_2O_2 and $Fm\bar{3}m$ NaO_2. For computational purpose, we calculated the surface energies of $Pa\bar{3}$ NaO_2 instead (Fig. 11(e)), which can be obtained when all of the O_2 bonds in $Fm\bar{3}m$ NaO_2 are aligned in the <111> direction. In addition to the correction to the stability of bulk Na–O compounds, we applied the oxidation energy correction to the surface slabs according to their degree of non-stoichiometry based on Eq. (8-6).

8.2. Surface orientations considered for Na_2O_2 and their energies

We considered three low-index surface orientations, $\{0001\}$, $\{1\bar{1}00\}$, and $\{11\bar{2}0\}$, for Na_2O_2. A unit cell of Na_2O_2 consists of two symmetrically distinct Na sites ($z = 0$ and $z = 0.5$), each with multiplicity of three in the unit cell, and two distinct sites for O (see Fig. 11(c). Two identical O atoms form an O_2 bond that straddles the $z = 0$ plane, and the other four O atoms form dimers in the same direction centering at $z = 0.5$. Due to this complexity, Na_2O_2 surfaces have many options for surface cleavage. We did not consider terminations that require the breaking of peroxide bonds as they have been observed to have high surface energies.[51]

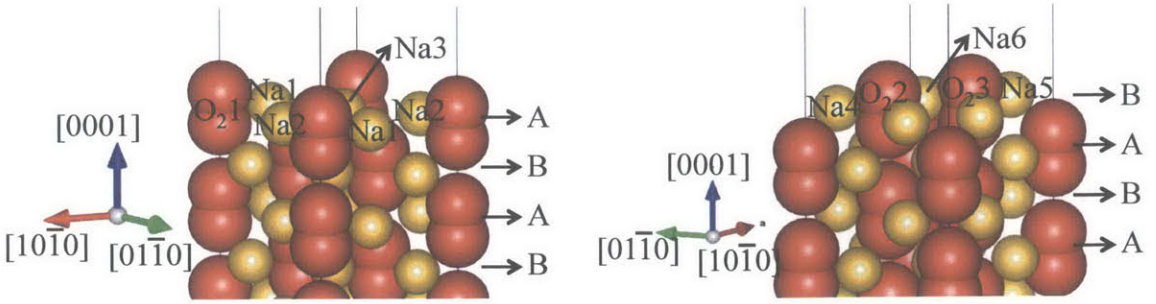

(a) (b)

Figure 16. The surface unit cell of a Na_2O_2 {0001} facet terminated at the (a) A layer and (b) B layer. The yellow spheres represent Na ions, and the red spheres represent O ions. The surface ions that are used to define the surface terminations are labeled in the figure.

8.2.1. Na_2O_2 {0001} surfaces

Along the {0001} orientation, Na_2O_2 is composed of alternate stacking of two different layers, labeled as A and B in Figs. 16(a) and 16(b). We considered 5 terminations for the A layer, and 11 terminations for the B layer. These terminations are denoted by the layer index (A or B) followed by the atoms remaining on the surface, for example, "(A) Na1-Na2-Na3-$O_2$1." The calculated surface energies are listed in Table A 1 in Chapter 8.4. APPENDIX. From the Na_2O limit to the O_2 gas limit, the most reducing and oxidizing boundaries for Na_2O_2 at room temperature, respectively, the (B) Na4-Na5-Na6-$O_2$2-$O_2$3 termination shown in Fig. 16(b) is the most stable termination.

8.2.2. Na_2O_2 $\{1\bar{1}00\}$ surfaces

Along the $\{1\bar{1}00\}$ orientation, Na_2O_2 consists of alternate stacking of three different layers, labeled as A, B, and B′ in Figs. 17(a–c), respectively. The B and B′ layers are identical except that underneath the layer, either B or A is present, respectively. We considered 5 terminations for the A layer, 6 terminations for the B layer, and 6 terminations for the B′ layer. The labeling of terminations follows the notation used for the {0001} surfaces. The calculated surface energies are listed in Table A 1 in Chapter 8.4. APPENDIX. At 300 K after E_{oxd} correction, the lowest surface energy termination for the $\{1\bar{1}00\}$

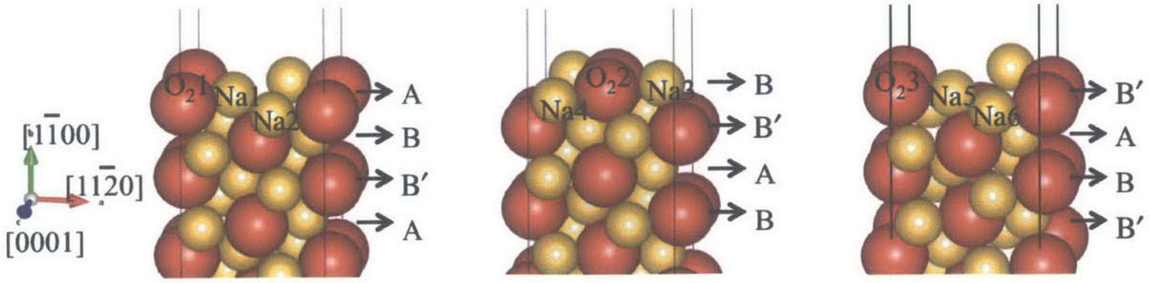

(a) (b) (c)

Figure 17. The surface unit cell of Na_2O_2 $\{1\bar{1}00\}$ terminated at the (a) A layer, (b) B layer, and (c) B′ layer. The yellow spheres represent Na ions, and the red spheres represent O ions. The surface ions that are used to define the surface terminations are labeled in the figure.

orientation evolves from O-rich (B) Na4-$O_2$2 to stoichiometric (A) Na1-Na2-$O_2$1 as the chemical potential moves from oxidizing to reducing limits (from the O_2 gas limit to the Na_2O limit).

8.2.3. Na_2O_2 $\{11\bar{2}0\}$ surfaces

In the $\{11\bar{2}0\}$ Na_2O_2 orientation, the crystal consists of alternating stacking of three different layers, labeled as A, B, and C in Figs. 18(a–c). The A layer consists only of O_2 bonds, while the B and C layers contain only Na ions. We considered 5 terminations for the

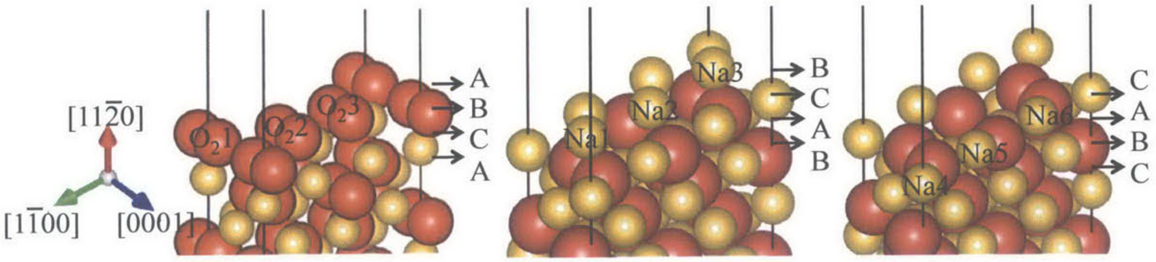

(a) (b) (c)

Figure 18. The surface unit cell of Na_2O_2 $\{11\bar{2}0\}$ terminated at the (a) A layer, (b) B layer, and (c) C layer. The yellow spheres represent Na ions, and the red spheres represent O ions. The surface ions that are used to define the surface terminations are labeled in the figure.

A layer, 3 terminations for the B layer, and 3 terminations for the C layer. The terminations and their energies are listed in Table A 1 in Chapter 8.4. APPENDIX. The lowest energy terminations at room temperature are O-rich (A) O_21-O_22-O_23 and stoichiometric (C) Na4-Na5-Na6 at the most oxidizing and reducing limits, respectively.

8.2.4. The lowest surface energies and Wulff shapes of Na_2O_2 as a function of μ_O

The surface energies of the most stable terminations of Na_2O_2 as a function of μ_O are plotted in Fig. 19(a). The surface energies were calculated at the standard state condition ($T = 300$ K and $P_{O_2} = 1$ atm) using Eq. (8-5), and the range of μ_O where Na_2O_2 is stable (from −5.82 to −5.20 eV) is marked using a yellow box. The energies of O-rich surface slabs decrease with increasing μ_O, and thus, at the most oxidizing limit of Na_2O_2, where $\mu_O = -5.20$ eV in equilibrium with O_2 gas, the lowest energy terminations of all of the surface orientations, {0001}, $\{1\bar{1}00\}$, and $\{11\bar{2}0\}$, are O-rich. However, as μ_O decreases,

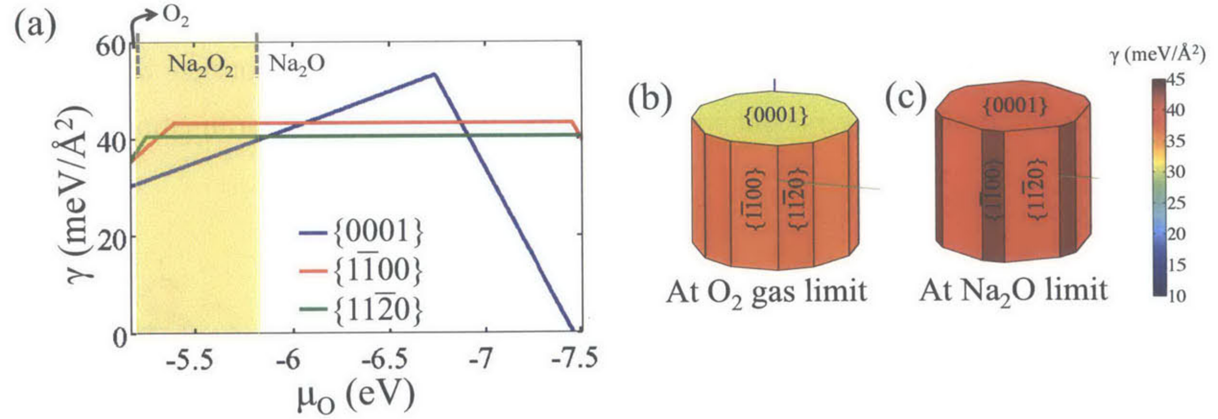

Figure 19. (a) Surface energies of Na_2O_2 as a function of μ_O for the most stable terminations of {0001}, $\{1\bar{1}00\}$, and $\{11\bar{2}0\}$ facets at 300 K and 1 atm. The range of μ_O where Na_2O_2 is stable, from the O_2 gas limit to the Na_2O limit, is marked using a yellow box, and the Wulff shapes at these two limits are displayed in (b) and (c), respectively. The color scheme of surface energies used for the Wulff shapes is displayed in the scale bar in meV/Å².

i.e., higher temperature and/or lower P_{O_2}, stoichiometric terminations for the $\{1\bar{1}00\}$ and $\{11\bar{2}0\}$ orientations become more stable than O-rich terminations. In addition, the energies of all of the $\{0001\}$, $\{1\bar{1}00\}$, and $\{11\bar{2}0\}$ orientations become comparable at the most reducing limit, where $\mu_O = -5.82$ eV in equilibrium with Na_2O. The lowest surface energies of Na_2O_2 are in the range of 30–45 meV/Å^2 within the stability window of Na_2O_2.

The Wulff shapes were constructed from the calculated surface energies at the most oxidizing and reducing phase boundaries of Na_2O_2. At the most oxidizing limit, the Wulff shape of Na_2O_2 is a dodecagonal prism, as illustrated in Fig. 19(b). The Wulff shape consists of 37%, 36%, and 26% of the $\{0001\}$, $\{1\bar{1}00\}$, and $\{11\bar{2}0\}$ facets, respectively. At the most reducing limit, the facet composition of the dodecagonal prism Na_2O_2 particle changes to 34%, 19%, and 47% for the $\{0001\}$, $\{1\bar{1}00\}$, and $\{11\bar{2}0\}$ facets, respectively, as shown in Fig. 19(c). As there is no experimental observation of Na_2O_2 particle shapes, comparison of the predicted Wulff shapes with experiments was not feasible.

8.3. Surface orientations considered for $Pa\bar{3}$ NaO_2 and their energies

We considered four surface orientations, $\{100\}$, $\{110\}$, $\{111\}$, and $\{211\}$. A unit cell of $Pa\bar{3}$ NaO_2 (Fig. 11(e)) is rather simple compared with the unit cell of Na_2O_2, as all eight Na ions and four O ions are in the same Wyckoff position groups, respectively. We did not consider the terminations requiring breaking superoxide bonds as they result in high surface energies.[51]

8.3.1. $Pa\bar{3}$ NaO_2 $\{100\}$ surfaces

Along the $\{100\}$ orientation, the $Pa\bar{3}$ NaO_2 crystal is composed of stacking of a single layer, as illustrated in Fig. 20(a). We calculated a stoichiometric (A) Na1-$O_2$1 termination, Na-rich (A) Na1 termination, and O-rich (A) $O_2$1 termination. Their surface energies are listed in Table A 2 in Chapter 8.4. APPENDIX at the most oxidizing and reducing conditions. The lowest surface energy termination for the $\{100\}$ orientation is the

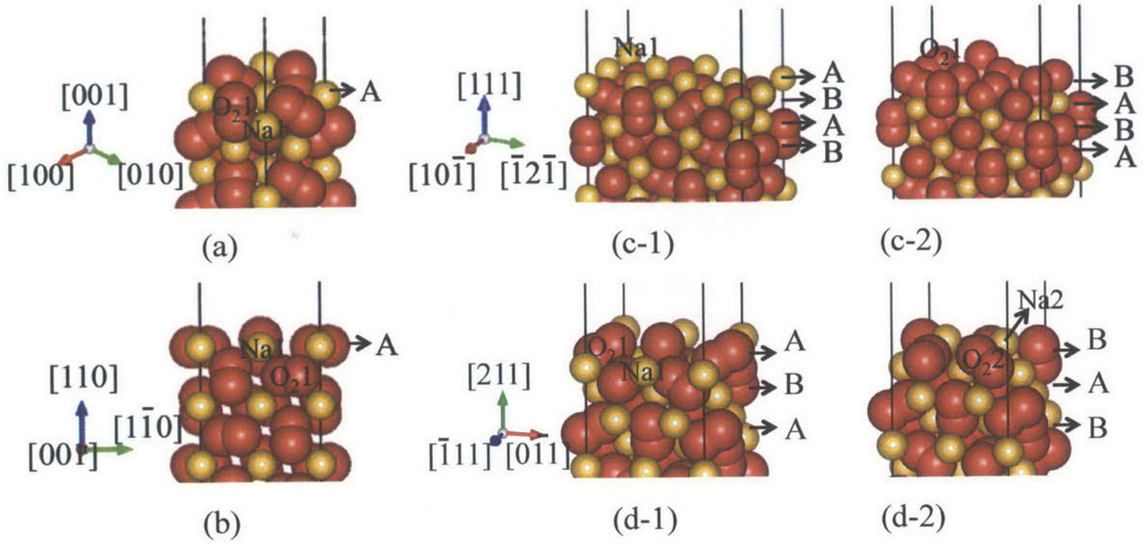

Figure 20. The surface unit cell of Pa$\overline{3}$ NaO_2 in the (a) {100} orientation, (b) {110} orientation, {111} orientation terminated at the (c-1) A layer and (c-2) B layer, and {211} orientation terminated at the (d-1) A layer and (d-2) B layer. The yellow spheres represent Na ions, and the red spheres represent O ions, and the surface ions that are used to define the surface terminations are labeled in the figure.

stoichiometric (A) Na1-$O_2$1 termination shown in Fig. 20(a), and its surface energy is 11.7 meV/Å^2.

8.3.2. Pa$\overline{3}$ NaO_2 {110} surfaces

Along the {110} orientation, the Pa$\overline{3}$ NaO_2 crystal consists of stacking of a single layer, as shown in Fig. 20 (b). We considered three terminations for the {110} orientation, and the O-rich (A) $O_2$1 termination is the lowest energy one within the μ_O window, where metastable NaO_2 exists at 300 K.

8.3.3. Pa$\overline{3}$ NaO_2 {111} surfaces

Along the {111} orientation, the Pa$\overline{3}$ NaO_2 crystal consists of alternate stacking of two different layers, labeled as A and B in Figs. 20(c-1) and 20(c-2), respectively. The A and B layers are Na-rich and O-rich terminations, respectively, and the latter one is the most stable termination at both the most oxidizing and reducing conditions.

8.3.4. Pa$\bar{3}$ NaO_2 {211} surfaces

Along the {211} orientation, the Pa$\bar{3}$ NaO_2 crystal consists of alternate stacking of two different layers, labeled as A and B in Figs. 20(d-1) and 19(d-2), respectively. We considered stoichiometric terminations only for both layers. Their energies are listed in Table A 2 in Chapter 8.4. APPENDIX, and the lowest surface energy termination for the {211} orientation is (A) Na1-$O_2$1 in Fig. 20(d-1).

8.3.5. The lowest surface energies and Wulff shapes of Pa$\bar{3}$ NaO_2 as a function of μ_O

Fig. 21(a) shows the surface energies of the most stable terminations of NaO_2 as a function of μ_O. The μ_O window from where NaO_2 is in equilibrium with Na_2O_2 ($\mu_O = -5.17$ eV) to where NaO_2 is in equilibrium with O_2 gas ($\mu_O = -5.20$ eV) is marked using a yellow box. At μ_O lower than −5.40 eV, the energies of Na-rich {110} and {111}

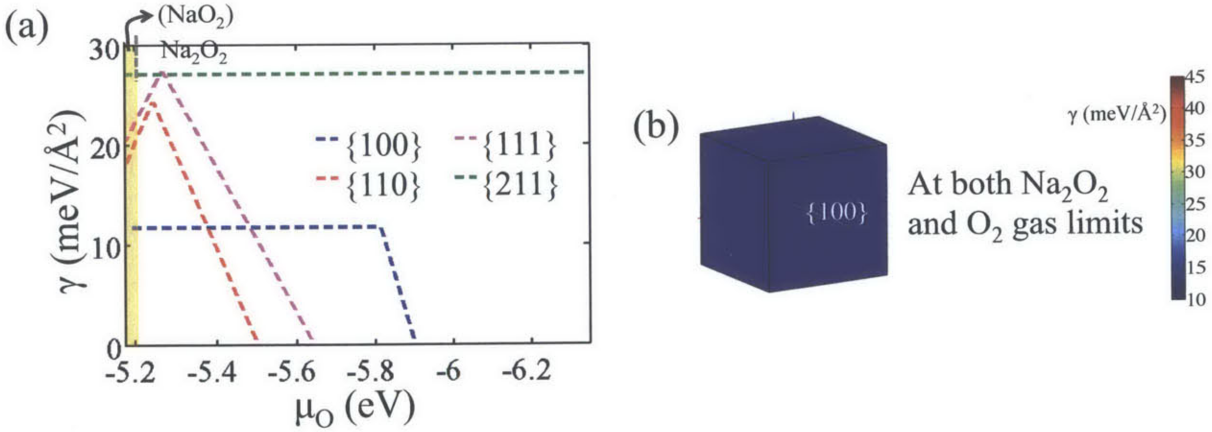

Figure 21. (a) Surface energies of Pa$\bar{3}$ NaO_2 as a function of μ_O for the most stable terminations of the {100}, {110}, {111}, and {211} facets at 300 K and 1 atm. NaO_2 exists as metastable at the standard state; therefore, its equilibrium boundary with Na_2O_2 and O_2 gas, the most oxidizing and reducing conditions, respectively, is considered and marked using a yellow box. The Wulff shapes at these two limits are identical and are represented by the cube displayed in (b). The color scheme of the surface energies used for the Wulff shape is displayed in the scale bar in meV/Å².

terminations are lower than the stoichiometric {100} surface; however, at such a low μ_{O}, NaO_2 becomes more unstable such that it will be hard to nucleate. In most of the μ_{O} range where NaO_2 can possibly be formed (near to the yellow box region), the stoichiometric {100} termination is the lowest energy surface with $\gamma = 11.7\ \mathrm{meV/Å^2}$. Accordingly, the Wulff shape of $Pa\overline{3}$ NaO_2 is a cube, comprised of stoichiometric {100} facets, and it is displayed in Fig. 21(b). This cubic shape is in good agreement with the NaO_2 particles nucleated in Na–O_2 batteries and observed by scanning electron microscopy (SEM).[9, 10] In addition, such a low surface energy of NaO_2 may facilitate its nucleation from nano-size as investigated in our previous study.[57] Note that the conventional surface calculation predicts the Wulff shape of NaO_2 as a cube whose edges and vertices are truncated by {110} and {111} facets at the most oxidizing limit.[52]

8.4. Effect of the oxidation correction energy on the surface energies of Na_2O_2 and $Pa\overline{3}$ NaO_2

In this chapter, we applied our energy correction method that addresses different oxygen valence states (O^{2-}, O_2^{2-}, and O_2^{-}) individually to the surface energy calculations. To compare our results with the conventional surface calculation method that is performed at 0 K without any correction, we listed the calculated surface energies of Na_2O_2 and NaO_2 at {0 K, without E_{oxd}} and {300 K, with E_{oxd}} in Chapter 8.5. APPENDIX. We can see from Tables A 1 and A 2 that the surface energies change significantly from {0 K, without E_{oxd}} to {300 K, with E_{oxd}} for certain terminations, e.g., the energies shift up for Na-rich Na_2O_2 surfaces and shift down for Na-rich NaO_2 surfaces. However, in general, the energies of surfaces comprising Wulff shapes that are either stoichiometric or slightly O-rich terminations only marginally change by less than $5\ \mathrm{meV/Å^2}$ from {0 K, without E_{oxd}} to {300 K, with E_{oxd}}. To assess the effect of our energy correction method, which varies from surface to surface, we break down the change in the surface energies $\Delta\gamma$ into three terms:

i) Δγ due to the temperature increase from 0 K to 300 K. Referring to Eq. (8-5), the only term affected by temperature is μ_{Na}. Therefore, the Δγ due to ΔT can be calculated as

$$\begin{aligned}\Delta\gamma_{\text{by }\Delta\mu(\Delta T)} &= \gamma(300\text{ K}) - \gamma(0\text{ K}) \\ &\cong -\frac{1}{2A}\left(N_{\mathrm{Na}} - \frac{x}{2}N_{\mathrm{O}}\right)\left[\mu_{\mathrm{Na}}^{\mathrm{Na}_x\mathrm{O}_2}(300\text{ K}) - \mu_{\mathrm{Na}}^{\mathrm{Na}_x\mathrm{O}_2}(0\text{ K})\right], \qquad \text{Eq. (8-9)}\end{aligned}$$

and the difference in μ_{Na} between Figs. 15(a-1) and 15(b-1) is plugged into Eq. (8-9);

ii) Δγ due to $\Delta\mu_{\mathrm{Na}}$ originated from the corrected bulk phase energies. Our correction method differentiates the valence states of oxygen, 1.33, 0.85, and 0.23 eV/O_2 for O^{2-}, O_2^{2-}, and O_2^{-}, respectively, which affects on the size of stable domains of bulk Na_xO_y compounds. This in turn alters the absolute values of μ_{Na} at the domain boundaries (see the difference in μ_{Na} between Figs. 15(b-1) and 15(b-2)). The effect of $\Delta\mu_{\mathrm{Na}}$ originated from $E_{\text{oxd, bulk}}$ on the surface energies can be calculated as

$$\Delta\gamma_{\text{by }\Delta\mu(E_{\text{oxd, bulk}})} \cong -\frac{1}{2A}\left(N_{\mathrm{Na}} - \frac{x}{2}N_{\mathrm{O}}\right)\left[\mu_{\mathrm{Na}}^{\mathrm{Na}_x\mathrm{O}_2 \text{ after } E_{\text{oxd}}} - \mu_{\mathrm{Na}}^{\mathrm{Na}_x\mathrm{O}_2 \text{ before } E_{\text{oxd}}}\right]; \qquad \text{Eq. (8-10)}$$

and

iii) Δγ due to the oxidation energy difference between the surface slab and bulk Na_xO_2. In Eq. (8-6), we define $E_{\text{oxd, slab}}$ as the summation of E_{oxd} at different oxidation states v, while the oxidation correction energy applied to the bulk is $E_{\text{oxd, Na}_x\text{O}_2}$ multiplied by the number of formula unit in the surface slab. The difference between these values ΔE_{oxd} contributes to the surface energies as

$$\begin{aligned}\Delta\gamma_{\text{by }\Delta E_{\text{oxd}}} &\cong \frac{1}{2A}\Delta E_{\text{oxd}} \\ &= \frac{1}{2A}\left(-E_{\text{oxd, slab}} + \frac{N_{\mathrm{O}}}{2}E_{\text{oxd, Na}_x\text{O}_2}\right). \qquad \text{Eq. (8-11)}\end{aligned}$$

We calculated Eqs. (8-9), (8-10), and (8-11) and averaged over Na-rich and O-rich surface slabs, respectively. The averaged surface energy change $\langle\Delta\gamma\rangle$ is not an optimal parameter to analyze the effect of contributing parameters because it ignores the degree of non-stoichiometry by which the size of the correction energies is weighted accordingly. However, this parameter can serve as a descriptor that shows the tendency of Δγ attributed to the different terms. The results are listed in Table 5 for Na_2O_2 and in Table 6 for NaO_2.

Table 5. The average surface energy changes ($\langle \Delta\gamma \rangle$ in meV/Å²) between {0 K, without E_{oxd}} and {300 K, with E_{oxd}} for Na-rich or O-rich surface slabs of Na_2O_2. The contribution to the Δγ is divided into three terms: i) $\Delta\mu_{\text{Na}}$ due to ΔT from 0 K to 300 K, ii) $\Delta\mu_{\text{Na}}$ due to the energy correction applied to bulk phases $E_{\text{oxd, bulk}}$, and iii) the oxidation correction energy difference between the surface slab and the bulk, ΔE_{oxd}.

	Na-rich		O-rich	
	Oxidizing limit	Reducing limit	Oxidizing limit	Reducing limit
$N_{\text{Na}} - N_{\text{O}}$	>0		<0	
$\Delta\mu_{\text{Na}}$ by ΔT	0.04	−0.05	0.04	−0.05
$\Delta\mu_{\text{Na}}$ by $E_{\text{oxd, bulk}}$	−0.60	−0.24	−0.60	−0.24
Net $\Delta\mu_{\text{Na}}$	−0.56	−0.29	−0.56	−0.29
$\langle \Delta\gamma \rangle$ by net $\Delta\mu_{\text{Na}}$	~ 19	~ 9	~ −17	~ −11
$\langle \Delta\gamma \rangle$ by ΔE_{oxd}	~ 10		~ 27	
Net $\langle \Delta\gamma \rangle$	~ 29	~ 19	~ 10	~ 17

From Tables 5 and 6, we can clearly see that the materials stability transformed by ΔT and $E_{\text{oxd, bulk}}$ and the ΔE_{oxd} originated from the non-stoichiometry of surface slabs both play an important role in the surface energies. First, for both Na_2O_2 and NaO_2, the materials stability transformed by net $\Delta\mu_{\text{Na}}$ shifts the surface energies of the Na-rich and O-rich terminations in opposite directions, stabilizing O-rich terminations and destabilizing Na-rich terminations. This finding is important because the $\Delta\mu_{\text{Na}}$ effect has been ignored in the conventional surface calculations. Hence, the suitably designed stability of bulk phases and its temperature dependence (e.g., Fig. 15) should not be overlooked, particularly for systems where the phase transformation occurs from 0 K to the given temperature, such as the Na–O system.

Table 6. The average surface energy changes ($\langle \Delta\gamma \rangle$ in meV/Å^2) between {0 K, without E_{oxd}} and {300 K, with E_{oxd}} for Na-rich or O-rich surface slabs of NaO_2. The contribution to the $\Delta\gamma$ is divided into three terms, i) $\Delta\mu_{\text{Na}}(\Delta T)$, ii) $\Delta\mu_{\text{Na}}(E_{\text{oxd, bulk}})$, and iii) ΔE_{oxd}.

	Na-rich		O-rich	
	Oxidizing limit	Reducing limit	Oxidizing limit	Reducing limit
$N_{\text{Na}} - N_{\text{O}}/2$	> 0		< 0	
$\Delta\mu_{\text{Na}}$ by ΔT	0.36	0.04	0.36	0.04
$\Delta\mu_{\text{Na}}$ by $E_{\text{oxd, bulk}}$	−0.48	−0.57	−0.48	−0.57
Net $\Delta\mu_{\text{Na}}$	−0.12	−0.53	−0.12	−0.53
$\langle \Delta\gamma \rangle$ by net $\Delta\mu_{\text{Na}}$	~ 26	~ 5	~ -26	~ -5
$\langle \Delta\gamma \rangle$ by ΔE_{oxd}	~ -31		~ 12	
Net $\langle \Delta\gamma \rangle$	~ -5	~ -27	~ -15	~ 7

On the other hand, the oxidation correction energy difference between the surface slab and bulk works in reverse for non-stoichiometric surfaces. The ΔE_{oxd} raises the energies of O-rich surfaces, while a relatively small increase (Na_2O_2) or even decrease (NaO_2) is imposed on the surface energies of Na-rich terminations. This finding can be understood from the energetics of the surface unit $Na_2O_2^*$ (NaO_2^*) that is transformed to either NaO_2^* or Na_2O^* (O_2^* or $Na_2O_2^*$) by surface cleavage. Suppose we start from a stoichiometric Na_2O_2 surface slab. When we create a Na-rich surface slab by removing one ½ O_2 molecule, one surface unit of $Na_2O_2^*$ is transformed into Na_2O^*. Accordingly, the correction energy applied to Na-rich Na_2O_2 surfaces slab is 1.33/2 = 0.67 eV, while the correction energy applied for the bulk Na_2O_2 is 0.85 eV. Therefore, by the correction energy difference between the bulk and surface slab, 0.85 – 0.67 = 0.18 eV per number of surface $Na_2O_2^*$ units transformed into Na_2O^*, the Na-rich Na_2O_2 surfaces are destabilized. In the same manner, the energies of Na-rich Na_2O_2 surfaces are increased by 0.62 eV/$Na_2O_2^*$ and those of O-rich NaO_2 surfaces are increased by 0.23 eV/NaO_2^*. Even though the degree of non-stoichiometry, i.e., the number of formula units of $Na_2O_2^*$ or NaO_2^* transformed, is neglected, the magnitude of the increase in $\Delta\gamma$ contributed from the ΔE_{oxd} (10, 12, and 27 meV/Å^2 for Na-rich Na_2O_2, O-rich NaO_2, and O-rich Na_2O_2 surfaces, respectively, as listed in Tables 5 and 6) agrees well with this "per formula unit correction energies" in order (0.18, 0.23, and 0.62 eV per $Na_2O_2^*$ or NaO_2^* for Na-rich Na_2O_2, O-rich NaO_2, and O-rich Na_2O_2 surfaces, respectively). Note that Na-rich NaO_2 surfaces are the only terminations for which the energies are lowered by ΔE_{oxd} by −0.20 eV/NaO_2^*.

In total, $\Delta\gamma$ by $\Delta\mu_{Na}$ and ΔE_{oxd} partially cancel each other for all the non-stoichiometric surfaces of Na_2O_2 and NaO_2 except Na-rich Na_2O_2 terminations. For the Na-rich Na_2O_2 surfaces, in addition to the synergic increase in $\Delta\gamma$ by $\Delta\mu_{Na}$ and ΔE_{oxd}, they require payment of the energy cost to break surface O_2^{2-} bonds to transform $Na_2O_2^*$ into Na_2O^*. The high surface energies of Na-rich Na_2O_2 terminations demonstrate such an energy cost (Table A 1 in Chapter 8.5. APPENDIX), and this is why only stoichiometric or O-rich terminations contribute to the Wulff shapes of Na_2O_2 within the stability window.

Now we are in the step to prove that our assumption that the non-stoichiometric surface slabs are regarded as combinations of aliovalent oxides (i.e., NaO_2^* or Na_2O^* on top of Na_2O_2 and O_2^* or $Na_2O_2^*$ on top of NaO_2) is fair by investigating the O–O bond lengths on the surfaces of the slabs. The O–O bond length is a good descriptor to estimate the charge state of oxygen ions because different oxygen valence states have their own distinguishable O–O bond lengths. For example, in GGA-optimized structures, O_2 gas, O_2^- in bulk $Pa\bar{3}$ NaO_2, and O_2^{2-} in bulk Na_2O_2 have bond lengths of 1.23, 1.35, and 1.55 Å (averaged over three O_2^{2-} bonds for Na_2O_2), respectively, and the distance between nearest O–O ions in bulk Na_2O is 3.96 Å. Thus, we chose the surface O_2 ions for which the coordination number has changed by surface cleavage and measured their bond lengths. In Fig. 9, we plot the correction energy applied to the surfaces due to their non-stoichiometry according to Eq. (8-11) versus the measured surface O_2 bond lengths. We added trend-lines obtained by the linear regression for each of the Na-rich and O-rich surface terminations. We can see from Fig. 22 that the Na_2O_2 surfaces can be categorized into two groups: Na_2O_2 surfaces on which O_2^{2-*} bonds undergo bond breaking and Na_2O_2 surfaces on which O_2^{2-*} bonds shortened

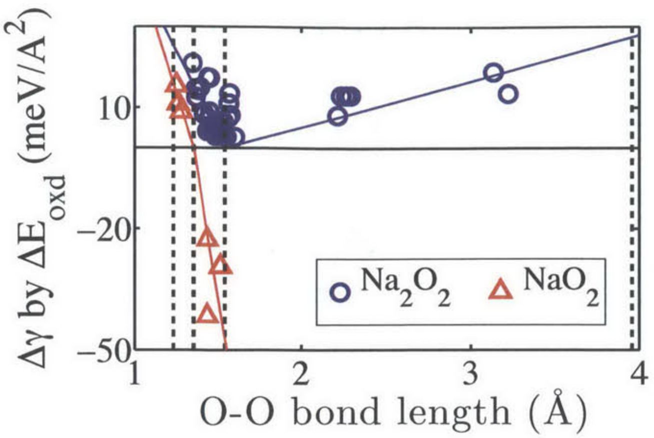

Figure 22. The correction energy applied to the surface energies by Eq. (8-11) as a function of the surface O–O bond lengths of all the surface terminations we considered for Na_2O_2 (blue circles) and NaO_2 (red triangles). The dashed vertical lines indicate the O_2 bond lengths in O_2 gas (1.23 Å), bulk $Pa\overline{3}$ NaO_2 (1.35 Å), and bulk Na_2O_2 (1.55 Å averaged over three O_2 bonds) and the distance between nearest O–O ions in bulk Na_2O (3.96 Å) from left to right. The blue and red lines are obtained from the linear regression for each non-stoichiometric surface group (Na-rich or O-rich) centering on the O_2^{2-} and O_2^{-} bond lengths in their bulk states, respectively.

close to O_2^{-}. In the same manner, the NaO_2 surfaces can be categorized into one with O_2^{-*} bonds shrunk near to the bond length of O_2 gas and the other one with O_2^{-*} bonds elongated toward the O_2^{2-} bond length. The oxidation correction energy applied to each group has a distinct tendency as demonstrated by the trend-lines, indicating that our underlying assumption in Eq. (8-6) can be justified by the correlation between ΔE_{oxd} and the optimized surface O_2 bond lengths.

Finally, we want to assess the effect of the oxidation correction energy we applied. Due to the partial cancellation between the parameters, Δγ by $\Delta\mu_{\mathrm{Na}}$ and ΔE_{oxd}, and intrinsically high surface energies for certain terminations, e.g., Na-rich Na_2O_2 surfaces, there is no large difference between the lowest surface energies evaluated at {0 K without ΔE_{oxd}} and {300 K with ΔE_{oxd}} for both Na_2O_2 and NaO_2 (Tables A 1 and A 2). Because the lowest energy surfaces are the most important ones to determine the particle polymorphs, surface reactivity, etc., the oxidation correction energy appears to have only a minor effect for this case we studied.

However, when the chemical potential window of the materials stability shifts further due to, for instance, oxygen partial pressure, it is possible that the Wulff shape and/or its composing surface structures are altered before and after the correction energy is applied because the oxidation correction energy may stabilize one of the metal-rich and oxygen-rich surfaces while destabilizing the other, as observed in Tables 5 and 6. To determine if the surface structures evolve under different conditions, we tested the surface structures of Na_2O_2 at 900 K, a typical temperature where Na_2O_2 is used as an oxidant.[116, 117] At 900 K, we observed that although the surface energies of Na_2O_2 are still in the range of 35–45 meV/Å^2, the O-rich terminations that were once the lowest energy terminations at 300 K are destabilized by E_{oxd}. Instead, only stoichiometric terminations, (B) Na4-Na5-Na6-$O_2$2-$O_2$3 for the $\{0001\}$ orientation, (A) Na1-Na2-$O_2$1 for the $\{1\bar{1}00\}$ orientation, and (C) Na4-Na5-Na6 for the $\{11\bar{2}0\}$ orientation, remain stable in all range of μ_{Na} within the stability window. This finding is in good agreement with the experimental finding by Otsuka *et al.* that the rate of the hydrogen abstraction reaction, which is activated by surface O_2^{2-*} ions on Na_2O_2, is insensitive to the oxygen partial pressure.[116] In contrast, when E_{oxd} is not applied, even Na_2O_2 is not a stable phase, and moreover, its lowest energy surfaces are still O-rich dominant and dependent on μ_{Na}.

8.5. APPENDIX: Surface energies of Na_2O_2 and $Pa\bar{3}$ NaO_2

Table A 1. Surface energies (in meV/$Å^2$) of different orientations and terminations of Na_2O_2 at 0 K without E_{oxd}, the correction energy difference between the surface slab and bulk Na_2O_2 (ΔE_{oxd}), which is the net correction energy applied to the surface energies, and the corrected surface energies at 300 K. The NaO_2 limit (O_2 gas limit) represents the most oxidizing condition, and the Na_2O limit (Na_2O limit) represents the most reducing condition for Na_2O_2 at 0 K (300 K). The lowest energy terminations are marked in bold for each condition.

Orien-tation	Termination	Note	0 K, w/o E_{oxd}		ΔE_{oxd}	300 K, w/ E_{oxd}	
			NaO_2 limit	Na_2O limit		O_2 gas limit	Na_2O limit
{0001}	(A) Na1-Na2-Na3-O_2	Na-rich	57.42	52.30	2.70	68.24	59.17
	(A) Na1-Na2-$O_2$1	O-rich	37.22	42.34	9.07	38.17	47.25
	(A) Na1-$O_2$1	O-rich	30.93	46.28	27.22	33.77	60.99
	(A) $O_2$1	O-rich	32.34	57.94	45.37	37.09	82.45
	(A) Na1-Na2-Na3	Na-rich	111.22	85.62	13.50	165.34	119.98
	(B) Na4-Na5-Na6-$O_2$2-$O_2$3	O-rich	**29.73**	**34.85**	9.07	**30.68**	**39.75**
	(B) Na4-Na5- $O_2$2-$O_2$3	O-rich	34.69	50.04	27.22	37.54	64.75
	(B) Na4- $O_2$2-$O_2$3	O-rich	35.57	61.16	45.37	40.32	85.68
	(B) $O_2$2-$O_2$3	O-rich	45.62	81.45	63.52	52.26	115.77
	(B) Na4-Na5-Na6- $O_2$2	Na-rich	96.95	81.59	8.10	129.42	102.20
	(B) Na4-Na5- $O_2$2	Na-rich	84.82	79.70	2.70	95.64	86.57
	(B) Na4- $O_2$2	O-rich	46.28	51.40	9.07	47.23	56.31
	(B) $O_2$2	O-rich	41.52	56.88	27.22	44.37	71.59
	(B) Na4-Na5-Na6	Na-rich	182.97	147.14	18.90	258.75	195.24
	(B) Na4-Na5	Na-rich	173.15	147.55	13.50	227.27	181.91
	(B) Na4	Na-rich	120.42	105.07	8.10	152.90	125.68
$\{1\bar{1}00\}$	(A) Na1-Na2-$O_2$1	Stoi.	43.15	**43.15**	0.00	43.15	**43.15**

	(A) Na1- $O_2$1	O-rich	35.21	47.52	21.81	37.50	59.30
	(A) Na2- $O_2$1	O-rich	41.24	53.52	21.78	43.51	65.29
	(A) $O_2$1	O-rich	**33.25**	57.67	43.30	37.78	81.07
	(A) Na1-Na2	Na-rich	150.26	125.55	13.04	202.52	158.72
	(B) Na3-Na4- $O_2$2	Stoi.	47.76	47.76	0.00	47.76	47.76
	(B) Na3- $O_2$2	O-rich	37.26	49.47	21.65	39.52	61.17
	(B) Na4- $O_2$2	O-rich	33.98	46.49	22.18	**36.30**	58.47
	(B) $O_2$2	O-rich	32.53	57.15	43.64	37.10	80.73
	(B) Na3-Na4	Na-rich	150.66	125.95	13.04	202.92	159.12
	(B) Na4	Na-rich	103.48	91.12	6.52	129.61	107.71
	(B′) Na5-Na6- $O_2$3	Stoi.	55.76	55.76	0.00	55.76	55.76
	(B′) Na5- $O_2$3	O-rich	41.10	53.45	21.90	43.39	65.29
	(B′) Na6- $O_2$3	O-rich	39.96	52.32	21.90	42.26	64.16
	(B′) $O_2$3	O-rich	40.56	65.28	43.81	45.15	88.95
	(B′) Na5-Na6	Na-rich	154.46	129.75	13.04	206.72	162.92
	(B′) Na5	Na-rich	110.18	97.83	6.52	136.31	114.41
$\{11\bar{2}0\}$	(A) $O_2$1-$O_2$2-$O_2$3	O-rich	**33.13**	54.61	38.08	**37.12**	75.19
	(A) $O_2$2-$O_2$3	O-rich	57.09	64.27	12.74	58.42	71.16
	(A) $O_2$1-$O_2$2	O-rich	57.09	64.28	12.74	58.42	71.16
	(A) $O_2$2	Na-rich	104.78	97.65	17.34	133.45	120.80
	(A) $O_2$1	Na-rich	104.99	97.81	17.47	133.87	121.13
	(B) Na1-Na2-Na3	Na-rich	140.51	119.60	11.03	184.74	147.67
	(B) Na1-Na2	Na-rich	113.60	99.33	7.53	143.77	118.48
	(B) Na1	Na-rich	72.78	65.64	3.76	87.86	75.22
	(C) Na4-Na5-Na6	Stoi.	40.54	**40.54**	0.00	40.54	**40.54**
	(C) Na4-Na5	O-rich	37.13	44.26	12.65	38.45	51.10
	(C) Na4	O-rich	38.09	52.36	25.29	40.74	66.02

Table A 2. Surface energies (in meV/Å^2) of different orientations and terminations of Pa$\overline{3}$ NaO_2 at 0 K without E_{oxd}, the correction energy difference between the surface slab and bulk NaO_2 (ΔE_{oxd}), which is the net correction energy applied to the surface energies, and the corrected surface energies at 300 K. The O_2 gas limit (Na_2O_2 limit) represents the most oxidizing condition, and the Na_2O_2 limit (O_2 gas limit) represents the most reducing condition for Na_2O_2 at 0 K (300 K). The lowest energy terminations are marked in bold for each condition.

Orien-tation	Termination	Note	0 K, w/o E_{oxd}		ΔE_{oxd}	300 K, w/ E_{oxd}	
			O_2 gas limit	Na_2O_2 limit		Na_2O_2 limit	O_2 gas limit
{100}	(A) Na1-$O_2$1	Stoi.	**11.73**	**11.73**	0.00	**11.73**	**11.73**
	(A) Na1	Na-rich	128.43	103.43	-41.58	96.57	92.85
	(A) $O_2$1	O-rich	38.83	63.83	15.42	44.53	48.25
{110}	(A) Na1-$O_2$1	Stoi.	22.43	**22.43**	0.00	22.43	22.43
	(A) Na1	Na-rich	52.94	35.26	-29.40	30.41	27.78
	(A) $O_2$1	O-rich	**13.99**	31.67	10.91	**18.02**	**20.65**
{111}	(A) Na1	Na-rich	51.07	37.47	-22.63	33.74	31.71
	(B) $O_2$1	O-rich	**17.16**	**31.59**	8.91	**20.45**	**22.60**
{211}	(A) Na1-$O_2$1	Stoi.	**27.09**	**27.09**	0.00	**27.09**	**27.09**
	(B) Na2-$O_2$2	Stoi.	29.35	29.35	0.00	27.09	27.09

Chapter 9. Nano-Particle Stabilization in Sodium Oxides and Understanding of the Discharging Thermodynamics in Na-Air Batteries

9.1. Particle-size-dependent phase diagram of Na_xO_2

The relative stability of Na_2O_2 and $Fm\bar{3}m$ NaO_2 nanoparticles is investigated by combining the formation free energy of the bulk obtained from Chapter 7.1 and the surface energies obtained from Chapter 8.1. The phase diagram of nanoparticles is constructed as a function of temperature, O_2 partial pressure and particle size.

9.1.1. Formalism for particle-size-dependent formation free energy

The formation free energy of a particle with unit volume (V_1 = 1 Å^3) is calculated as

$$\begin{aligned}\Delta\bar{G}_{\text{form}}\left(T,P_{O_2}\right) &= \Delta G_{\text{form}}^{\text{bulk}}\left(T,P_{O_2}\right)+\sum_i \gamma_i\left(T,P_{O_2}\right)\cdot A_{1,i} \\ &\equiv \Delta G_{\text{form}}^{\text{bulk}}\left(T,P_{O_2}\right)+\bar{\gamma}\left(T,P_{O_2}\right)\cdot \sum_i A_{1,i}\ , \qquad \text{Eq. (9-1)}\end{aligned}$$

where $\Delta G_{\text{form}}^{\text{bulk}}$ is the formation energy of bulk Na_xO_2 in eV/Å^3 unit obtained from Eq. (7-7) and γ_i is the surface energy of the i facet in the predicted Wulff shape in eV/Å^2 unit obtained from Eq. (8-5). We defined $A_{1,i}$ as the surface area of the i facet in Å^2/Å^3 unit for a unit volume particle. The normalized total surface energy $\bar{\gamma}$ is defined as

$$\bar{\gamma}\left(T,P_{O_2}\right)\equiv\frac{\sum_i \gamma_i\left(T,P_{O_2}\right)\cdot A_{1,i}}{\sum_i A_{1,i}}\ , \qquad \text{Eq. (9-2)}$$

representing the net free energy contributed from surface energies. The normalized total surface energy $\bar{\gamma}$ is integrated over the different surface facets comprised of the Wulff shapes and normalized by the surface area in eV/Å^2 unit. Using the surface energies obtained in Chapter 8.1, we obtained $\bar{\gamma}$ for Na_2O_2 as 0.178 and 0.196 eV/Å^3 at 300 K at the most oxidizing and reducing conditions, respectively, and 0.070 eV/Å^3 for $Pa\bar{3}$ NaO_2 at both the most oxidizing and reducing conditions.

For a particle with an arbitrary particle size d (Å), where the particle volume $V_2 = d^3 \times V_1 = d^3$, the surface area of the i facet can be calculated as $A_{2,i} = d^2 \times A_{1,i}$. The formation energy of a particle with an arbitrary particle size d can be calculated as

$$\begin{aligned}\Delta G_{\text{form}}\left(d,T,P_{\mathrm{O}_2}\right) &= \Delta G_{\text{form}}^{\text{bulk}}\left(T,P_{\mathrm{O}_2}\right)\cdot V_2 + \sum_i \gamma_i\left(T,P_{\mathrm{O}_2}\right)\cdot A_{2,i} \\ &\equiv \Delta G_{\text{form}}^{\text{bulk}}\left(T,P_{\mathrm{O}_2}\right)\cdot d^3 + \sum_i \gamma_i\left(T,P_{\mathrm{O}_2}\right)\cdot d^2\cdot A_{1,i} \\ &= \Delta G_{\text{form}}^{\text{bulk}}\left(T,P_{\mathrm{O}_2}\right)\cdot d^3 + \bar{\gamma}\left(T,P_{\mathrm{O}_2}\right)\cdot d^2\end{aligned} \quad \text{Eq. (9-3)}$$

9.1.2. Phase diagram as a function of particle size

Fig. 23 presents the calculated phase diagram as a function of particle size and O_2 partial pressure. The phase diagram is calculated at the O_2 gas limit; however, the phase diagrams under other conditions share the same features. Similar to the bulk phases, Na_2O_2 is stable at lower P_{O_2}, while NaO_2 becomes stabilized at higher P_{O_2}. When the particle size decreases, the formation of NaO_2 is preferred due to the lower surface energies of NaO_2. The particle size at which Na_2O_2 becomes more stable than NaO_2 at P_{O_2} = 1 atm is ~6 nm at the

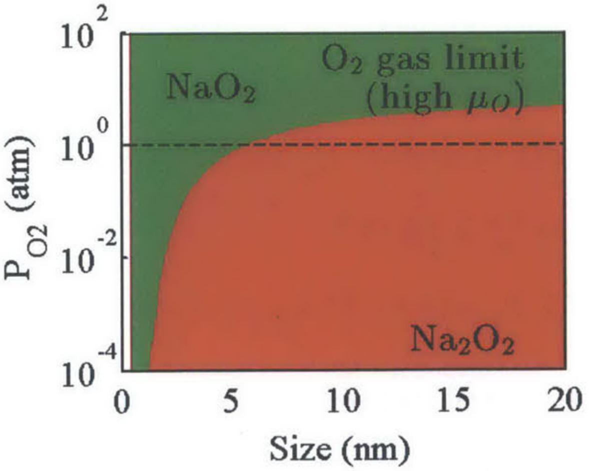

Figure 23. Phase diagram of Na_2O_2 (red) and NaO_2 (green) at 300 K as a function of particle size and P_{O_2} at the O_2 gas limit. The particle size is defined as $(V^0)^{1/3}$, where V^0 is the total volume of the particle. Reprinted with permission from Kang, S.; Mo, Y.; Ong, S. P.; Ceder, G. *Nano Letters* **2014,** 14 (2), 1016-1020. Copyright 2014 American Chemical Society.

O_2 gas limit. In addition, higher P_{O_2} promotes the stability of larger NaO_2 particles. For example, at P_{O_2} = 4 atm, the size of the stable NaO_2 particle is greater than 20 nm.

9.2. Kinetics in nucleation of Na_2O_2 and $Fm\bar{3}m$ NaO_2 nanoparticles

To further evaluate the initial stage of nucleation during discharge of a Na–O_2 battery, we calculated the critical nucleus size d^* and the critical nucleation energy barrier ΔG^* of Na_2O_2 and NaO_2 particles.

9.2.1. Formalism for critical nucleus size of Na_2O_2 and $Fm\bar{3}m$ NaO_2 nanoparticles and their nucleation energy barrier

We calculated the critical nucleus size using the P_{O_2} and/or the electrochemical potential ϕ as a driving force for nucleation:

$$\Delta G_v\left(T,P_{O_2},\phi\right)=\frac{\Delta G_{\text{form}}^{\text{Na}_x\text{O}_2}\left(T,1\text{ atm},\phi_{\text{eq}}^{\text{Na}_x\text{O}_2}\right)+xF\phi-k_BT\ln P_{O_2}}{xV^{\text{Na}_x\text{O}_2}}, \qquad \text{Eq. (9-4)}$$

where $\Delta G_{\text{form}}^{\text{Na}_x\text{O}_2}$ is the formation free energy of bulk Na_xO_2 at a given temperature T, P_{O_2} = 1 atm and its equilibrium potential $\phi_{\text{eq}}^{\text{Na}_x\text{O}_2}$, F is the Faraday constant, and $V^{\text{Na}_x\text{O}_2}$ is the volume of Na_xO_2 in Å^3 per formula unit. The nucleation driving force ΔG_v is the normalized formation free energy of Na_xO_2 at arbitrary P_{O_2} and electrochemical potential ϕ in eV/Å^3 per Na. We plugged ΔG_v into $\Delta G_{\text{form}}^{\text{bulk}}$ in Eq. (9-3):

$$\Delta G_{\text{form}}\left(d,T,P_{O_2},\phi\right)=\Delta G_v\left(T,P_{O_2},\phi\right)\cdot d^3+\bar{\gamma}\left(T,P_{O_2}\right)\cdot d^2 \qquad \text{Eq. (9-5)}$$

and calculated the size of the critical nucleus when $\partial\Delta G_{\text{form}}\left(d,T,P_{O_2},\phi\right)/\partial d=0$.

The critical nucleus size, $(d^*)^3$, represents the particle volume beyond which the particle growth is energetically favorable; ΔG^* is the free energy required to form this critical nucleus size. These parameters can be calculated as

$$d^{*}=-\frac{2\bar{\gamma}\left(T,P_{\mathrm{O}_2}\right)}{3\Delta G_{v}\left(T,P_{\mathrm{O}_2},\phi\right)},\qquad \text{Eq. (9-6)}$$

and

$$\Delta G^{*}=\frac{4\left\{\bar{\gamma}\left(T,P_{\mathrm{O}_2}\right)\right\}^{3}}{27\left\{\Delta G_{v}\left(T,P_{\mathrm{O}_2},\phi\right)\right\}^{2}}.\qquad \text{Eq. (9-7)}$$

Note that we plugged in the normalized total surface energy $\bar{\gamma}$ at all P_{O_2} conditions that are calculated at the O_2 gas limit at $T = 300$ K and $P_{\mathrm{O}_2} = 1$ atm because the standard state (300 K and 1 atm) is the typical initial setting for Na–O_2 batteries. In addition, in terms of computational convenience, because P_{O_2} alters the stability window of compounds (Fig. 15), $\bar{\gamma}$ as a function of P_{O_2} makes the calculation much more complicated. However, considering P_{O_2} change by $O(10^2)$, e.g., from 1 atm to either 100 atm or 10^{-2} atm, only shifts μ_{O} by < 0.06 eV, $\bar{\gamma}$ as a function of P_{O_2} is expected to have only a minor effect.

9.2.2. Results

We calculated d^{*} and ΔG^{*} as a function of P_{O_2} when the applied potential is 2.1 V versus Na/Na^{+}, corresponding to 0.21 and 0.18 V below the calculated equilibrium potentials for the formation of both Na_2O_2 and NaO_2, respectively (Table 4). Under this condition, the critical nucleus size for NaO_2 is smaller than that for Na_2O_2 at P_{O_2} higher than ~0.005 atm (Fig. 24(a)). In addition, the nucleation energy barrier for Na_2O_2 is consistently much higher than that of NaO_2 (Fig. 24(b)). Therefore, NaO_2 particles are more likely to nucleate because of their smaller critical nucleus size and lower nucleation energy barrier than Na_2O_2. The fact that NaO_2 nucleates with a much lower energy barrier and smaller critical nucleus size than Na_2O_2 holds for all discharge potentials, as shown in Figs. 24(c) and 24(d). Furthermore, a higher P_{O_2} significantly reduces the critical nucleus size and critical energy barrier for NaO_2 particles; the critical nucleus size is less than 1 nm at $P_{\mathrm{O}_2} = 1$ atm (Fig. 24).

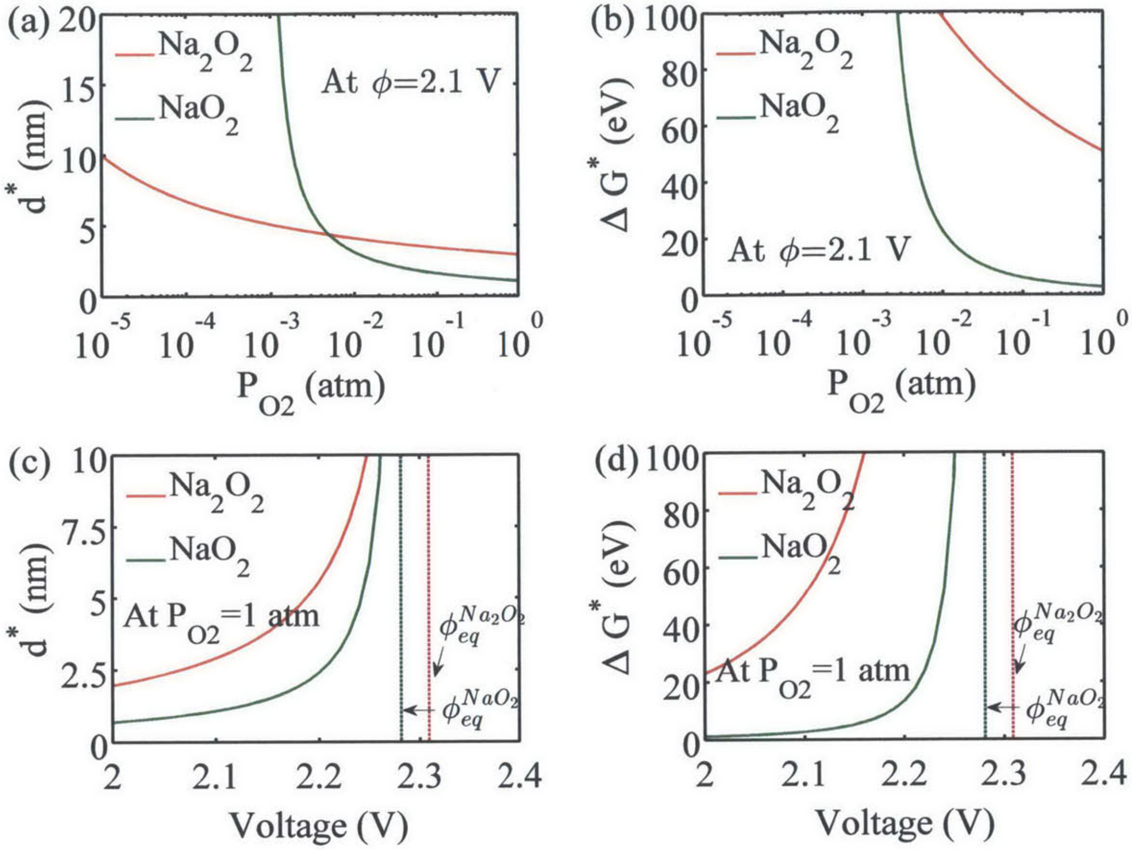

Figure 24. (a, c) The critical nucleus size and (b, d) critical nucleation energy barrier of Na_2O_2 and NaO_2 particles as a function of P_{O_2} at ϕ = 2.1 V vs. Na/Na^+ ((a) and (b)) and as a function of voltage at P_{O_2} = 1 atm ((c) and (d)). The applied potential 2.1 V for (a) and (b) is 0.21 and 0.18 V lower than the calculated equilibrium potentials of Na_2O_2 and NaO_2, respectively. These equilibrium potentials of Na_2O_2 and NaO_2 are marked by vertical lines in (c) and (d). Reprinted with permission from Kang, S.; Mo, Y.; Ong, S. P.; Ceder, G. *Nano Letters* **2014,** 14 (2), 1016-1020. Copyright 2014 American Chemical Society.

9.3. Conclusion: Implication to the thermodynamics in discharge products in Na–O_2 batteries

We are now in a position to shed light on what controls the formation of either NaO_2 or Na_2O_2 during the discharge of Na–O_2 batteries. Considering the formation energy of bulk phases, one may expect that Na_2O_2 will be the dominant product at the standard condition

(300 K and 1 atm), and NaO_2 will form only at extremely high P_{O_2} (> 8.5atm) (Fig. 14). However, when the effect of surface energy is considered, our computational results reveal that the lower surface energy of NaO_2 stabilizes small NaO_2 particles over Na_2O_2 particles, resulting in the preferred nucleation of NaO_2 nanoparticles at any given temperature, O_2 pressure and chemical potential (Fig. 23). Given the distinct structure of NaO_2 and Na_2O_2 and the fact that the energy difference between NaO_2 and Na_2O_2 is small (20 meV/Na at $d = 20$ nm, and 30 meV/Na in bulk), these particles may never transform into Na_2O_2, thus remaining metastable. We believe that this phenomenon may explain the observation of μm-sized NaO_2 particles by Hartmann *et al.*[9, 10] The formation of Na_2O_2 may be favored by poor oxygen transport in the electrode caused by, for example, pore clogging. Pore clogging interrupts the O_2 supply to nucleation sites and lowers the formation free energy of bulk Na_2O_2. For example, when the local P_{O_2} decreases to 10^{-3} atm, Na_2O_2 particles larger than 1.5 nm become energetically stable (Fig. 23), and when they reach their critical nucleus size, 2.1 nm, there is no obstacle to the nucleation of Na_2O_2. Thus, to promote NaO_2 formation, it is critical to ensure an O_2 supply by deploying cathode microstructures with high pore-density and/or suitable electrolytes rendering appropriate O_2 solubility and diffusion.[118-120]

As the stability of the superoxide is possibly a key parameter in designing viable metal-air batteries, as described in Chapter 6, our finding that the formation of the superoxide is controlled by its substantially lower nucleation energy at the nanoscale over peroxide may be particularly important for designing reversible Na–O_2 systems as well as other air batteries.

In summary, we investigated the relative phase stability of Na_2O_2 and NaO_2 as a function of temperature, O_2 partial pressure, and particle size. Our results confirm that in bulk, Na_2O_2 is stable, and NaO_2 is metastable at standard conditions. As the superoxide NaO_2 has a much lower surface energy than the peroxide, it is stabilized when the particle size is in the nanometer regime where nucleation occurs. Our results further reveal that the O_2 partial pressure is a significant parameter in determining the formation and growth of a particular sodium oxide phase. For higher O_2 pressure, the energy barrier to nucleate NaO_2 is reduced, and the superoxide remains thermodynamically stable up to larger particle sizes, thereby reducing the possibility that it transforms to the peroxide upon growth.

We expect that our findings will direct efforts toward understanding and controlling the formation of desired Na–O compounds in battery operation and further invigorate interest in the potential of Na–O_2 batteries.

References

(1) Hayner, C. M.; Zhao, X.; Kung, H. H. *Annual Review of Chemical and Biomolecular Engineering* **2012,** 3 (1), 445-471.

(2) Rahman, M. A.; Wang, X.; Wen, C. *Journal of The Electrochemical Society* **2013,** 160 (10), A1759-A1771.

(3) Etacheri, V.; Marom, R.; Elazari, R.; Salitra, G.; Aurbach, D. *Energy & Environmental Science* **2011,** 4 (9), 3243-3262.

(4) Cheng, F.; Chen, J. *Chemical Society Reviews* **2012,** 41 (6), 2172-2192.

(5) Lee, J.-S.; Tai Kim, S.; Cao, R.; Choi, N.-S.; Liu, M.; Lee, K. T.; Cho, J. *Advanced Energy Materials* **2011,** 1 (1), 34-50.

(6) Ren, X.; Wu, Y. *Journal of the American Chemical Society* **2013,** 135 (8), 2923-2926.

(7) Christensen, J.; Albertus, P.; Sanchez-Carrera, R. S.; Lohmann, T.; Kozinsky, B.; Liedtke, R.; Ahmed, J.; Kojic, A. *Journal of the Electrochemical Society* **2012,** 159 (2), R1-R30.

(8) Li, F.; Zhang, T.; Zhou, H. *Energy & Environmental Science* **2013,** 6 (4), 1125-1141.

(9) Hartmann, P.; Bender, C. L.; Vracar, M.; Durr, A. K.; Garsuch, A.; Janek, J.; Adelhelm, P. *Nat Mater* **2013,** 12 (3), 228-232.

(10) Hartmann, P.; Bender, C. L.; Sann, J.; Durr, A. K.; Jansen, M.; Janek, J.; Adelhelm, P. *Physical Chemistry Chemical Physics* **2013,** 15 (28), 11661-11672.

(11) Wriedt, H. A. *Bulletin of Alloy Phase Diagrams* **1987,** 8 (3), 234-246.

(12) Sangster, J.; Pelton, A. D. *JPE* **1992,** 13 (3), 296-299.

(13) Bruce, P. G.; Freunberger, S. A.; Hardwick, L. J.; Tarascon, J.-M. *Nature Materials* **2012,** 11 (1), 19-29.

(14) Mizuno, F.; Nakanishi, S.; Kotani, Y.; Yokoishi, S.; Iba, H. *Electrochemistry* **2010,** 78 (5), 403-405.

(15) Freunberger, S. A.; Chen, Y. H.; Peng, Z. Q.; Griffin, J. M.; Hardwick, L. J.; Barde, F.; Novak, P.; Bruce, P. G. *Journal of the American Chemical Society* **2011,** 133 (20), 8040-8047.

(16) McCloskey, B. D.; Bethune, D. S.; Shelby, R. M.; Girishkumar, G.; Luntz, A. C. *Journal of Physical Chemistry Letters* **2011,** 2 (10), 1161-1166.

(17) Bryantsev, V. S.; Faglioni, F. *J Phys Chem A* **2012,** 116 (26), 7128-7138.

(18) Bryantsev, V. S.; Giordani, V.; Walker, W.; Blanco, M.; Zecevic, S.; Sasaki, K.; Uddin, J.; Addison, D.; Chase, G. V. *J Phys Chem A* **2011,** 115 (44), 12399-12409.

(19) Chen, Y.; Freunberger, S. A.; Peng, Z.; Barde, F.; Bruce, P. G. *Journal of the American Chemical Society* **2012,** 134 (18), 7952-7957.

(20) Freunberger, S. A.; Chen, Y. H.; Drewett, N. E.; Hardwick, L. J.; Barde, F.; Bruce, P. G. *Angewandte Chemie-International Edition* **2011,** 50 (37), 8609-8613.

(21) Laoire, C. O.; Mukerjee, S.; Abraham, K. M.; Plichta, E. J.; Hendrickson, M. A. *Journal of Physical Chemistry C* **2010,** 114 (19), 9178-9186.

(22) Lu, Y. C.; Gasteiger, H. A.; Crumlin, E.; McGuire, R.; Shao-Horn, Y. *Journal of the Electrochemical Society* **2010,** 157 (9), A1016-A1025.

(23) Peng, Z. Q.; Freunberger, S. A.; Hardwick, L. J.; Chen, Y. H.; Giordani, V.; Barde, F.; Novak, P.; Graham, D.; Tarascon, J. M.; Bruce, P. G. *Angewandte Chemie-International Edition* **2011,** 50 (28), 6351-6355.

(24) Black, R.; Oh, S. H.; Lee, J. H.; Yim, T.; Adams, B.; Nazar, L. F. *Journal of the American Chemical Society* **2012,** 134 (6), 2902-2905.

(25) Ottakam Thotiyl, M. M.; Freunberger, S. A.; Peng, Z.; Bruce, P. G. *Journal of the American Chemical Society* **2012,** 135 (1), 494-500.

(26) Peng, Z. Q.; Freunberger, S. A.; Chen, Y. H.; Bruce, P. G. *Science* **2012,** 337 (6094), 563-566.

(27) Riaz, A.; Jung, K.-N.; Chang, W.; Lee, S.-B.; Lim, T.-H.; Park, S.-J.; Song, R.-H.; Yoon, S.; Shin, K.-H.; Lee, J.-W. *Chemical Communications* **2013,** 49 (53), 5984-5986.

(28) Ottakam Thotiyl, M. M.; Freunberger, S. A.; Peng, Z.; Chen, Y.; Liu, Z.; Bruce, P. G. *Nat Mater* **2013,** 12 (11), 1050-1056.

(29) Li, F.; Tang, D.-M.; Chen, Y.; Golberg, D.; Kitaura, H.; Zhang, T.; Yamada, A.; Zhou, H. *Nano Letters* **2013,** 13 (10), 4702-4707.

(30) Chen, Y.; Freunberger, S. A.; Peng, Z.; Fontaine, O.; Bruce, P. G. *Nat Chem* **2013,** 5 (6), 489-494.

(31) Lim, H.-D.; Song, H.; Kim, J.; Gwon, H.; Bae, Y.; Park, K.-Y.; Hong, J.; Kim, H.; Kim, T.; Kim, Y. H.; Lepró, X.; Ovalle-Robles, R.; Baughman, R. H.; Kang, K. *Angewandte Chemie International Edition* **2014,** 53 (15), 3926-3931.

(32) Jian, Z.; Chen, Y.; Li, F.; Zhang, T.; Liu, C.; Zhou, H. *Journal of Power Sources* **2014,** 251 (0), 466-469.

(33) Liu, W.; Sun, Q.; Yang, Y.; Xie, J.-Y.; Fu, Z.-W. *Chemical Communications* **2013,** 49 (19), 1951-1953.

(34) Peled, E.; Golodnitsky, D.; Mazor, H.; Goor, M.; Avshalomov, S. *Journal of Power Sources* **2011,** 196 (16), 6835-6840.

(35) Kim, J.; Lim, H.-D.; Gwon, H.; Kang, K. *Physical Chemistry Chemical Physics* **2013,** 15 (10), 3623-3629.

(36) Perdew, J. P.; Burke, K.; Ernzerhof, M. *Physical Review Letters* **1996,** 77 (18), 3865-3868.

(37) Heyd, J.; Scuseria, G. E.; Ernzerhof, M. *The Journal of Chemical Physics* **2003,** 118 (18), 8207-8215.

(38) Heyd, J.; Scuseria, G. E.; Ernzerhof, M. *The Journal of Chemical Physics* **2006,** 124 (21), 219906-219901.

(39) Sun, J.; Marsman, M.; Csonka, G. b. I.; Ruzsinszky, A.; Hao, P.; Kim, Y.-S.; Kresse, G.; Perdew, J. P. *Physical Review B* **2011,** 84 (3), 035117.

(40) Chevrier, V. L.; Ong, S. P.; Armiento, R.; Chan, M. K. Y.; Ceder, G. *Physical Review B* **2010,** 82 (7), 075122.

(41) Heyd, J.; Scuseria, G. E. *The Journal of Chemical Physics* **2004,** 121 (3), 1187-1192.

(42) Heyd, J.; Scuseria, G. E.; Ernzerhof, M. *Journal of Chemical Physics* **2006,** 124 (21), 219906.

(43) Hummer, K.; Harl, J.; Kresse, G. *Physical Review B* **2009,** 80 (11), 115205.

(44) Krukau, A. V.; Vydrov, O. A.; Izmaylov, A. F.; Scuseria, G. E. *The Journal of Chemical Physics* **2006,** 125 (22), -.

(45) Kresse, G.; Furthmuller, J. *Physical Review B* **1996,** 54 (16), 11169-11186.

(46) Blochl, P. E. *Physical Review B* **1994,** 50 (24), 17953-17979.

(47) Wang, L.; Maxisch, T.; Ceder, G. *Physical Review B* **2006,** 73 (19), 1-6.

(48) Ong, S. P.; Jain, A.; Hautier, G.; Kang, B.; Ceder, G. *Electrochemistry Communications* **2010,** 12 (3), 427-430.

(49) Wang, L.; Maxisch, T.; Ceder, G. *Chemistry of Materials* **2006,** 19 (3), 543-552.

(50) Kramer, D.; Ceder, G. *Chemistry of Materials* **2009,** 21 (16), 3799-3809.

(51) Mo, Y. F.; Ong, S. P.; Ceder, G. *Physical Review B* **2011,** 84 (20), 1-9.

(52) Lee, B.; Seo, D.-H.; Lim, H.-D.; Park, I.; Park, K.-Y.; Kim, J.; Kang, K. *Chemistry of Materials* **2014,** 26 (2), 1048-1055.

(53) Radin, M. D.; Rodriguez, J. F.; Tian, F.; Siegel, D. J. *Journal of the American Chemical Society* **2012,** 134 (2), 1093-1103.

(54) Hummelshøj, J. S.; Blomqvist, J.; Datta, S.; Vegge, T.; Rossmeisl, J.; Thygesen, K. S.; Luntz, A. C.; Jacobsen, K. W.; Nørskov, J. K. *Journal of Chemical Physics* **2010,** 132 (7), 071101.

(55) Hummelshøj, J. S.; Luntz, A. C.; Nørskov, J. K. *The Journal of Chemical Physics* **2013,** 138 (3), 034703-034712.

(56) Kang, S.; Mo, Y.; Ong, S. P.; Ceder, G. *Chemistry of Materials* **2013,** 25 (16), 3328-3336.

(57) Kang, S.; Mo, Y.; Ong, S. P.; Ceder, G. *Nano Letters* **2014,** 14 (2), 1016-1020.

(58) Chase, M. W.; National Institute of, S.; Technology, *NIST-JANAF thermochemical tables*. American Chemical Society ; American Institute of Physics for the National Institute of Standards and Technology: [Washington, D.C.]; Woodbury, N.Y., 1998.

(59) Abraham, K. M.; Jiang, Z. *Journal of the Electrochemical Society* **1996,** 143 (1), 1-5.

(60) Jung, H.-G.; Hassoun, J.; Park, J.-B.; Sun, Y.-K.; Scrosati, B. *Nature Chemistry* **2012,** 4 (7), 579-585.

(61) Ogasawara, T.; Debart, A.; Holzapfel, M.; Novak, P.; Bruce, P. G. *Journal of the American Chemical Society* **2006,** 128 (4), 1390-1393.

(62) Black, R.; Adams, B.; Nazar, L. F. *Advanced Energy Materials* **2012,** 2 (7), 801-815.

(63) Lee, J. S.; Kim, S. T.; Cao, R.; Choi, N. S.; Liu, M.; Lee, K. T.; Cho, J. *Advanced Energy Materials* **2011,** 1 (1), 34-50.

(64) Girishkumar, G.; McCloskey, B.; Luntz, A. C.; Swanson, S.; Wilcke, W. *Journal of Physical Chemistry Letters* **2010,** 1 (14), 2193-2203.

(65) Shao, Y. Y.; Park, S.; Xiao, J.; Zhang, J. G.; Wang, Y.; Liu, J. *Acs Catalysis* **2012,** 2 (5), 844-857.

(66) Lu, Y. C.; Kwabi, D. G.; Yao, K. P. C.; Harding, J. R.; Zhou, J. G.; Zuin, L.; Shao-Horn, Y. *Energy & Environmental Science* **2011,** 4 (8), 2999-3007.

(67) Harding, J. R.; Lu, Y. C.; Tsukada, Y.; Shao-Horn, Y. *Physical Chemistry Chemical Physics* **2012,** 14 (30), 10540-10546.

(68) Xu, W.; Viswanathan, V. V.; Wang, D. Y.; Towne, S. A.; Xiao, J.; Nie, Z. M.; Hu, D. H.; Zhang, J. G. *Journal of Power Sources* **2011,** 196 (8), 3894-3899.

(69) Xiao, J.; Hu, J. Z.; Wang, D. Y.; Hu, D. H.; Xu, W.; Graff, G. L.; Nie, Z. M.; Liu, J.; Zhang, J. G. *Journal of Power Sources* **2011,** 196 (13), 5674-5678.

(70) Laoire, C. O.; Mukerjee, S.; Abraham, K. M.; Plichta, E. J.; Hendrickson, M. A. *Journal of Physical Chemistry C* **2009,** 113 (46), 20127-20134.

(71) Lu, Y. C.; Gasteiger, H. A.; Shao-Horn, Y. *Journal of the American Chemical Society* **2011,** 133 (47), 19048-19051.

(72) Lu, Y. C.; Xu, Z. C.; Gasteiger, H. A.; Chen, S.; Hamad-Schifferli, K.; Shao-Horn, Y. *Journal of the American Chemical Society* **2010,** 132 (35), 12170-12171.

(73) McCloskey, B. D.; Scheffler, R.; Speidel, A.; Bethune, D. S.; Shelby, R. M.; Luntz, A. C. *Journal of the American Chemical Society* **2011,** 133 (45), 18038-18041.

(74) McCloskey, B. D.; Speidel, A.; Scheffler, R.; Miller, D. C.; Viswanathan, V.; Hummelshoj, J. S.; Norskov, J. K.; Luntz, A. C. *The Journal of Physical Chemistry Letters* **2012,** 3 (8), 997-1001.

(75) Zhang, Z.; Lu, J.; Assary, R. S.; Du, P.; Wang, H.-H.; Sun, Y.-K.; Qin, Y.; Lau, K. C.; Greeley, J.; Redfern, P. C.; Iddir, H.; Curtiss, L. A.; Amine, K. *The Journal of Physical Chemistry C* **2011,** 115 (51), 25535-25542.

(76) Lu, Y.-C.; Crumlin, E. J.; Veith, G. M.; Harding, J. R.; Mutoro, E.; Baggetto, L.; Dudney, N. J.; Liu, Z.; Shao-Horn, Y. *Scientific Reports* **2012,** 2.

(77) Jung, H.-G.; Kim, H.-S.; Park, J.-B.; Oh, I.-H.; Hassoun, J.; Yoon, C. S.; Scrosati, B.; Sun, Y.-K. *Nano Letters* **2012,** 12 (8), 4333-4335.

(78) Yang, J.; Zhai, D.; Wang, H.-H.; Lau, K. C.; Schlueter, J. A.; Du, P.; Myers, D. J.; Sun, Y.-K.; Curtiss, L. A.; Amine, K. *Physical Chemistry Chemical Physics* **2013,** 15 (11), 3764-3771.

(79) McCloskey, B. D.; Scheffler, R.; Speidel, A.; Girishkumar, G.; Luntz, A. C. *Journal of Physical Chemistry C* **2012,** 116 (45), 23897-23905.

(80) Oh, S. H.; Nazar, L. F. *Advanced Energy Materials* **2012,** 2 (7), 903-910.

(81) Lu, Y.-C.; Shao-Horn, Y. *The Journal of Physical Chemistry Letters* **2012,** 4 (1), 93-99.

(82) Ong, S. P.; Mo, Y. F.; Ceder, G. *Physical Review B* **2012,** 85 (8), 2-5.

(83) Chen, J.; Hummelshoj, J. S.; Thygesen, K. S.; Myrdal, J. S. G.; Norskov, J. K.; Vegge, T. *Catalysis Today* **2011,** 165 (1), 2-9.

(84) Zhao, Y. F.; Ban, C. M.; Kang, J.; Santhanagopalan, S.; Kim, G. H.; Wei, S. H.; Dillon, A. C. *Applied Physics Letters* **2012,** 101 (2).

(85) Viswanathan, V.; Thygesen, K. S.; Hummelshoj, J. S.; Norskov, J. K.; Girishkumar, G.; McCloskey, B. D.; Luntz, A. C. *Journal of Chemical Physics* **2011,** 135 (21), 214704.

(86) Bryantsev, V. *Theor Chem Acc* **2012,** 131 (7), 1-11.

(87) Haynes, W. M., *CRC handbook of chemistry and physics*. 93th edition ed.; CRC Press: 2012.

(88) Cota, L. G.; de la Mora, P. *Acta Crystallogr B* **2005,** 61, 133-136.

(89) Chan, M. K. Y.; Shirley, E. L.; Karan, N. K.; Balasubramanian, M.; Ren, Y.; Greeley, J. P.; Fister, T. T. *Journal of Physical Chemistry Letters* **2011,** 2 (19), 2483-2486.

(90) Radin, M. D.; Rodriguez, J. F.; Siegel, D. J. In *Lithium peroxide surfaces and point defects: Relevance for Li-air batteries*, Battery Congress 2011, Ann Arbor, Michigan, USA, 2011; Uddin, M. N.; Tang, T.; Thompson, J.; Uddin, R., Eds. Global Automotive Management Council
Curran Associates, Inc.: Ann Arbor, Michigan, USA.

(91) Yanli, W.; Yi, D.; Jun, N. *Journal of Physics: Condensed Matter* **2009,** 21 (3), 035401.

(92) Xiao, R.; Li, H.; Chen, L. *Chemistry of Materials* **2012,** 24 (21), 4242-4251.

(93) Bakulina, V. M.; Tokareva, S. A.; Vol'nov, I. I. *Journal of Structural Chemistry* **1967,** 8 (6), 980-981.

(94) Seriani, N. *Nanotechnology* **2009,** 20 (44), 445703.

(95) Lau, K. C.; Curtiss, L. A.; Greeley, J. *Journal of Physical Chemistry C* **2011,** 115 (47), 23625-23633.

(96) Alfe, D. *Computer Physics Communications* **2009,** 180 (12), 2622-2633.

(97) Wang, X.; Andrews, L. *Molecular Physics* **2009,** 107 (8-12), 739-748.

(98) Andrews, L. *The Journal of Chemical Physics* **1969,** 50 (10), 4288-4299.

(99) Rolfe, J.; Holzer, W.; Murphy, W. F.; Bernstein, H. J. *The Journal of Chemical Physics* **1968,** 49 (2), 963-963.

(100) Aydinol, M. K.; Kohan, A. F.; Ceder, G.; Cho, K.; Joannopoulos, J. *Physical Review B* **1997,** 56 (3), 1354-1365.

(101) Doe, R. E.; Persson, K. A.; Meng, Y. S.; Ceder, G. *Chemistry of Materials* **2008,** 20 (16), 5274-5283.

(102) Malik, R.; Zhou, F.; Ceder, G. *Nature Materials* **2011,** 10 (8), 587-590.

(103) Debart, A.; Paterson, A. J.; Bao, J.; Bruce, P. G. *Angewandte Chemie-International Edition* **2008,** 47 (24), 4521-4524.

(104) Lau, K. C.; Assary, R. S.; Redfern, P.; Greeley, J.; Curtiss, L. A. *The Journal of Physical Chemistry C* **2012,** 116 (45), 23890-23896.

(105) Li, Y.; Yadegari, H.; Li, X.; Norouzi Banis, M.; Li, R.; Sun, X. *Chemical Communications* **2013,** 49 (100), 11731-11733.

(106) Sun, Q.; Yang, Y.; Fu, Z.-W. *Electrochemistry Communications* **2012,** 16 (1), 22-25.

(107) Das, S. K.; Xu, S.; Archer, L. A. *Electrochemistry Communications* **2013,** 27 (0), 59-62.

(108) Carter, G. F.; Templeton, D. H. *Journal of the American Chemical Society* **1953,** 75 (21), 5247-5249.

(109) Templeton, D. H.; Dauben, C. H. *Journal of the American Chemical Society* **1950,** 72 (5), 2251-2254.

(110) McQuarrie, D. A., *Statistical Mechanics*. University Science Books: 2000.

(111) Gonze, X. *Physical Review A* **1995,** 52 (2), 1096-1114.

(112) Gonze, X. *Physical Review A* **1995,** 52 (2), 1086-1095.

(113) Baroni, S.; Giannozzi, P.; Testa, A. *Physical Review Letters* **1987,** 58 (18), 1861-1864.

(114) Ramamoorthy, M.; Vanderbilt, D.; King-Smith, R. D. *Physical Review B* **1994,** 49 (23), 16721-16727.

(115) Reuter, K.; Scheffler, M. *Physical Review B* **2001,** 65 (3), 035406.

(116) Otsuka, K.; Murakami, Y.; Wada, Y.; Said, A. A.; Morikawa, A. *Journal of Catalysis* **1990,** 121 (1), 122-130.

(117) Shimada, H.; Galuszka, J., Infrared spectroscopic study of methane coupling over Na2O2. In *Studies in Surface Science and Catalysis*, Kevin, J. S.; Emerson, C. S., Eds. Elsevier: 1992; Vol. Volume 73, pp 99-102.

(118) Song, M.-K.; Park, S.; Alamgir, F. M.; Cho, J.; Liu, M. *Materials Science and Engineering: R: Reports* **2011,** 72 (11), 203-252.

(119) Xiao, J.; Mei, D.; Li, X.; Xu, W.; Wang, D.; Graff, G. L.; Bennett, W. D.; Nie, Z.; Saraf, L. V.; Aksay, I. A.; Liu, J.; Zhang, J.-G. *Nano Letters* **2011,** 11 (11), 5071-5078.

(120) Read, J. *Journal of The Electrochemical Society* **2002,** 149 (9), A1190-A1195.